NIOBIUM NITRIDE BASED THIN FILMS DEPOSITED BY DC REACTIVE MAGNETRON SPUTTERING: NbN, NbSiN AND NbAlN

THÈSE N^{O} 3325 (2005)

PRÉSENTÉE À LA FACULTÉ SCIENCES DE BASE

Institut de physique de la matière complexe

SECTION DE PHYSIQUE

ÉCOLE POLYTECHNIQUE FÉDÉRALE DE LAUSANNE

POUR L'OBTENTION DU GRADE DE DOCTEUR ÈS SCIENCES

PAR

Moushab BENKAHOUL

Magister en physique du solide, Université de Constantine, Algérie
et de nationalité algérienne

acceptée sur proposition du jury:

Prof. F. Lévy, directeur de thèse
Prof. A. Fiore, rapporteur
Dr N. Martin, rapporteur
Dr J. Patscheider, rapporteur

Lausanne, EPFL
2005

Abstract

Due to their high hardness, high melting point and high chemical stability, transition metal nitrides present a great interest for various applications. This work constitutes a contribution to the understanding of the properties of Nb based binary and ternary nitride materials. It deals with the study of the deposition and characterization of the niobium nitride system.

Single and mixed phase thin films of niobium nitride in addition to niobium silicon nitride and niobium aluminum nitride were deposited by DC reactive magnetron sputtering. The properties of these thin films are investigated using several experimental techniques: X-ray diffraction, scanning and transmission electronic microscopy, optical reflectivity and spectroscopic ellipsometry, X-ray photoelectron spectroscopy, Fourier transform infrared spectroscopy, electrical measurements and nanoindentation.

The influence of the nitrogen partial pressure and substrate temperature on the phase composition is studied. Single and mixed phase of niobium nitride films: β-Nb_2N, δ-NbN and δ´-NbN were successfully deposited.

The single phase niobium nitride films are characterized. Properties of mixed phase films are interpreted in the light of that of single phase. All NbN thin films have a columnar morphology. The columnar structure in the hexagonal phases is more pronounced than in the cubic. The hexagonal δ´ and β phases are more covalent than the cubic one. The physical parameters (carrier charge density N^* and free electron relaxation time τ) for each single phase were calculated by fitting the optical properties using a Drude model with a set of Lorentz oscillators. High hardness values of 35 and 40 GPa are measured for the β and δ´ phases, respectively. They are larger than that of the cubic δ phase, 25 GPa. This hardness values is related to the high covalent character of the hexagonal phases compared to that of the cubic. Hardness of mixed phase is determined by the hardness of the majority phase.

Influence of the addition of a third element, Si and Al, into NbN is studied. Nb-Si-N and Nb-Al-N thin films were deposited and characterized.

A model for the film formation of Nb-Si-N thin films deposited by DC magnetron sputtering is proposed. Three distinct concentration domains were pointed out. In Domain 1 ($1 \le C_{Si} \le 4$ at.%) the Si atoms substitute Nb in the NbN lattice and polycrystalline films of NbN:Si are deposited. In Domain 2 ($4 \le C_{Si} \le 7$ at.%) a fraction of Si atoms segregates to the grain boundaries. A SiN_x layer forms on the NbN:Si crystallite surfaces. The covering ratios increase with Si content up to 100% (formation of a monolayer). For further increase of Si content (Domain 3), the NbN:Si crystallites, surrounded by a monolayer of SiN_x, reduce their size from 18 to 2 nm. The increasing amount of the SiN_x phase in the films is realized by increasing the surface to volume ratio of the NbN:Si nanocrystallites.

The formation of the SiN_x layer explains the change observed in the electrical and optical properties of Nb-Si-N films with increasing the Si content. The electrical resistivity measured as a function of temperature is proposed to provide an experimental mean for determining the limit of Si solubility in the Nb-Si-N system and for following the thickness evolution of the SiN_x coverage layer in the composite films.

For $Nb_zAl_yN_x$ films, the solubility limit of the Al in the NbN lattice is in the range: $y/(y+z) = 0.5 \pm 0.1$. Passing this value an insulating hexagonal AlN_x phase is formed. The electronic properties of the $Nb_zAl_yN_x$ are significantly altered by the changes in the value of y and x. The resistivity increases with increasing y. The hardness of $Nb_zAl_yN_x$ is maximum in films with $y = 0.19$ (solubility limit). At higher y the formation of the AlN_x phase reduces the hardness. The increase of hardness observed in the $Nb_zAl_yN_x$ films is attributed to the solid solution hardening mechanism.

If the system NbN presents many phases, it appears that the addition of a third element, Si and Al, allows the stabilization of the cubic δ phase. In both Nb-Si-N and Nb-Al-N systems Si and Al are soluble up to a certain limit. Passing this limit the third element segregates at the grain boundaries forming SiN_x and hexagonal AlN_x. If in the case of Nb-Si-N, the formed SiN_x cannot be detected by X-ray diffraction due to the fact that it segregates as a thin layer at the grain boundaries of the NbN grains. In the case of the Nb-Al-N the hexagonal AlN_x phase is clearly detected. The high Al solubility in the Nb-Al-N gives rise to a large change of the electronic properties with increasing the Al content.

Version abrégée

A cause de leur grande dureté, de leur point de fusion élevé, de leur grande stabilité chimique, les nitrures des matériaux de transition présentent un grand intérêt en vue d'applications variées. Ce travail constitue une contribution dans la compréhension des propriétés de ces matériaux. Il est consacré à l'étude du dépôt et de la caractérisation du system nitrure de niobium.

Des couches minces monophasées et biphasées de nitrure de niobium ainsi que des nitrures de niobium-aluminium et niobium-silicium ont été déposées par pulvérisations cathodique magnétron en mode DC. Les propriétés de ces couches minces sont étudiées par plusieurs techniques: Diffraction des rayons X, microscopie électronique à balayage et en transmission, réflectivité optique et ellipsométrie spectroscopique, spectroscopie photoélectronique des rayons X, mesures électriques et nanoindentation.

L'influence de la pression partielle d'azote et de la température du substrat sur la composition phasique est étudiée. Les couches minces déposées sont monophasées et biphasées et ont la composition: β-Nb_2N, δ-NbN and δ´-NbN.

Les couches minces monophasées sont sélectionnées et caractérisées. Les propriétés des couches minces biphasées sont interprétées avec comparaison avec ceux des couches monophasées. Toutes les couches minces de nitrure de niobium présentent une morphologie colonnaire. Cette dernière se manifeste plus clairement dans les phases hexagonales que cubique. Les phases hexagonales sont plus covalentes que la phase cubique. Les paramètres électroniques de chaque phase sont calculés à partir des propriétés optiques, en utilisant le model de Drude complété par un ensemble d'oscillateurs lorentziens. Les phases hexagonales β-Nb_2N et δ´-NbN présentent respectivement une grande dureté de 35 et 40 GPa. Cette dureté est très élevée comparée à celle de la phase cubique qui vaut 25 GPa. Ces différentes valeurs de duretés sont liées au caractère plus covalent des phases hexagonales comparé à celui de la phase cubique. Pour le mélange de phases (biphasé) la dureté est déterminée par la dureté de la phase majoritaire.

L'influence de l'addition d'un troisième élément, Si et Al, est étudiée. Des couches minces de Nb-Si-N et Nb-Al-N ont été déposées et charatérisées .

Un model pour la formation des couches minces de Nb-Si-N déposées par pulvérisation magnétron est proposé. Trois domaines de concentration de Si sont déterminés. Dans le domaine 1 ($1 \leq C_{Si} \leq 4$ at.%) les atomes de Si substituent les

atomes de Nb dans le réseau NbN. Des couches minces polycristallines NbN :Si sont donc déposées. Dans le domaine 2 (4≤ C_{Si} ≤7 at.%) une fraction des atomes de Si s'accumulent au joints de grains. Une couche de SiN_x se forme sur les surfaces des cristallites de NbN :Si. Le rapport de couverture augmente avec la concentration de Si jusqu'à 100% (formation d'une monocouche). Au delà, l'augmentation de la concentration de Si (domaine 3) implique une diminution de la taille des cristallites de NbN :Si, entourées de la monocouche de SiN_x, de 18 nm à 2 nm. Ainsi l'augmentation de la concentration de Si dans les couches minces est absorbée par la réduction du rapport surface volume des nanocristallites de NbN :Si.

La formation de la monocouche SiN_x explique les changements observés dans les propriétés électriques et optiques des couches minces de Nb-Si-N avec l'augmentation de la concentration de Si. La mesure de la résistivité en fonction de la température est proposée comme moyen expérimental pour la détermination de la limite de solubilité de Si dans le system Nb-Si-N et pour suivre l'évolution de l'épaisseur de la couche SiN_x qui entoure les cristallites dans les couches minces composites.

Pour les couches minces de $Nb_zAl_yN_x$ la limite de solubilité de Al dans le NbN est: $y/(y+z) = 0.5 \pm 0.1$. Au dessus de cette valeur, une phase isolante de l'AlN_x hexagonal est formée. Les propriétés électroniques de couches minces de $Nb_zAl_yN_x$ sont sensiblement modifiées par le changement dans les valeurs de y et x. La résistivité électrique augmente avec l'augmentation de y. La dureté des couches minces de $Nb_zAl_yN_x$ est maximale pour $y = 0.19$ (limite de solubilité). Pour les plus grandes valeurs de y, la formation de la phase AlN_x entraine une diminution de la dureté. L'augmentation de la dureté observée dans les couches minces de $Nb_zAl_yN_x$ est attribuée au durcissement par solution solide.

Si le système NbN présente plusieurs phases, il apparait que l'addition d'un troisième élément permet la stabilisation de la phase cubique δ. Dans les deux systemes Nb-Si-N et Nb-Al-N, Si et Al sont solubles jusqu'à une certaine limite. Au-delà de cette limite, le troisième élément se sépare et s'accumule aux joints des grains pour former une deuxième phase : SiN_x ou AlN_x. Dans le cas de SiN_x il n'est pas possible de la détecter par diffraction des rayons X a cause du fait qu'elle forme une couche mince autour des grains de NbN :Si. Par contre la phase hexagonale AlN_x est facilement détectable à cause de sa ségrégation sous forme d'une phase indépendante. La grande solubilité de Al dans le NbN est à l'origine de variations significatives des propriétés électroniques en variant la concentration de Al.

ملخـــــص

نظرا لصلادتها العالية ودرجة انصهارها المرتفعة واستقرارها الكيميائي، أظهرت نتريدات العناصر الانتقالية أهمية كبيرة في ميادين تطبيقية مختلفة.

يمثل هذا العمل مساهمة في فهم خواص هذه المواد وهو موجه بالخصوص لدراسة ترسيب و تخصيص نظام نتريد النيوبيوم.

لقد تم ترسيب شرائح رقيقة وحيدة وثنائية الطورلنتريد النيوبيوم وكذا نتريدات النيوبيوم – ألمنيوم و النيوبيوم – سليكون بطريقة الرش المهبطي المغناطيسي ذي التيار المباشر ثم درست خواص العينات المرسبة بالاعتماد على عدة تقنيات نذكر منها: انعراج الأشعة السينية، المجهر الإلكتروني الماسح والنفاذي، الانعكاسية الضوئية، المطيافية الإهليليجية، مطيافية الإلكترونات الضوئية المثارة بالأشعة السينية، القياسات الكهربائية والغرز النانومتري.

درسنا في هذا العمل، تأثير الضغط الجزئي للنتروجين ودرجة حرارة المسند على التركيب الطوري، كما رسبنا شرائح رقيقة وحيدة وثنائية الطورلنتريد النيوبيوم δ'-NbN, δ-NbN, β-Nb_2N . تم انتقاء الشرائح الرقيقة وحيدة الطور ودرست خواصها أما خواص الشرائح ثنائية الطور فقد تم تفسيرها مع تلك الخاصة بأحادية الطور.
أظهرت كل شرائح نتريد النيوبيوم بنية على شكل أعمدة، وتظهر هذه البنية جليا في الأطوار السداسية كما تتميز الأطوار السداسية بتكافئية أعلى من الطور المكعب.

كما تم في هذه الدراسة حساب الوسائط الإلكترونية لكل طور بإجراء مقاربة للخواص الضوئية اعتمادا على نموذج درود إضافة إلى جملة من الهزازات اللورنتزية.
أبدت الأطوار السداسية β-Nb_2N و δ'-NbN صلادة عالية تقدر ب:35 و 40 جيغاباسكال على التوالي وتعد هذه الصلادة جد عالية مقارنة بتلك الخاصة بالطور المكعب والتي تقدر ب 25 جيغاباسكال. ويعزى هذا الفرق في الصلادة إلى السلوك التكافئي الكبير للأطوار السداسية مقارنة بالطور المكعب. أما فيما يتعلق بالمزيج الطوري فإن الصلادة تحدد بصلادة الطور الغالب.

تناول هذا العمل أيضا دراسة تأثير إضافة عنصر ثالث(Si, Al) للنظام المدروسNbN و في هذا الصدد تم اقتراح نموذج لتكوين الشرائح الرقيقة لـ Nb-Si-N المرسبة بالرش المهبطي المغناطيسي. وجاء النموذج ليوضح السلوك في ثلاث ميادين مختلفة من تركيز Si. في المجال الأول $1 \le C_{Si} \le 4$at.% تحل ذرات Si محل ذرات Nb في الشبكة البلورية لـNbN و تشكل بذلك شرائح رقيقة لـSi : NbN. في المجال الثاني$4 \le C_{Si} \le 7$at.% يترسب مقدار معين من ذرات Si في الحدود الحبيبية مما يؤدي إلى تشكيل شريحة من SiN_x على سطوح بليراتSi : NbN . وقد تبين أن نسبة التغطية تزداد مع تركيز Si إلى أن تبلغ 100% (تشكل شريحة أحادية) و بالدخول في المجال الثالث تؤدي زيادة تركيز Si إلى نقصان البعد الحبيبي لحبيباتSi: NbN المحاطة بالشرائح الأحادية لـSiN_x منnm 18 إلى nm 2. تضمن الزيادة في تركيزSi في الشرائح الرقيقة بانخفاض نسبة السطح إلى حجم بليرات NbN:Si

يفسر تشكل الشريحة الأحادية SiN_x التغيرات الملاحظة على الخواص الكهربائية و الضوئية للشرائح الرقيقة لـ Nb-Si-N مع زيادة تركيزSi.

اقترح قياس المقاومية بدلا لة درجة الحرارة كأداة تجريبية لتحديد حد انحلالية Si في النظامNb-Si-N وكذا تتبع تغير سمك شريحة SiN_x التي تحيط بالبليرات في الشرائح الرقيقة للمواد المركبة.

أما فيما يخص الشرائح الرقيقة $Nb_zAl_yN_x$ فان حد انحلالية Al في شبكة NbN فهي في المجال $y/(y+z)=0.5\pm0.1$. إذا اجتيزت هذه القيمة يتشكل طور عازل سداسي البنية AlN_x . لقد وجد أن الخصائص الالكترونية للشرائح الرقيقة $Nb_zAl_yN_x$ جد حساسة لتغيرقيمx وy فالمقاومية الكهربائية تزداد بزيادة قيمة y أما صلادة الشرائح $Nb_zAl_yN_x$ فتكون أعظمية من أجل$y=0.9$ (حد الانحلالية) في حين أنه من أجل قيم أعلى لـy تتناقص الصلادة جراء تشكل الطور سداسي البنية AlN_x . يعزى ارتفاع الصلادة الملاحظ في الشرائح الرقيقة $Nb_zAl_yN_x$ إلى التصليد بالمحلول الصلب.

إذا كان النظام NbN يبدي عدة أطوار فان إضافة عنصر ثالث يجعل من الطور المكعب أكثر استقرارا. إن العنصر المضاف ينحل في النظامين Nb-Si-N و Nb-Al-N إلى حد معين و عندما يجتاز هذا الحد يبدأ في الانعزال في الحدود الحبيبية ليتشكل بذلك طور ثان SiN_x أو AlN_x يتعذر على الأشعة السينية الكشف على SiN_x بالانعراج لأن هذه

الأخيرة تشكل شريحة رقيقة حول حبيبات NbN:Si على عكس الطور AlN_x الذي يسهل الكشف عنه بالأشعة السينية بسبب إنعزاله في الحدود الحبيبية مشكلا بذلك طورا مستقلا. إن الإنحلالية الكبيرة للألمنيوم في شبكة NbN تعطي إمكانية حدوث تغيرات معتبرة في الخواص الإلكترونية بتغير تركيز الألمنيوم.

Table of contents

Chapter 1

Introduction

The present work addresses the deposition by DC reactive magnetron sputtering of niobium nitride: NbN, Nb-Si-N and Nb-Al-N thin films and their physical characterization.

Transition metal nitrides (MeN) (Me =Ti, Cr, Nb...etc.) are refractory metals that present major interest in functional coatings and surface engineering. They possess excellent mechanical and tribological properties, high hardness, high wear and oxidation resistance. They show a metallic luster and have a metallic thermal and electrical conductivity, of the order of magnitude of pure metals, and often are superconductors [1]. These properties are a consequence of the complex chemical bonding which mixes covalent, ionic and metallic contributions.

Among these materials, niobium nitride (NbN) crystallizes with a NaCl type of structure; it has been of considerable interest since the discovery of its superconducvity by Ashermann and co-workers [2]. Among the binary compounds with the NaCl type structure it has the highest superconductivity critical temperature T_c [3]. In contrast, only scant information is available on its mechanical properties, such as microhardness, crack resistance, and wear resistance

[4]. The NbN system is complex and presents various phases e.g. β, δ, ε, γ, δ´ and η [5-8]. The well studied phase remains the cubic δ phase.

Recently, it was found that the properties of MeN thin films can be improved by the addition of the third element e.g. Si and Al. The Ti-Si-N and Ti-Al-N sputter deposited films, for instance, show better mechanical properties such as higher hardness and oxidation resistance, compared to simple TiN materials [9,10].

Even if it is clear that the addition of Si and Al to MeN materials improves their mechanical and tribological properties, the hardening mechanism in Me-Si-N materials remains a subject of a controversial discussion. Veprek et al. [11] attributed the hardening in these materials to their nanocomposites microstructure, which consists in a mixture of phases: nanocrystallites of MeN and amorphous SiN_x. In contrast, the hardening observed in Zr-Si-N [12] and Cr-Si-N [13] was attributed to a different mechanism: the solid solution hardening which is caused by the incorporation of a small amount of silicon in the MeN lattice.

In the case of Me-Al-N films, most of the works attribute the hardening to the solid solution hardening mechanism whereas the good oxidation resistance is attributed to the formation of a passive Al oxide layer. This layer prevents the diffusion of oxygen toward the bulk of the Me-Al-N film. While the studies of the Ti-Si-N and Ti-Al-N were extended to Cr-Si-N [13], Zr-Si-N [12] and Cr-Al-N [14] Zr-Al-N [15], no results were reported on the deposition and characterisation of Nb-Si-N and Nb-Al-N films.

In this work NbN, Nb-Si-N and Nb-Al-N thin films were deposited by DC reactive magnetron sputtering. The manuscript is divided in 6 chapters:

The chapter 1 as an introduction to the work and places it with respect of the state of the art.

In chapter 2, the deposition method and parameters as well as the experimental techniques for characterization e.g. EPMA, XRD, SEM, TEM, nanoindentation, are presented.

In chapter 3 the results are reported of the study of the influence of reactive sputter deposition parameters, nitrogen partial pressure P_{N2} and substrate temperature T_s, on the phase composition of NbN films. The physical characterization of films is also discussed. Three phases have been successfully deposited: cubic δ, hexagonal δ´ and β. The structural, morphological, electronic and mechanical properties are systematically studied. The relationship between their functional, e.g. hardness, and fundamental, e.g. crystalline structure, electronic properties and morphology properties is investigated.

Chapter 4 presents the influence of Si on the properties of NbN. Si was added to NbN in order to study the properties of the nanocomposite Nb-Si-N. In particular, the influence of Si addition on the hardness behavior is investigated in relation with the spectacular and controversial properties of Ti-Si-N [9].

Chapter 5 deals with the study of the influence of the addition of Al on the properties of NbN, a series of Nb-AI-N films were deposited and characterized. The role of Al addition is particularly interesting with respect to oxidation resistance as investigated in Ti-Al-N for example [10].

The main results of this work are the success of the deposition of thin films of single and mixed NbN phases: δ, δ´ and β and the study of their: structural, electronic and mechanical properties. All NbN phase films show a columnar morphology. The columnar structure in the hexagonal phases is more evidential than in the cubic. X-ray photoelectron spectroscopy (XPS) measurements reveal that the hexagonal δ´ and β phases are more covalent than the cubic one. The optical properties of single δ, δ´ and β phases significantly differ. This property can be used for the determination of the phase composition, in the NbN system, using ellipsometric spectroscopy. From the optical properties, fitted by a Drude model with a set of Lorentz oscillators, the electronic parameters for each single phase film can be derived. The high hardness of 35 and 40 GPa observed for the β and δ', respectively, compared to that of the cubic δ, 25 GPa, can be related to the high covalent character of the hexagonal phases compared to that of the cubic. In mixed phase the hardness is determined by the hardness of the majority phase.

A model of the morphology evolution as a function of the Si content is proposed for the Nb-Si-N films. The model splits the morphology evolution in three domains. In the first domain (Si content below 4 at. %) the Si atoms are soluble in the NbN lattice whereas in the second domain (Si content between 4 and 7 at. %) the Si atoms begin to segregate at the grain boundaries of the NbN grains forming a layer of SiN_x. In the third domain (higher Si content) the NbN grain size reduces with keeping constant the thickness of the SiN_x layer. This model allows explaining the evolution of whole Nb-Si-N films properties as a function of the Si content. The deposited Nb-Si-N films show the typical hardness behavior observed in the Me-Si-N (Me: Ti, Cr, Zr) [9,12-13]. The hardening was attributed to the solid solution mechanism. The electrical resistivity measured as a function of temperature allows detecting the presence of the insulating SiN_x phase at the grain boundaries.

The solubility limit of Al in NbN was determined from the X-ray diffraction diagrams. In the limit of Al solubility domain, the electronic properties of Nb-Al-N significantly change, indicating the decrease of the electronic density at the E_F of the material with increasing Al content. The highest hardness was observed for the film with maximum concentration of soluble Aluminum. At higher Al content the insulating hexagonal AlN phase appears leading to a drastic decrease in the hardness.

The addition of each third element, Si and Al, allows the stabilization of the cubic δ phase in the NbN system.

References of chapter 1

[1] S.P. Denker, J. of the Less-Common Metals 14 (1968) 1.
[2] G. Ashermann, E. Friedrich, E. Justi and J. Kramer, z. Phys. 42 (1941) 349.
[3] G.I. Oya J. Appl. Phy. 45 (3) March 1974.
[4] V. N. Zhitomirsky, I. Grimberg, L. Rapoport, N. A. Travitzky, R. L. Boxman, S. Goldsmith, A. Raihel, I. Lapsker and B. Z. Weiss, Thin Solid Films 326, 1-2 (1998) 134.
[5] H. Hollek, Binäre und ternäre Carbid- und Nitridsysteme der Uebergangsmetalle, Gebrüder Borntraeger, Berlin–Stuttgart, 1984.
[6] Yu.V. Levinskiy. Russ. Metall. (1974) 34.
[7] W. Lengauer, M. Bohn, B. Wollein and K. Lisak. Acta Mater. 48 (2000) 2633.
[8] G. Brauer, and Esselborn, Z. Anorg. Allg. Chem. 309 (1961) 151
[9] M. Diserens, J. Patscheider and F. Lévy, Surf. Coat. Technol. 120–121 (1999) 158.
[10] A. Hörling, L. Hultman, M. Odén, J. Sjölén and L. Karlsson, Surf. Coat. Technol. 191 (2005) 384.
[11] S. Veprek, J. Vac. Sci. Technol. A 17 (1999) (5) 2401.
[12] M. Nose and W.A. Chiou, J. Vac. Sci. Technol. A 20 (2002) (3) 823
[13] E. Martinez, R. Sanjinés, O. Banakh and F. Lévy, Thin Solid Films 447–448 (2004) 332.
[14] O. Banakh, P.E. Schmid, R. Sanjinés and F. Lévy, Surf. Coat. Technol. 163–164 (2003) 57.
[15] Y. Makino, M. Mori, S. Miyake, K. Saito and K. Asami, Surf. Coat. Technol. 193 (2005) 219.

Chapter 2

Deposition method and characterization techniques

In this chapter, the author reports a brief description of the sputter deposition method and a detail of the parameters of the films deposition. Basic principles of the characterization techniques, their resolution and the accuracy of each measure are also reported. The characterization techniques are presented according to the properties they study: chemical composition, structure and morphology, electronic properties and mechanical properties.

2.1. Coating deposition by sputtering

The sputtering process consists in the extraction of materials particles from a target which is bombarded with high energetic particles of inert gas, generally argon. The pressure of inert gas in the chamber is between 10^{-1} and 10^{+1} Pa [1]. The expulsed atoms or ions condens and react on the surface of the substrates. In magnetron sputtering, a magnetic field in front of the target causes an extended path length for plasma electrons. This induces an increase in the sputtering gas ionization and leads to higher deposition rate. If sputtering is done in atmosphere of inert gas (e.g. Ar) plus reactive gas (e.g. N_2, O_2) the method is called reactive sputtering. Deposition of metal nitrides films is often carried out by reactive magnetron sputtering (*RMS*). In the present work, *RMS* was used for the deposition of the thin films: (i) the high energies, involved in the process of this technique, allow the stabilization of metastable structures far from the thermodynamical equilibrium (case of NbN deposition); (ii) the possibility of employing two targets simultaneously permits the deposition of ternary nitrides under similar conditions to that of binary nitrides (case of deposition of NbSiN and NbAlN).

2.2. Deposition parameters of binary and ternary nitrides

Thin films studied in this work have been deposited by DC reactive magnetron sputtering. The deposition apparatus is equipped with two confocal targets (figure 2.1). The distance between the targets and the substrates was 10 cm. During the deposition, substrate heating is achieved by heating lamps placed at the back of the substrates holder. DC power supplies were used for the deposition of binary nitride (NbN) and ternary nitride (Nb-Si-N, Nb-Al-N) films. No substrate bias was applied during the deposition. The targets used for film depositions were Nb (99.95), Si (99.95) and Al (99.95). The target diameters were 5 cm. Pure gases Ar (99.999) and N_2 (99.999) were used. In order to avoid the film contamination, the targets were pre-sputtered for 10 min, under the same atmosphere used for the film deposition. Deposition was done on different types of substrates: polished silicon wafers, oxidized silicon wafers for electrical measurements, double side polished Si wafers for FTIR measurements and WC-Co strips for TEM cross-sectional observations. The total pressure was kept constant at 0.4 Pa for all deposited films. The films thickness is 1.2–1.9 µm, except for the samples for FTIR measurements where the thickness is 0.2–0.5 µm.

The N_2 partial pressure (P_{N2}) and the substrate temperature (T_s) were varied for the deposition of the NbN_x thin films. For the deposition of Nb-Si-N thin films the current on the Nb target (I_{Nb}) was kept constant whereas the current on the Si target (I_{Si}) was varied. The deposition of $Nb_{1-x}Al_xN_y$ was carried out by fixing either I_{Nb} and varying the current on Al target (I_{Al}) or by fixing I_{Al} and varying I_{Nb}. Table 1.1 summarizes the deposition conditions of each series of samples.

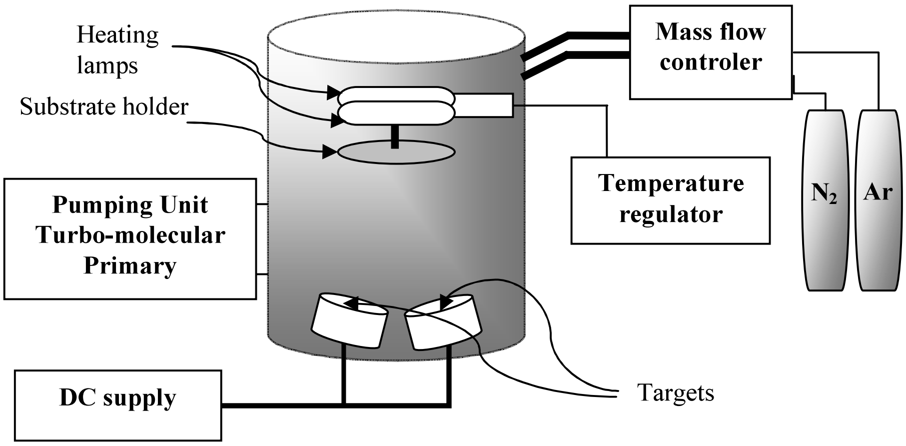

Fig. 2.1. Schematic description of the sputtering apparatus used for the film deposition.

Table 1.1 Deposition conditions details of films.

Samples	*Base pressure (Pa)*	P_{N2} (%)	T_s (°C)	I_{Nb} (A)	I_{Si} (A)	I_{Al} (A)
NbN_x						
Series 1	$\leq 5 \times 10^{-5}$	3-21	RT	0.25	--	--
Series 2	$\leq 10^{-4}$	15	RT-400	0.25	--	--
Series 3	$\leq 10^{-4}$	15-40	400	0.25	--	--
$NbSi_yN_x$	$\leq 2 \times 10^{-5}$	21	250	0.3	0-0.2	--
$Nb_{1-x}Al_xN_y$						
Series 1	$\leq 2 \times 10^{-5}$	21	250	0.3	--	0.03-0.1
Series 2	$\leq 2 \times 10^{-5}$	21	250	0.03-0.1	--	0.3

2.3. Characterization techniques

2.3.1. Chemical composition

2.3.1.1. Electron probe microanalysis

Electron probe microanalysis (*EPMA*) is based on the measurements of characteristic X-rays emitted from microscopic part of the sample bombarded by a beam of accelerated electrons. The intensity ratio of the characteristic X-rays (K- and L-edges) emitted from the sample is measured. For accurate quantitative analysis, the intensities of sample signal are compared to that of a standard specimen of known chemical composition. Thus, the atomic ratios are calculated.

In this study, a CAMECA SX 50 equipment was used for *EPMA* measurements. The analyses were performed at the Institute of Mineralogy at the University of Lausanne. In order to excite 1 µm of film depth, the sample is bombarded with electrons of 8 kV and 50 nA. The chemical composition value of each film is an average of at least 20 measurements performed on different sample places. The uncertainty of the technique measurement is typically 1 at.%.

2.3.1.2. Rutherford backscattering spectrometry

Rutherford backscattering spectrometry (*RBS*) consists in the bombardment of the sample by ions having enough energy (a few MeV) to penetrate the electron cloud of the target atoms and scatter elastically off the target nuclei (Rutherford scattering). An ion backscattered from a relatively heavy target atom carries a higher backscattered energy than an ion backscattered from a lighter atom [2]. The mass of the target atoms can be determined by measuring the collision energy transfer. Furthermore, knowing the scattering cross section enables a quantitative analysis of the atomic composition. The backscattered ions traveling through the sample lose energy by Coulomb interaction with the electrons. This allows obtaining depth information in the form of a chemical depth profile. *RBS* cannot usefully detect atoms lighter than the projectile.

For film sufficiently thin, *RBS* gives the value of the areal density (N_M) in at/cm^2. Knowing the film thickness (t), the density of film (ρ_{film}) can be calculated from the following equation

$$\rho_{film} = \frac{N_M \cdot < M_Z >}{t \cdot \mathrm{N_A}}$$

where $<M_Z> = \Sigma f_Z M_Z$ the average atomic mass (with f_Z and M_Z the atomic fraction and the atomic weight of element Z, respectively) and N_A is Avogadro's constant.

In this work, RBS investigations were performed for the chemical composition analysis and for the density measurements. The measurements were performed at the Centre d'Analyses par Faisceau Ionique (CAFI) at the École d'Ingénieurs (EICN) in Le Locle. He^+ ions and proton beams with energy of 2 MeV were used. Proton beam is more sensitive for light elements (e.g. N_2). The precision chemical composition is within ± 1at.%.

2.3.1.3. X-ray energy-dispersive spectrometry

X-ray energy-dispersive spectrometry (*XEDS*) technique is used for the determination of the local chemical composition. In fact, this method is done during *TEM* (see *2.3.2.4*) observations. The transmission electron microscope column includes an X-ray energy-dispersive spectrometer. Characteristic X-ray spectra emitted from electron-excited small volumes (few nm in diameter) of the sample are acquired. Chemical compositions were determined by using tabulated Cliff-Lorimer factors. The considered chemical composition value is an average of at least 5 measurements. The precision of the results is within ± 3 at.%.

2.3.2. *Structure and morphology determination*

2.3.2.1. Profilometry

In order to measure the film thickness, a part of the substrate is masked during the deposition. A profilometer (alpha-step 500 KLA Tencor Corporation) was used for the measurement of the height of the step from the bare substrate to the top of the deposited film. The precision of the thickness measurement is within ± 5 nm. Due to the thickness inhomogeneity the accuracy of the considered value of the thickness is 10%.

2.3.2.2. X-ray diffraction

X-ray diffraction (*XRD*) was used to determine the crystalline structure of the films. XRD was done on a RIGAKU instrument using monochromatic radiation (Cu K_α). Both configurations, grazing incidence (GI) at $\Omega = 4°$ and Bragg Brentano ($\theta/2\theta$) were used. For the first configuration GI the diffracting planes are at an angle of $\frac{1}{2}(2\theta) - \Omega$ to the normal of the surface film, whereas in the second $\theta/2\theta$ the diffracting planes are parallel to the surface film.

Using Jade 6.0 computer software the *XRD* patterns were fitted in order to obtain the peak position, integral breadth and the integrated peak surface (peak intensity). The width of the peak is an integral convolution of the instrumental broadening, of the broadening caused by the finite size of the crystallites and that from the random strain of the lattice. The instrumental width was removed automatically using an *XRD* pattern of a reference sample, powder of Y_2O_3, recorded in the suitable configuration, GI or $\theta/2\theta$.

In this work, the average crystallite size (*D*) value was calculated according to Scherrer's formula

$$D = \frac{K.\lambda}{\beta.\cos\theta}$$

here β is the integral breadth and *K* a constant which depends on the crystallites shape (0.9 value is used in this work). Even if this method does not take into account the contribution of the strain, in the width of the *XRD* peak, it gives a good estimation of the crystallite size especially for small crystallite size [3].

2.3.2.3. Scanning electron microscopy

In scanning electron microscopy (*SEM*), an electron beam with energies within 2 to 25 kV, scans the surface of the sample and the emitted secondary electrons are collected. The intensity of the collected electrons depends on the angle between the emitting surface and the detector. Regions in the specimen emitting an intense signal appear brighter than regions emitting a weaker signal. This contrast allows the formation of a surface image. The lateral resolution in *SEM*, in the range of 10 nm, limits the observations of nanostructures.

For our purpose, the fracture cross-section of NbN coatings was examined by *SEM* on a Philips XL 30 equipped with a field emission gun at accelerating voltage of 10 kV. *SEM* observations were done at the Centre Interdisciplinaire de Microscopie Electronique (CIME) at the EPFL. These observations give information on the film cross-section morphology.

2.3.2.4. Transmission electron microscopy

In transmission electron microscopy (*TEM*), electrons from the emission gun are transmitted through very thin sample (electron transparent), and generate an image of the internal structure of the sample. The resulting image displays structural details at very high spatial resolution, of the order of fractions of a nanometer [4].

In this work, the microstructure of the coatings was examined in cross-section by *TEM* on a Philips CM 300 equipped with a field emission gun at an accelerating voltage of 300 kV. Different types of contrast in the image, different observation modes have been employed: for diffraction (Bragg) contrast bright field and dark field images, for phase contrast: high resolution images. Selected area electron diffraction modes provide information about existing phases and preferential orientation of crystallites in the films. *TEM* observations were done at the Centre Interdisciplinaire de Microscopie Electronique (CIME) at the EPFL. Cross-section samples of films on WC-Co substrates were prepared by mechanically polishing down to a thickness of few µm. Further reduction of the thickness of a small region to roughly 20 nm was achieved by ion milling in a Gatan PIPS at 6-8° incident angle with Ar^+ ions at 2.5 kV.

2.3.2.5. Scanning tunneling microscopy

The principle of scanning tunneling microscopy (*STM*) consists in the fact that when electrically conducting tip is moved close enough to the surface of a conducting sample and a bias voltage is applied (typically between 1 mV and 4 V) to the tip a tunneling current of typically 0.1 to 10 nA can be generated. If this current is kept constant (constant current mode) the tip to surface distance must be unchanged. This allows to the formation of a topography image as the tip is scanned over the sample surface.

STM observations in this work were done using an Omicron STM-1 microscope, with a tungsten tip and a lateral resolution of about 0.1 nm in the constant current mode.

2.3.3. *Electronic properties*

2.3.3.1. Optical reflectivity and spectroscopic ellipsometry

In order to obtain the optical constants of the materials, the optical reflectivity and spectroscopic ellipsometry (*SE*) have been measured at room temperature.

The specular reflectivity was determined using a UV-VIS-IR spectrophotometer (CARY 500, VARIAN). The absolute specular reflectivity was measured at near normal incidence (7°), in the dual beam mode with a W shaped optical setup.

Reflection *SE* gives the values of the ellipsometric angles Ψ and Δ which reflect the change in polarization state due to sample-light interaction. In fact, the polarization state of an incident light beam changes after a reflection at the sample surface.

In this work, most *SE* measurements were accomplished on phase modulated ellipsometer (UVISEL, Jobin-Yvon) at an angle of incidence 70° for spectral range of 1.5-5.0 eV. For larger spectral range from 0.75 to 5 eV the *SE* were done on an ellipsometer (UVISEL HR 460, Jobin-Yvon), at Laboratoire de microstructuration et d'optoélectronique (LMSO) at the École d'Ingénieurs (EICN) in Le Locle

2.3.3.2. X-ray photoelectron spectroscopy

In X-ray photoelectron spectroscopy (*XPS*) technique, an incident X-ray on a sample leads to the ejection of a core level electron. The kinetic energy *KE* of the photoemmited core electron is

$$KE = h\nu - BE + \varphi$$

where $h\nu$ is the energy of the exciting radiation, *BE* is the binding energy of the emitted electron in the solid, and φ is the spectrometer work function [5].

In this work, *XPS* measurements were done using the incident radiation of Al K_α ($h\nu$ =1486.6 eV). For NbSiN samples, cleaned by Ar sputtering at 3 keV for 5 min before the measurements, the analyses were done using VG-ESCALAB MKII instrument at Surface Science Laboratory at KFUPM in Dhahran (Saudi Arabia). SCIENTA ESCA 300 was used for *XPS* analysis on freshly deposited NbN films, at Laboratoire de Spectroscopie Electronique at EPFL.

2.3.3.3. Fourier transform infrared spectroscopy

When irradiated with infrared light, a sample can transmit, scatter, or absorb the incident radiation. Absorbed infrared radiation usually excites molecules into higher–energy vibrational states. Infrared spectroscopy is useful for determining frequency of vibrations of chemical bonds [6].

A Nexus Fourier-transform infrared spectrometer was used to measure the transmission at normal incidence in the photon energy range from 400 to 4000 cm^{-1}. The instrument casing was constantly flooded with dry N_2 gas. The optical signature of silicon nitride vibrational modes in NbSiN films was checked by Fourier transform infrared spectroscopy (*FTIR*) in transmission mode.

2.3.3.4. Resistivity

The Van der Pauw method [7] allows measurements of the specific resistivity of a flat sample of arbitrary shape. A constant current (I_{12}) flows between the contacts 1 and 2, in the sample (figure 2). This induces potential drop between contacts 3 and 4 (V_{34}).

The resistance $R_{12,34}$ is defined as

$$R_{12,34} = \frac{U_{34}}{I_{12}}$$

The resistivity is given by

$$\rho_{DC} = \frac{\pi \cdot t}{\ln 2} \cdot \left(\frac{\mathrm{R}_{23,41} + \mathrm{R}_{12,34}}{2}\right) \cdot f\left(\frac{\mathrm{R}_{23,41}}{\mathrm{R}_{12,34}}\right)$$

where t is the film thickness and the function f represents a geometrical correction. It depends on the ratio $\mathrm{R}_{23,41}/\mathrm{R}_{12,34}$.

In this work, the resistivity was measured on films with a cross shape. The substrates were oxidized Si wafers (figure 2.2).

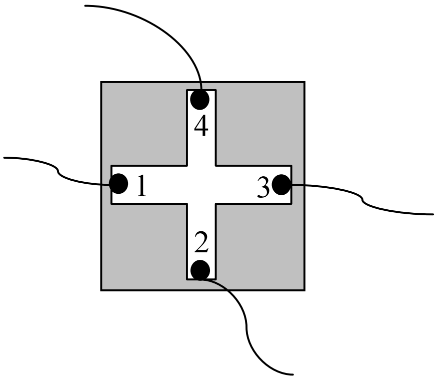

Fig. 2.2. Films cross on square oxidized Si (SiO_2/Si) substrate. 1, 2, 3, 4 are the contacts.

2.3.4. Mechanical properties

2.3.4.1. Nanoindentation

Many techniques exist for measuring the hardness of the materials. Nanoindendation technique is the appropriate one for thin films. The small loads (0.001-0.2N) used in this technique allow to measure the hardness down to a depth of 10% of the thickness. At this depth, the influence of the substrate on the hardness value is supposed to be negligible. Thus, the hardness measurement on a thin film (<5 µm) becomes possible. The hardness and Young's modulus are determined with a nanoindenter XP (Nano Instruments). A Berkovich-type pyramidal diamond tip indents the films to a maximum depth of 600 nm. Contact stiffness data were measured by oscillating the tip during indentation at a frequency of 65 Hz and amplitude of few nm. This kind of measurements provides hardness, Young modulus, and stiffness data throughout the whole indentation depth. In order to avoid the influences of the surface roughness and of the substrate, hardness values are taken where the hardness *vs.* depth has a plateau, at about 100-200 nm. In fact, the measured hardness at this depth is an indicative value of the intrinsic material hardness. The influence of the indenter size should be considered [8,9]. At least six indentations at different sites on the film have been performed and averaged.

2.3.4.2. Stress

The simplest and little time consuming method for measuring the residual stress (σ_{res}) in the film is the deflection technique. It consists in measuring the curvature radii of the sample before (r_b) and after deposition (r_a). The stress was then calculated using Stoney's formula

$$\sigma_{res} = \frac{E_s}{1-\upsilon_s} \cdot \frac{t_s^2}{6t_f} \cdot \left(\frac{1}{r_a} - \frac{1}{r_b} \right)$$

where $E_s/(1-\upsilon_s)$ is the biaxial modulus of the substrate, t_s and t_f are the substrate and coating thickness, respectively. In my work, the stress was determined on films deposited on Si strips (10×5×0.5 mm) using a laser beam (KLA TENCOR FLX-2320). The measure of the curvature radii of the substrates reveled that r_b is in the order of 100m and that r_a is in the ordre of 1m. Thus,

$$\frac{1}{r_a} - \frac{1}{r_b} \approx \frac{1}{r_a}$$

this implied no need to measure every time the substrate curvature before deposition.

References of chapter 2

[1] F.R. Bunshah, Deposition Technologies of Films and Coatings, Noyes, Park Ridge, NJ (1982).
[2] W-K Chu in Metals Handbook 9th ed. 10 Materials Characterization 328, American Society for Metals, (1986).
[3] A. Niederhofer, P. Nesladek, H.-D. Männling, K. Moto, S. Veprek and M. Jile, Surf. Coat. Technol. 120–121 (1999) 173.
[4] A.D. Roming in Metals Handbook 9th ed. 10 Materials Characterization 429, American Society for Metals, (1986).
[5] J.B. Lumsden in Metals Handbook 9th ed. 10 Materials Characterization 568, American Society for Metals, (1986).
[6] C. Marcott in Metals Handbook 9th ed. 10 Materials Characterization 109, American Society for Metals, (1986).
[7] L.J. van der Pauw, Philips Technical Review 20 (1958/1959) 220.
[8] S. J. Bull, J. Vac. Sci. Technol. A 19(4) (2001) 1404.
[9] S. Veprek, S. Mukherjee, P. Karvankova, H.-D. Männling, J. L. Moto and J. Prochazka, J. Vac. Sci. Technol. A 21(3) (2003) 532.

Chapter 3

Binary niobium nitride NbN$_x$ thin films

In this chapter, the first section reports on the influence of the deposition parameters on the phase and chemical composition whereas the second part presents the microstructure, electronic properties, mechanical properties and stability of the deposited NbN$_x$ thin films. The properties and results of the characterization of the single phases are reported first. They precede those presented for the mixed phases.

3.1. Influence of deposition parameters (P_{N2},T_s) on composition and crystalline structure of NbN_x films

In contrast to group IV metal nitrides where the cubic δ-MeN phase is homogenous on a wide range of nitrogen content, the Nb-N system crystallizes in several phases [1]. Levinskiy [2] reported two phase diagrams. The first isobaric diagram mentions the solid phases β-Nb_2N, δ-NbN, γ-Nb_4N_3 and ε-NbN. The second isobaric diagram established at 10^2 Pa is much simpler and contains β-Nb_2N and γ-Nb_4N_3. Recently, Lengauer et al. [3] reported the presence of solid phases β-Nb_2N, δ-NbN, γ-Nb_4N_3 and η-NbN in the Nb-N phases diagram.

In this work only three Nb-N phases, hexagonal β-Nb_2N and δ′-NbN and cubic δ-NbN were deposited. The elementary cell of these structures is illustrated in figure 3.1.

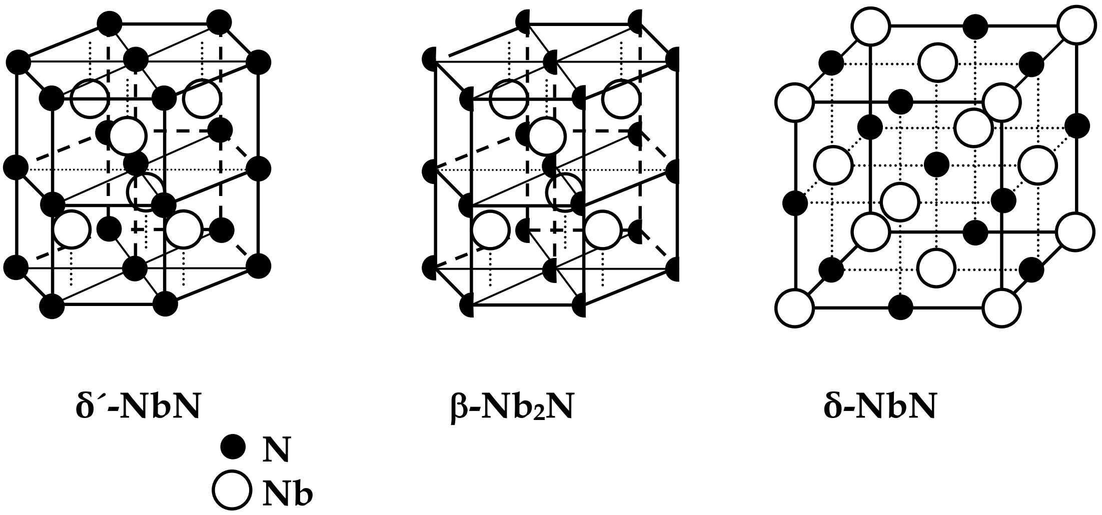

Fig. 3.1. Elementary cell of the crystalline structure of the three deposited Nb-N phases, hexagonal δ′-NbN and β-Nb_2N and cubic δ-NbN. For β-$Nb_2N$the notation ◖ means that only half of the nitrogen sites are occupied [4].

The phase identification of NbN_x films requires special care because of the superposition of the majority of the peaks from hexagonal phases δ′-NbN (PCPDF file 14-0547) and ε-NbN (PCPDF file 20-0801). A similar source of uncertainty occurs for the cubic δ-NbN phase (PCPDF file 38-1155) and the tetragonal γ-Nb_4N_3 phase (PCPDF file 20-0803) because of the shift of the peaks due to the presence of stress and broadening as a result of the small grain size.

The crystal structure of NbN$_x$ thin films, deposited at room temperature (RT) and at various nitrogen partial pressure P_{N2} (3%≤ P_{N2} ≤21%), changes from mixed (β+δ) phases to mixed (δ+h) phases (h: hexagonal ε or δ′) through a single cubic δ phase, with increasing P_{N2} (figure 3.2a and b). For films deposited at P_{N2} = 3% (x =0.61) most of the peaks can be attributed to either δ or β phase. It is really difficult to identify exactly the peaks in the X-ray diffraction diagrams. Nevertheless, the peaks at ~40° (figure 3.2a,b) and at 120°(figure 3.2a) are distinctive peaks of the δ phase.

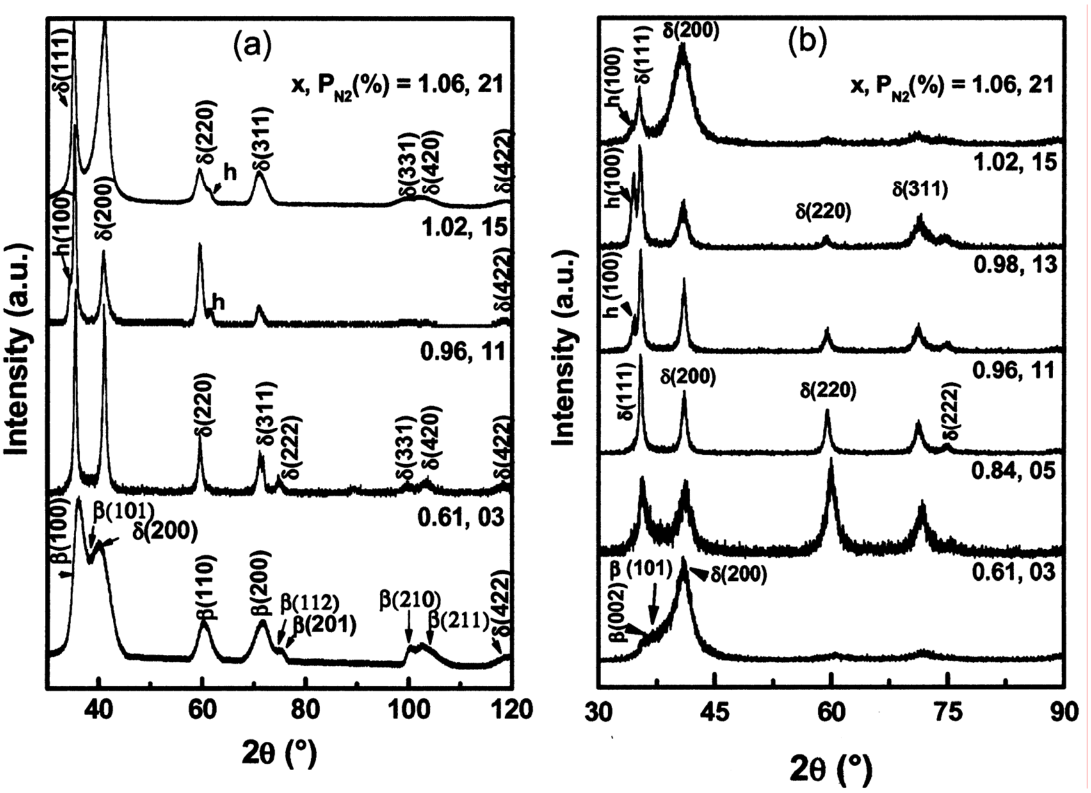

Fig. 3.2. XRD patterns (a) in grazing incidence configuration (γ=4°) (b) Bragg-Brentano, of NbN$_x$ films deposited at room temperature and different ratios x = N/Nb with various P_{N2}.

Due to the stoichiometric ratio x =0.61 of this film close to that of β-Nb$_2$N (PCPDF file 40-1274) and because of the optical properties (see 3.3.1.2) the majority of the peaks are attributed to the β phase. For films with 0.98≤ x ≤1.06, XRD does not allow distinguishing the precise nature of the hexagonal (h) structure. In fact, the small peak at 2θ ≈62.5° corresponds to either hexagonal δ′-NbN or hexagonal ε-NbN structures.

The crystal structure of NbN$_x$ films, deposited at various substrate temperature T_s (RT to 400°C) and at P_{N2} =15% changes from mixed (δ+h) phases to mixed (δ+δ′) phases with increasing T_s (figure 3.3). The XRD peak lying at ~115° is distinctive (212) peak of the δ′ phase.

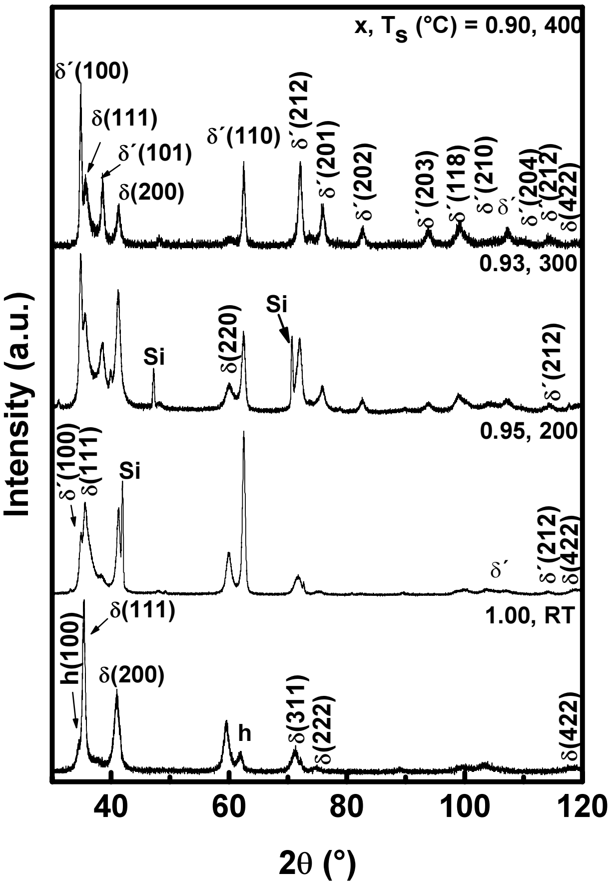

Fig. 3.3. XRD patterns, in grazing incidence configuration (γ = 4°), of NbN$_x$ films deposited at P_{N2} =15% and various T_s with different ratios x = N/Nb.

Increasing T_s favors the growth of the δ′ phase. The concentration of the hexagonal δ′-NbN (δ′[%]) phase in the film increases with increasing T_s (figure 3.5a). The δ′[%] was calculated following the formula

$$\delta'[\%] = \frac{\sum I_{\delta'}}{\sum I_{\delta'} + \sum I_{\delta}}$$

where $\sum I_{\delta}$ and $\sum I_{\delta'}$ are the sum of the intensities of δ cubic peaks and hexagonal δ′ peaks of the XRD measured in grazing incidence (γ=4°), respectively. The stability of the different NbN_x phases will be discussed in section 3.3.1

The crystal structure of NbN_x thin films, deposited at substrate temperature T_s =400°C and at various nitrogen partial pressures P_{N2} ($7\% \leq P_{N2} \leq 40\%$), changes from mixed (β+δ) phases to a single δ phase through a mixture (δ+δ′) with increasing P_{N2} (figure 3.4). For films with x =0.57 and 0.64 most of the XRD peaks have been identified as β-Nb_2N peaks, because of their stoichiometric ratio x approaching 0.5 (value for Nb_2N). The optical measurements confirm that result (see 3.3.2). The evolution of the δ′ [%] as function of x is shown in figure 3.5b.

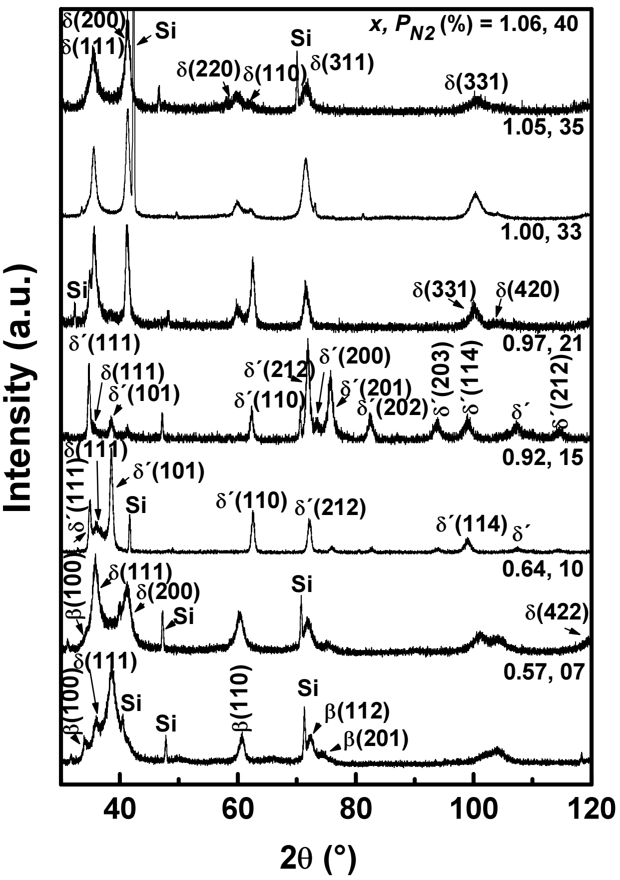

Fig. 3.4. XRD patterns, in grazing incidence configuration (γ = 4°), of NbN_x films deposited at 400°C and various nitrogen partial pressure P_{N2} with different stoichiometric ratios x = N/Nb.

The phase domains of sputter deposited NbN_x films, as a function of the nitrogen partial pressure and substrate temperature, are shown in figure 3.6.

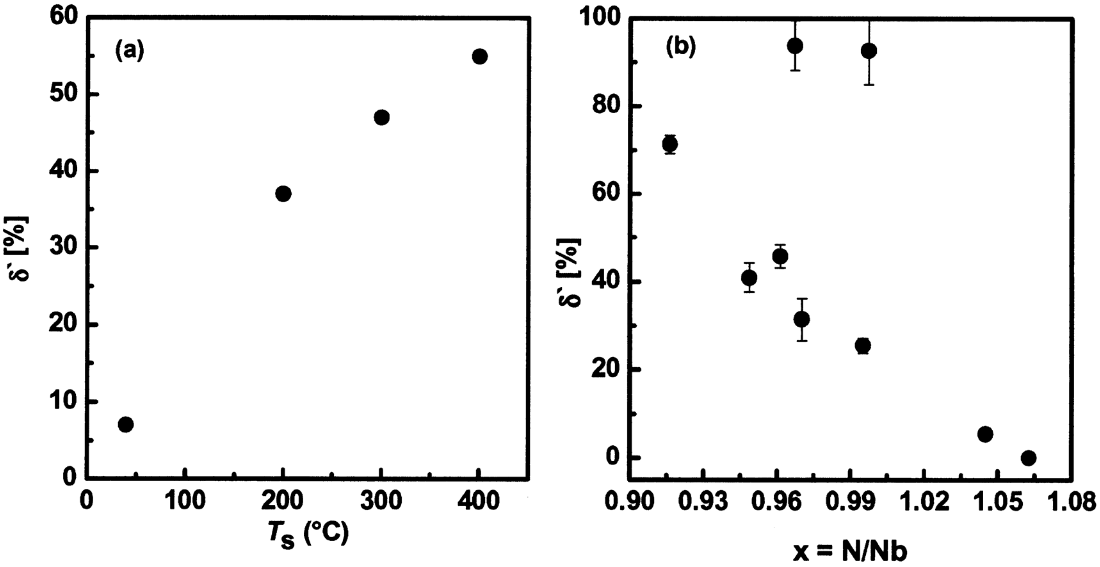

Fig. 3.5. NbN thin films: Concentration of the hexagonal phase δ' *as a function of (a)* T_s, P_{N2}=15% *and (b) x,* T_s = 400°C *with various* P_{N2}, *respectively.*

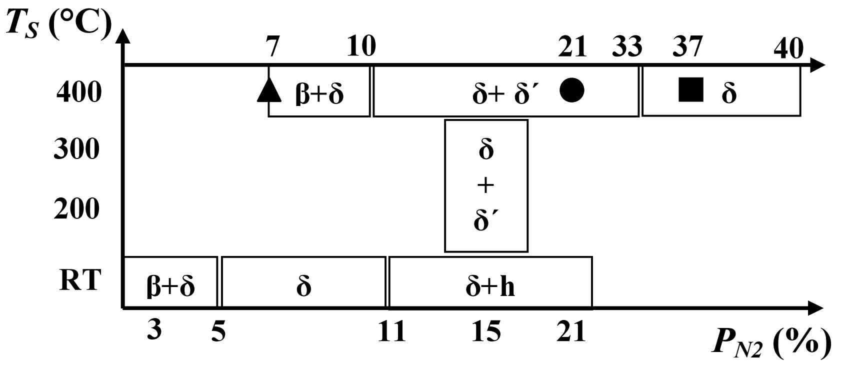

Fig. 3.6. Phase composition of Nb-N film system depending on the nitrogen partial pressure P_{N2} *and substrate temperature* T_s. ▲,● *and* ■ *represent positions of single* β, δ' *and* δ *(used for the study of single phases), respectively. The boundaries are approximate.*

The single phase NbN_x films were chosen from the series of NbN_x films deposited at T_S =400°C. In figure 3.6 the position of these single phases are noted. As just a small peak lying at ~35° of the second δ phase was observed in the films deposited at P_{N2} =7 and 21% (figure 3.4), the crystal structure was considered as single β and δ′ phase, respectively. The deposition conditions of the investigated single phase films are summarized in Table 3.1.

Table 3.1 Deposition parameters (T_s, P_{N2}), ratio x=N/Nb, lattice parameters (a,c), grain size and ratio between the measured and the theoretical density(d_{mea}/d_{theo}) of selected single phases: δ-NbN, β-Nb_2N and δ′-NbN thin films

Phases	**T_s (°C)**	**P_{N2} (%)**	**x (±1 %)**	**a (nm)**	**c (nm)**	**Grain size (nm)**	**d_{mea} / d_{theo}**
β-Nb_2N	400	7	0.57	0.305	0.500	6	0.96
δ′-NbN	400	21	0.97	0.299	0.535	26	0.86
δ-NbN	400	37	1.06	0.438	--	6	0.8

3.2. Microstructure

3.2.1. Single NbN_x phases

Series of 200 × 200 nm^2 scanning tunneling microscopy (STM) images of the surface of β-Nb_2N, δ′-NbN and δ-NbN phase films are shown in figure 3.7a, b and c, respectively. The surface topography looks different. The surface morphology of β-Nb_2N phase film is characterized by dense clusters composed of small grains (6-10 nm). The granular morphology of δ′-NbN phase film is different (figure 3.7b): large compact clusters (80-100 nm) with crystal grains of 20-30 nm are observed.

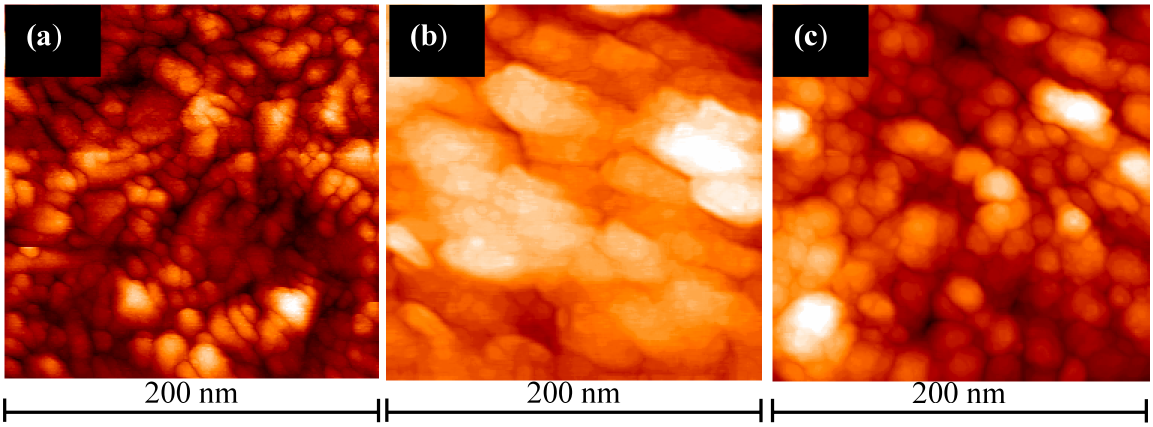

Fig. 3.7. STM images of hexagonal β-Nb_2N (a), hexagonal δ′-NbN (b) and cubic δ-NbN (c) films.

The surface morphology of the cubic δ-NbN phase films exhibits a structure with crystallites ranging from 10 to 20 nm. In good agreement with the XRD results, the smallest average lateral grain size is observed for β-Nb_2N films and the highest for δ′-NbN phase film.

Cross-section transmission electron microscopy (TEM) and high resolution transmission electron microscopy (HRTEM) investigations were done to investigate more precisely the microstructure of the single phase films. Conventional TEM contrast images of the three single phase films are presented in figure 3.8. The microstructure of the three single phases is columnar. Each column is formed by agglomerates of crystallites (figure 3.8). The column width is 15-30 nm in the β-Nb_2N films and 40-70 nm in the δ′-NbN films. In the case of the hexagonal phase films (figure 3.8a, b), the columns can be easily distinguished. These films show well-defined crystalline orientation in the column. For cubic films (figure 3.8 c) the overall texture is well pronounced, but inside the same column the crystallites have different orientations. Consequently, the diffraction contrast increases inside the column and practically disappears between the columns (figure 3.8 c).

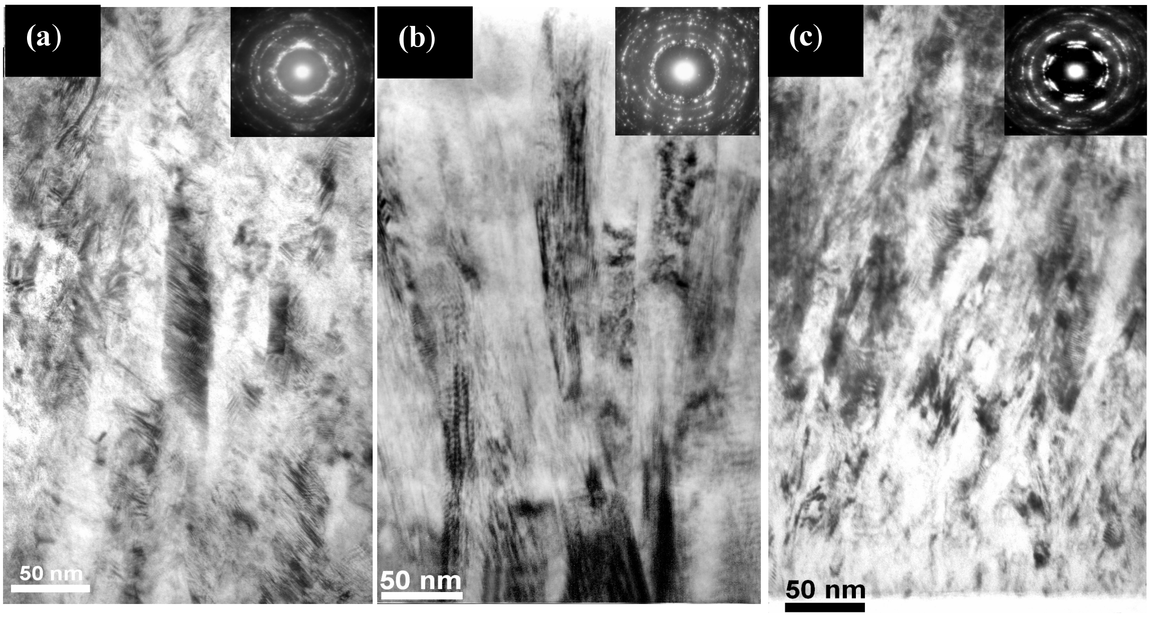

Fig 3.8. TEM images and corresponding SAED patterns for hexagonal β-Nb_2N (a), hexagonal δ′-NbN (b) and cubic δ-NbN (c) films.

In the β-Nb_2N phase films, the columns morphology shows interesting features (figure 3.9). In the contrast image the column looks like a feather: thin needle-shaped crystallites oriented at approximately 30° and 50° relatively to the growth direction. The needle-shaped crystallites are 2-3 nm large and 15-30 nm long. In such columns the crystallites keep one common direction. The HRTEM images confirm that the columns of β-Nb_2N films contain multi-twin successions (figure 3.9a). The HRTEM images of δ′ and δ phase films (figure 3.10b, c) show large crystal domain. Twins or dislocations were not observed in these films.

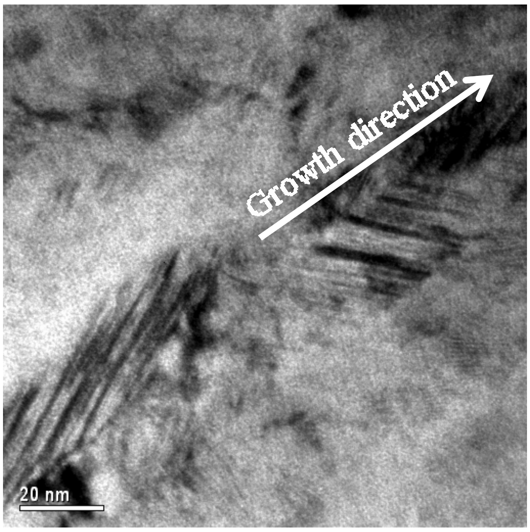

Fig. 3.9. TEM image: column detail into hexagonal β-Nb_2N phase film.

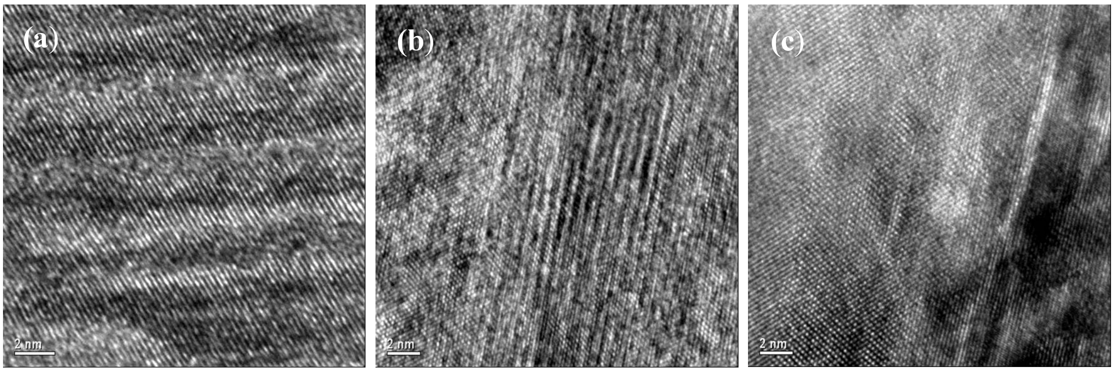

Fig. 3.10. HRTEM images for hexagonal β-Nb_2N (a) hexagonal δ′-NbN (b) and cubic δ-NbN (c) films.

3.2.2. Mixed NbN$_x$ phases

Scanning electron microscopy (*SEM)* micrographs show the fracture cross section of three NbN$_x$ coatings deposited at RT and various P_{N2} (figure 3.11).

The morphology evolution of these films appears to be controlled by the chemical composition x. Films with x = 0.61 and 1.06 are compact with small grain size (figure 3.11a, c). Nevertheless, their fracture cross section is different. With x approaching 0.97, the morphology becomes columnar with more voids (figure 3.11b). The grain size perpendicular to the plane of the substrate has been estimated from the integral width of the XRD peaks, in Bragg-Brentano configuration (figure 3.12). At x =0.61 the film presents a small grain size (~4 nm), this is probably due to the presence of two phases (β+δ) in the film. Single δ phase film with x-0.85 also shows a small grain size (~5 nm).With increasing x up to ~0.96 the grain size increase up to 16 nm. At x ~0.97 the second δ′ phase appears which reduces the grain size down to 4 nm.

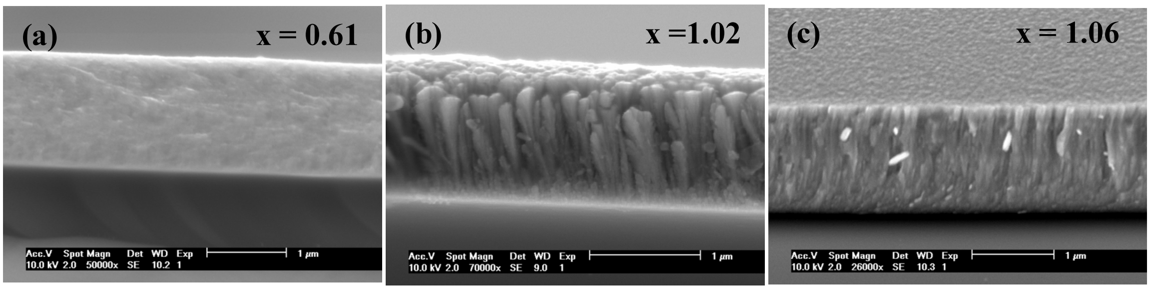

Fig. 3.11. Scanning electron micrographs of the cross section of NbN$_x$ films, deposited at RT and various P_{N2}, for three different ratios x = N/Nb.

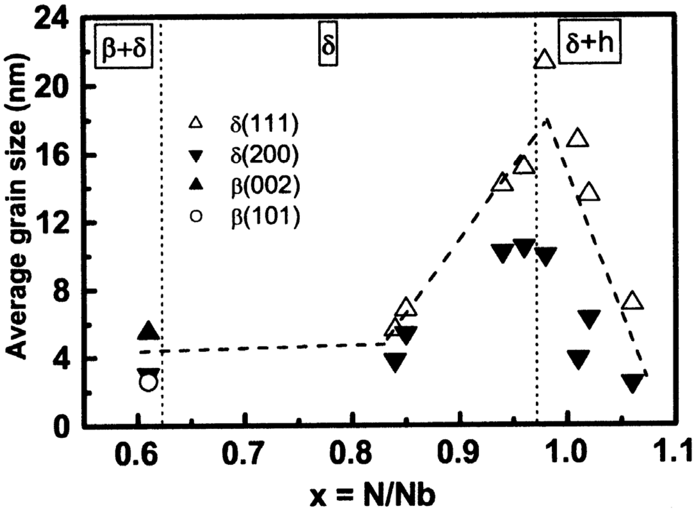

Fig. 3.12. Average grain size of NbN$_x$ films, deposited at RT and various P_{N2}, for different ratios x = N/Nb. The dashed line follows values of grain size as a guide for the eye.

SEM micrographs of films deposited at P_{N2} =15% and at different substrate temperatures T_s are shown in figure 3.13. Fracture cross section of films deposited at low T_s reveals a brittle microstructure (figure 3.13a). In contrast, the microstructure of the film deposited at high T_s is compact (figure 3.13b). For T_s > 200°C, the grain size of the hexagonal δ′ phase rapidly increases, with increasing T_s (figure 3.14b). Heating the substrate increases the mobility of the adatoms which increase the density of the film as it appears in figure 3.13. In additions, the change in the crystal structure from cubic δ-NbN to hexagonal δ′-NbN, with increasing T_s, can also be responsible on the increase in the films density and grain size.

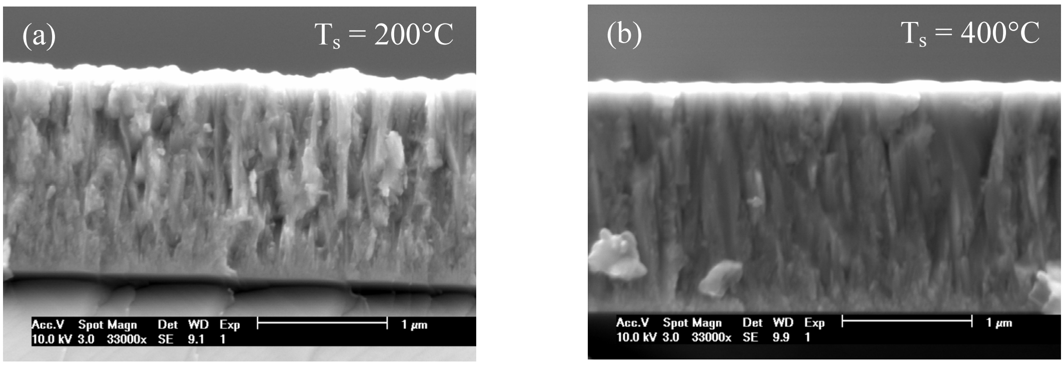

Fig. 3.13. Scanning electron micrographs of the cross section of NbN_x films, deposited at P_{N2} =15% and T_s.=200°C (a) and 400°C (b).

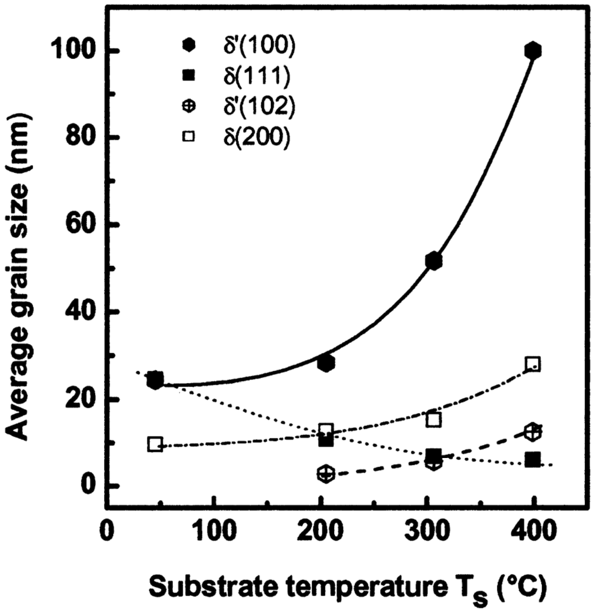

Fig. 3.14. Average grain size of NbN_x films, deposited at P_{N2} =15% as a function of the substrate temperature T_s.

SEM micrographs of films deposited at T_s =400°C and various P_{N2} are shown in figure 3.15. It appears that the morphology of these films is controlled by the content of the δ′ phase in the film. At low δ′ phase content (below 50%) the films morphology is non compact and brittle (figure 3.15a). Whereas, for higher δ′ content (above 50%), the morphology becomes denser with well defined columnar structure (figure 3.15b, c).

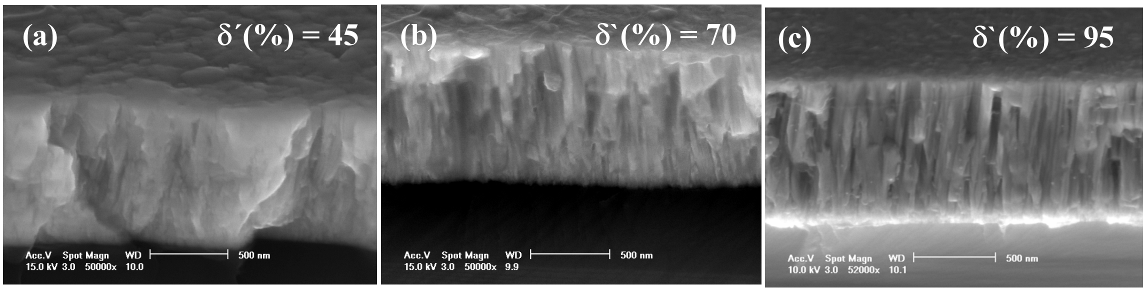

Fig. 3.15. Scanning electron micrographs of the cross section of NbN_x films, deposited at T_s =400°C and various P_{N2}, containing different hexagonal δ′ phase content.

3.3. Electronic properties

3.3.1. Single NbN_x phases

3.3.1.1. Electrical resistivity

Figure 3.16 shows the dc electrical resistivity $\rho_{dc}(T)$ as a function of the temperature of hexagonal δ′-NbN and β-Nb_2N, cubic fcc δ-NbN thin film. For pure δ'-NbN, the resistivity monotonously increase, as the temperature increases, exhibiting a metallic behavior; with a residual resistivity ratio (RRR) ρ_{RT}/ρ_{20K}=1.3. The room temperature resistivity ρ_{RT} is about 90 μΩcm. The metallic behavior is less pronounced for β-Nb_2N, the ρ_{RT} of these thin films is in the range of 160 μΩcm and the resistance ratio ρ_{RT}/ρ_{20K} close to unity. The cubic δ-NbN thin films exhibit the highest ρ_{RT} values, typically 250 μΩcm, and a negative temperature coefficient of resistivity with a RRR, ρ_{RT}/ρ_{20K}=0.76. Only the cubic δ-NbN films exhibit the transition to the superconducting state at the critical temperature T_c =11K with a narrow range of the transition temperature of 1 K. The unusual nonmetallic conduction, which is often observed in these polycrystalline films, is ascribed to the grain boundary and point defect scattering effect [5-8].

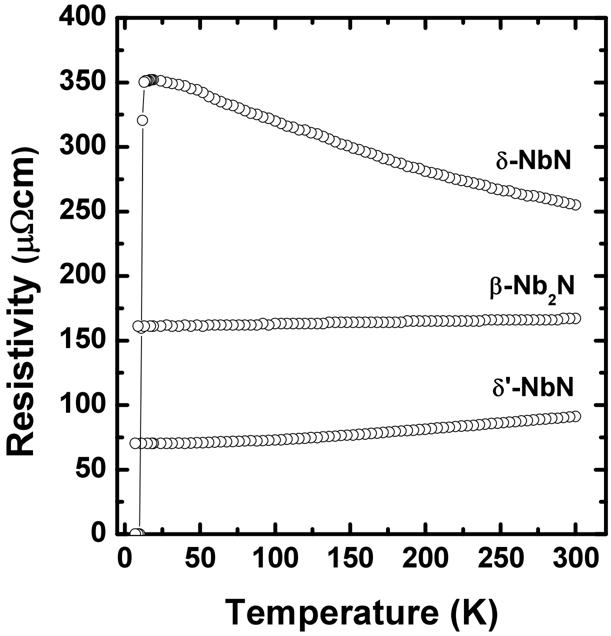

Fig. 3.16. Resistivity vs. temperature of single phases films: hexagonal δ′-NbN and β-Nb$_2$N, and cubic δ-NbN.

The low ρ_{RT} values observed in the case of the hexagonal δ'-NbN$_x$ thin films are related to their good crystalline quality and large grain size (26 nm) compared to that of the δ-NbN phase (6 nm) (Table 3.1).

Oya et al. [9] report a T_c of ~11 K for δ-NbN$_{1.2}$ films deposited on MgO substrate. On the contrary, the mixed films of γ-Nb$_4$N$_3$+δ′-NbN$_x$ do not exhibit superconductivity down to 1.77 K. Tanabe et al. [10] reported a value of ρ_{RT} = 117 and 176 μΩcm and an RRR of 0.94 and 0.83 for β or α + δ and δ films, respectively. Konevecki et al. [11] reported ρ_{RT} of 226-394 μΩcm and a T_c of 12.9-14.4 K for NbN films without checking of the crystalline structure.

3.3.1.2. Optical properties

Typical optical reflection spectra of hexagonal β-Nb$_2$N, δ′-NbN and cubic fcc δ-NbN, are shown in figure 3.17 as a function of the photon energy $\hbar\omega$ over the range from 0.5 to 6.5 eV. The highest reflectivity at low energy is achieved by the cubic δ-NbN sample. In this sample the minimum reflectivity value of 0.30 is observed at $\hbar\omega$=3.8 eV. The reflectivity spectrum of the β-Nb$_2$N sample is characterized by a continuously decreasing reflectivity values from 0.77 down to 0.37 as the photon energy increases from 0.46 to 6.5 eV, a weak reflectance edge is observed at about 4.5 eV. The reflection spectrum of the δ′-NbN sample is characterized by a sharp drop in reflectivity with a minimum reflectivity of 0.37 lying at 1 eV and by features located at 2.5 eV, 4 eV and 6.25 eV.

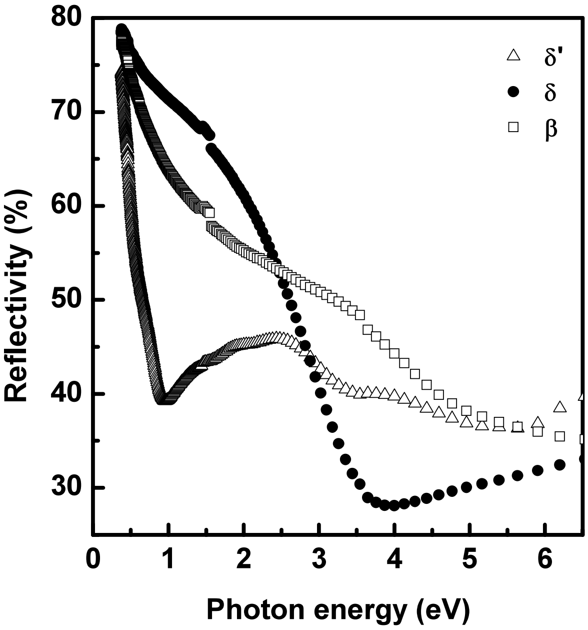

Fig.3.17. Reflectivity spectra of single phases: δ-NbN, β-Nb$_2$N and δ′-NbN.

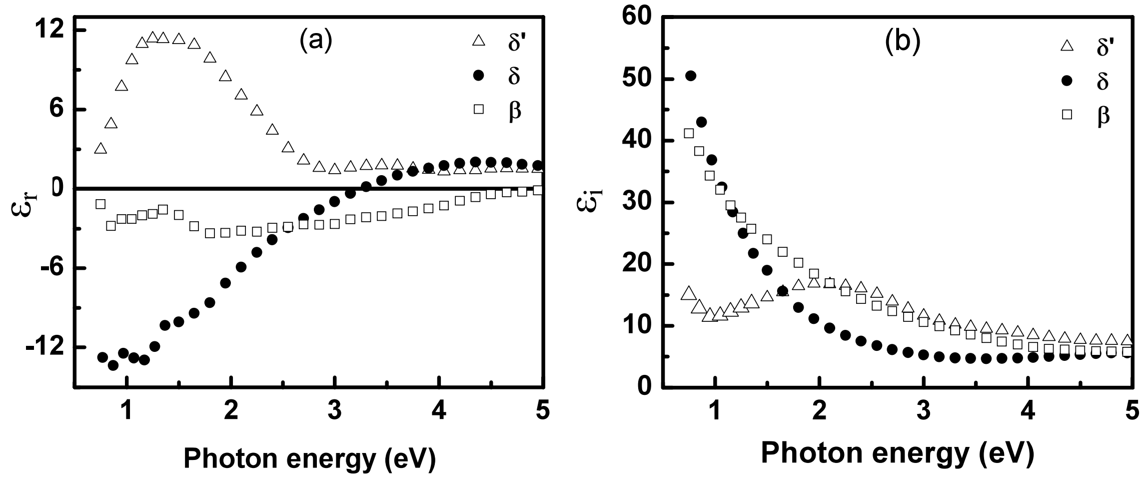

Fig. 3.18. Dielectric function spectra of single phases: δ-NbN, β-Nb$_2$N and δ′-NbN. a) real part ε_r and b) imaginary part ε_i.

The reflectivity measurements were complemented by spectroscopic ellipsometry (*SE*) measurements in the energy range extending from 0.75 to 5.5 eV. Since, the NbN$_x$ films with a thickness of 1-2 μm are opaque for ellipsometric measurements, in this range of photon energy, a semi-infinite model was used for calculation of the complex dielectric function $\varepsilon(\omega)=\varepsilon_r(\omega)+i\varepsilon_i(\omega)$ of the bulk film without any contribution from the substrate. The real ε_r and the imaginary ε_i parts of the dielectric function are represented in figure 3.18. Both the δ-NbN and the β-Nb_2N phases exhibit a Drude like behaviour with screened plasma energies $\hbar\omega_s$ =3.2±0.1 eV and 4.7±0.3 eV, respectively. In the case of the hexagonal δ'-NbN, the dielectric function spectra ε_r remains positive over the entire photon energy range and shows a prominent feature which can be attributed to interband transitions centered at about 1.5 eV. ε_i indicates resonance peaks located at 1.5 eV, 2 to 2.6 eV and 3.6 eV.

In order to obtain the electronic parameters of the δ-NbN, β-Nb_2N and δ′-NbN phases, the measured reflectivity and dielectric function were simultaneously fitted following an established analysis procedure [12]. The fit has been achieved with considering the contributions of intraband and interband transitions described by a Drude term and a set of three Lorentz oscillators, respectively:

$$\varepsilon(\omega) = \varepsilon_\infty - \frac{\omega_p^2}{\omega^2 + i\Gamma_p\omega} + \sum_k \frac{\omega_k^2}{\omega_k^2 - \omega^2 + i\Gamma_k\omega}$$

where ε_∞ is a constant accounting for all higher-energy interband transitions that are not taken into account in the Lorentz terms. The Drude term is characterized by the plasma frequency ω_p and the damping factor Γ_p. The physical parameter obtained from the Drude-Lorentz analyses are the effective optical free electron density $N^* = N/(m_e^*/m_e)$ given by

$$N^* = \frac{\varepsilon_0 m_e \omega_p^2}{e^2}$$

and the free electron relaxation time $\tau = \hbar/\Gamma_p$; where m_e (m_e^*) and e are the mass (effective mass) and the charge of the electron, respectively. The optical resistivity is calculated by $\rho_{opt} = \Gamma_p/\varepsilon_0\omega_p^2$. Table 3.2 illustrates the values of the physical parameters of NbNx phases deduced from the fit. The cation density in stoichiometric δ-NbN and δ′-NbN is about n = 4.6 10^{22} cm^{-3} whereas for β-Nb_2N, it is 5.6 10^{22} cm^{-3}. Under the assumption that each Nb atom provides 3 electrons to the N 2p bands and two electrons to the 4d conduction bands, the charge carrier density N_{cal} was calculated (Table 3.2).

Table 3.2 *Physical parameters ($\hbar\omega_p, \Gamma_p, \tau$, N^*) deduced from the fit of measured optical properties, calculated carrier charge density (N_{cal}) and calculated optical(ρ_{opt}) and DC measured resistivity ρ_{DC}) for single phase: δ-NbN, β-Nb_2N and δ′-NbN thin films.*

Phases	$\hbar\omega_p$ *(eV)*	Γ_p *(eV)*	τ *(10^{-15} s)*	N^* *(10^{22} cm^{-3})*	N_{cal} *(10^{22} cm^{-3})*	ρ_{opt} *(μΩcm)*	ρ_{DC} *(μΩcm)*
δ-NbN	5.8	0.65	0.66	2.44	9.2	140	260
β-Nb_2N	6.6	1.0	1.31	3.16	11.2	170	170
δ′-NbN	3.8	0.5	1.01	1.05	9.2	260	90

The optical resistivity (ρ_{opt}) is in a good agreement with the measured one (ρ_{DC}) for the β phase. For the cubic δ phase ρ_{opt} is lower than the ρ_{DC}. Due to the influence of the grain boundaries on the DC measured resistivity, ρ_{DC} is always larger than ρ_{opt}. The value of ρ_{opt} is higher than ρ_{DC}, for the hexagonal δ′ phase.

In fact, it is difficult to extract the Drude term from the optical response of transition metal compound where d-bands play an important role. In particular, this causes problems when attempting to match the DC conductivity with the extrapolation to zero frequency of the optical conductivity $\sigma_{opt} = \varepsilon_0 \varepsilon_i \omega$, e.g. the σ_{opt} of Pt increases by a factor of 3 with increasing $\hbar\omega$ from 0 to 0.3 eV [13]. In such case it is crucial to measure the optical values in the infrared, and to include interband contributions when analyzing the dielectric function. This is the most likely reason why the DC conductivity of the hexagonal δ′-NbN phase film is apparently higher than the optical value. For a similar reason the apparent equality between optical and DC conductivity found for the δ and β phases films of the present study is fortuitous and actually points an inaccurate evaluation of the optical conductivity.

According to the band structure calculations reported for cubic δ-NbN [14], the lower direct gaps of interband transitions at the Γ and X points are in the range of 2 to 4 eV, close to the reflection edge. Thus the Drude free electron energy range coincides with the energy of these interband transitions. In the case of the hexagonal β-Nb_2N, the shift of the screened plasma energy toward to higher energy value (4.5 to 5.0 eV) suggests reduced interband transition effects. In the case of the hexagonal δ′-NbN, the screened plasma energy is well lowered down to about 0.7 eV (as the extrapolation of the ε_1 curve suggests in figure. 3.18). Consequently, the observed features located at 1.5 eV, 2-2.6 eV and 3.6 eV in the dielectric function as well as in the reflectance spectra are tentatively associated with interband transitions. Theoretical DOS calculations exhibit two peaks located at 2 and 3.5 eV above the Fermi level (antibonding states) arising predominantly from Nb 4d derived states weakly mixed with N 2p states (figure 3.22). Thus, the observed features can be attributed to transitions between occupied states near the Fermi level to unoccupied hybridized Nb 4d and N 2p states. In addition, the Fermi level is seen to lie near a pronounced minimum in the density of states (DOS) (figure 3.21.).

Only one report can be found in the literature on the optical properties of the δ-NbN phase. K. Tanabe et al. [6] report for the plasma photon energy $\hbar\omega_p$=3.47 to 3.53 eV and Γ_p of 0.3-0.4 eV. These values were determined by fitting the reflectivity spectra without taking into account the interband transitions. This explains why the values of $\hbar\omega_p$ and Γ_p are lower than those found in the present study.

3.3.1.3. XPS Valence band spectra

Figure 3.19 shows the XPS valence band (VB) spectra recorded for hexagonal β-Nb_2N, and δ′-NbN and cubic δ-NbN phase. The VB energy distribution curve (EDC) of the cubic δ-NbN phase is mainly dominated by three peaks centered at 17 eV, 6.5 eV and 1.5 eV. The EDCs of the hexagonal phases are also characterized by three emission structures located at about 17.5 eV, 6 eV and 2 eV below the Fermi level (E_F), but they significantly differ from those of the cubic phase. The partial DOS calculated by Music et al. [15] (Figure 3.22) allows to identify these peaks as arising from N 2s states degenerated with Nb 4d and Nb 4p states (region I), strongly hybridized N 2p - Nb 4d states (region II), and from predominantly Nb-4d states weakly mixed with N 2p states (region III), respectively. By studying differences and changes in these three regions, valuable information concerning the bonding character of the three different phases can be extracted.

To provide a more precise description of the variations between the EDC of the cubic and hexagonal phases, difference data were obtained by subtracting the spectra of the hexagonal phases from the spectrum of the cubic phase. Similar procedure was also applied in comparing the two hexagonal phases (figure 3.20). The spectra were normalized to the intensity of the corresponding N 2s for the hexagonal δ′-NbN and cubic δ-NbN nitrides while for β-Nb_2N the N 2s was fixed to half intensity of that of the hexagonal δ′-NbN, thus they represent the VB DOS per nitrogen atom modulated by the respective photoionization cross-section of the involved levels of N and Nb atoms. In contrast to the featureless 6.5 eV and 1.5 eV peaks observed in the cubic phase, those of the hexagonal phases exhibit new features and strong intensity emission modifications. These features are labeled as d_1, d_2, d_3, p_1 and p_2 as shown in figure 3.20.

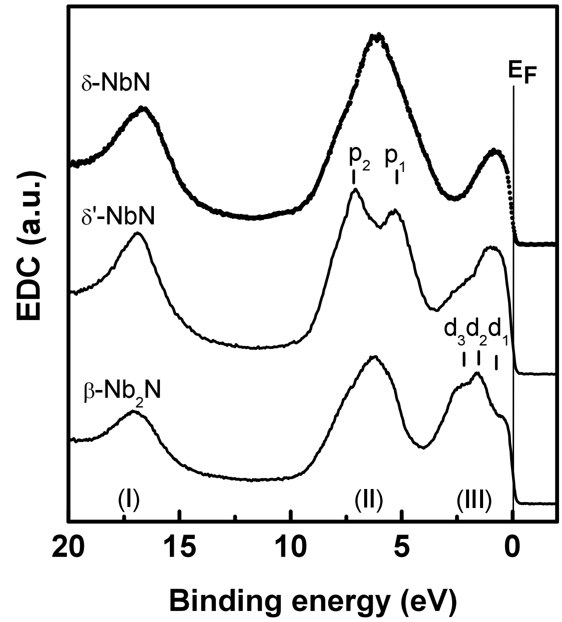

Fig. 3.19. Valence band spectra of hexagonal β-Nb_2N, δ′-NbN and cubic δ-NbN.

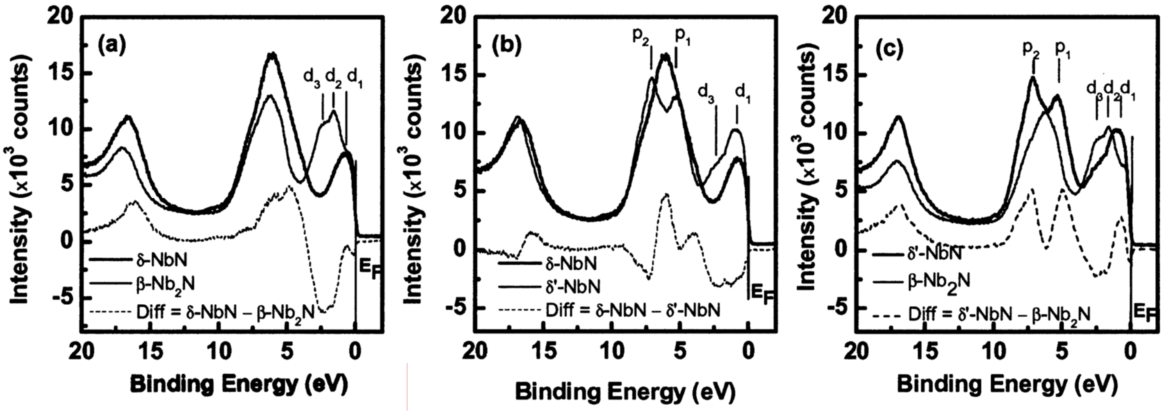

Fig. 3.20. Difference valance band spectra obtained by subtracting the data from each other.

In the case of the β-Nb_2N (figure 3.20a), in the region II the 6 eV peak is narrowed in comparison with the broad hybridized peak of the cubic phase while in the region III the peak located just below E_F exhibits strong broad emission and shows three structures: a shoulder at about 0.5 eV (peak d_1), a narrow peak at 2 eV (peak d_2) and a second shoulder located at 2.5 eV (peak d_3). With regard to the hexagonal δ′-NbN (figure 3.20b) the most striking feature in the VB region II is the splitting of the broad 6.5 eV peak in to two narrow peaks (peaks p_1 and p_2) located at 5.3 eV and 7.1 eV while the emission just below E_F is characterized by two structures: a broad peak arising at 1.5 eV (peak d_1) and a second one at 2.5 eV (peak d_3) which is noticeable as a shoulder on the right side of the peak d_1.

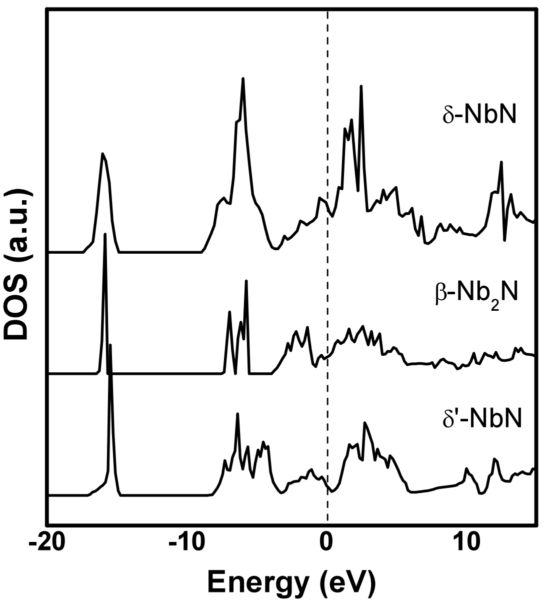

Fig. 3.21. Total density of states (DOS) for hexagonal β-Nb$_2$N, hexagonal δ′-NbN, and cubic δ-NbN, as obtained from the VASP code Fermi levels are set to 0 eV [15].

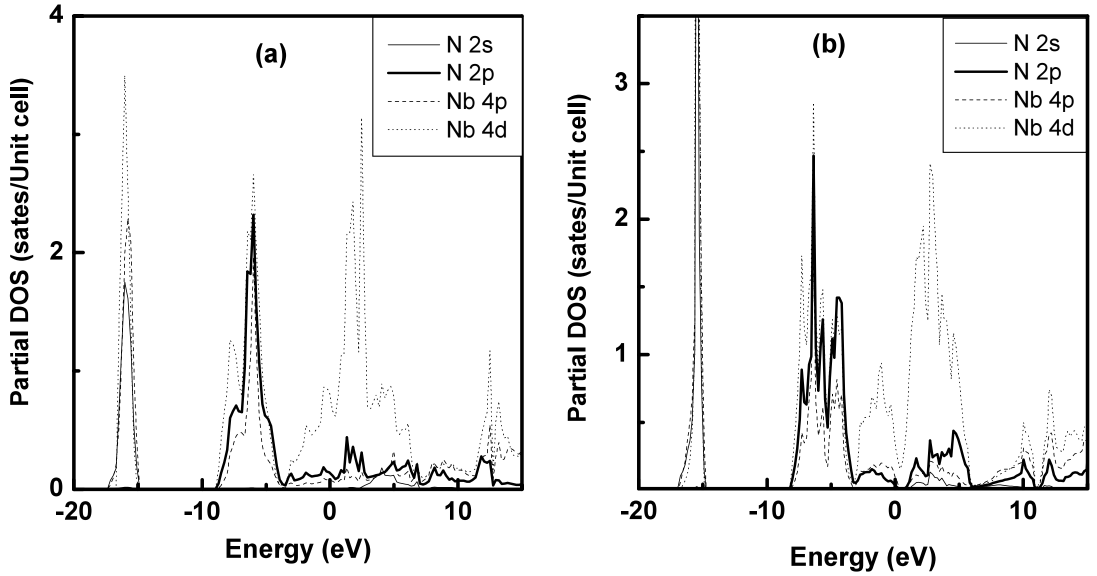

Fig. 3.22. Partial density of states (DOS) for (a) cubic δ-NbN and (b) hexagonal δ′-NbN, exemplifying the bonding in the studied binary nitrides. Fermi levels are set to 0 eV. [15]

The difference spectrum Diff = δ-NbN - β-Nb_2N exhibits a positive peak located at about 16 eV due to the difference in the N content between the two phases. The position of this peak at 16 eV results from the fact that the N 2s level in β-Nb_2N lies at slightly higher binding energy compared to that of the cubic δ-NbN. A similar feature is also observed in the difference spectrum Diff = δ-NbN-δ′-NbN. These trends indicate that both hexagonal β-Nb_2N and δ′-NbN phases are more covalent than the cubic fcc one.

In the VB region associated with the hybridized N 2p – Nb 4d orbitals and the predominantly Nb 4d states, the strong positive and negative differential intensities reflect important modifications of the partial (p-d)-like and d-like DOS in the VB structure due to the structural modifications going from the cubic to the hexagonal phases. In the case of hexagonal β-Nb_2N two strong emissions, peaks d_2 and d_3, appear in the region of nearly pure Nb 4d states (figure 3.20c). Considering δ′-NbN (figure 3.20a), the spectral contribution of peak d_2 vanishes, the contribution of the d_3 peak is decreased while that of the peak d_1 is increased. This can be explained by the dissimilarity of the first and the second as well as the third Nb-Nb coordination in the cubic and hexagonal structures. Furthermore, in the case of the hexagonal β-Nb_2N the degree of hybridization between the nonmetal and metal ions is decreased, approximately half of the emission vanishes in the right side of the hybridized region II (positive peak centered at about 5 eV, see figure 3.20) while in the case of δ′-NbN the p-d hybridization leads to the formation of two well separated (p-d) bands (figure 3.20b). The large redistribution of the VB states is associated with the low N content in the Nb_2N film and with the changes in the nearest neighbor coordination of N with Nb atoms (octahedral for the cubic and trigonal prismatic for the hexagonal). By comparing the two hexagonal phases (figure 3.20c), it appears that, if the β-Nb_2N is regarded as a simple defective δ′-NbN phase with N vacancies, a simple rigid band picture to describe the electronic structure of these nitrides is not appropriate. The d_2 and d_3 features observed at 2 and 2.5 eV below E_F, which have Nb-d character, can be considered as vacancy peaks emanating from Nb-Nb bonds through the nitrogen vacancy site. In this context, it is reported in the literature that states associated with the vacancy peaks in cubic nitrides lead to a reduction of the DOS at the Fermi level providing a phase stability mechanism [16]. In the case of hexagonal nitrides, the effects of vacancies on the relative stability of phases can be elucidated from the DOS. In stoichiometric δ′-NbN the Fermi level is located near a pseudo gap of the DOS (figure 3.21). In this case, the shift of the Fermi level towards higher DOS values or the introduction of vacancy states in the pseudo gap can lead to drastic lowering of the stability. This can explains the narrow composition range $0.97 \leq x \leq 1.0$ (see 3.1) observed for the critical stability of the δ′-NbN phase.

3.3.1.4. Core levels, charge transfer and ionicity

The binding energy values of N 1s and Nb $3d_{2/3}$ core levels, associated with the hexagonal β-Nb_2N and δ′-NbN and cubic δ-NbN nitrides, are given in Table 3.3. Reported are also the differences of binding energies, ΔBE, between the N 1s–Nb 3d levels. The difference of binding energies ΔBE is significant in order to avoid effects due to changes in crystal potential and reference level.

Table 3.3 *Binding energies of core levels of N 1s and Nb 3d, energy difference values ΔBE and hardness values of single phases: hexagonal β-Nb_2N and δ′-NbN, and cubic δ-NbN.*

Phases	*N 1s (± 0.05) eV*	*Nb $3d_{5/2}$ (± 0.05) eV*	*ΔBE (N 1s - Nb $3d_{5/2}$) (± 0.1) eV*
β-Nb_2N	397.90	203.56	194.3
δ′-NbN	397.77	204.10	193.7
δ-NbN	397.20	204.20	193.0

The chemical shift of core levels is interpreted in terms of changes in the charge distribution providing indication of the degree of ionicity and covalency of the bonding [17].

In the hexagonal phases, the N 1s and Nb 3d ΔBE values indicate that the covalency level in β-Nb_2N is slightly higher than that in δ′-NbN. Both the β-Nb_2N and the δ′-NbN are more covalent than the cubic δ-NbN. Consequently, the covalency level decreases in the order β-Nb_2N ≥ δ′-NbN > fcc-NbN according to the position of their N 1s level (397.90 eV for β-Nb_2N, 397.77 eV for δ′-NbN and 397.20 eV for fcc NbN).

3.3.2. *Mixed NbN_x phases*

The electronic properties of each single NbN_x phase provide bases for the interpretation of those of mixed phases.

The real part of the dielectric function (ε_1) and the reflectivity spectra of NbN_x films, deposited at *RT* and various nitrogen partial pressures P_{N2}, are shown in figure 3.23a and b, respectively. The film with x =0.61 shows optical properties like that observed in the β-Nb_2N phase. Thus, its crystal structure is confirmed to be β-Nb_2N. From XRD measurements only it was difficult to precise if its crystal structure is β or δ. For 0.84≤ x ≤0.96, the screened plasma photon energy $\hbar\omega_{ps}$ decreases with increasing x. A small increase in x from 0.96 to 0.98 leads to a change in the curve of ε_r and rapid decrease of $\hbar\omega_{ps}$. This can be explained by the change of the crystal structure from single δ to mixed δ+δ′. Further increases of x leads to the progressively change in ε_r behaviour towards that of single δ′ phase. This indicates that the δ′ phase content in the film increases, with increasing x. Due to the weak peaks observed on the XRD patterns of this film, it was difficult to determine exactly the evolution of the δ′ phase in these films, which is therefore confirmed by spectroscopic ellipsometry measurements.

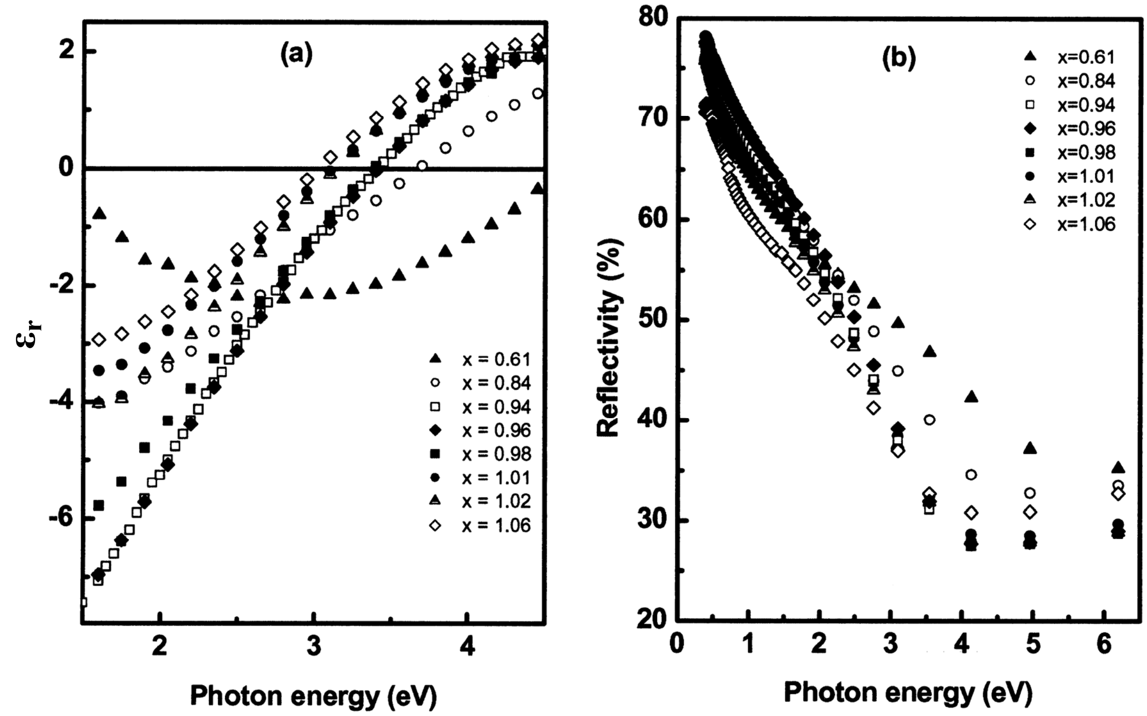

Fig. 3.23. Dielectric function (a) and reflectivity (b) spectra of NbN$_x$ films, deposited at RT and various nitrogen partial pressure P_{N2}, with different x=N/Nb.

The real part of the dielectric function (ε_r) and the reflectivity spectra of NbN$_x$ films, deposited at P_{N2} =15% and various substrate temperature T_s, are shown in figure 3.23a and b, respectively. The optical properties change continuously from that of δ phase to that of δ′ phase, with increasing T_s. This is due to the increase of the content of the δ′ phase in the film with increasing T_s (figure 3.5a).

The real part of the dielectric function (ε_r) and the reflectivity spectra of NbN$_x$ film, deposited at T_s = 400°C and various P_{N2}, are presented in figure 3.24a and b, respectively. As a function of the phase concentration, the shape of the permittivity $\varepsilon_r(\hbar\omega)$ and of the reflectivity curves progressively changes from those of the starting single phase to those of the single second phase.

The knowledge of the optical characteristics of the single NbN$_x$ phases allows estimating the degree of the mixture of NbN$_x$ phases. Therefore, spectroscopic ellipsometry *SE* measurements provide an efficient diagnostic for the optical characterization and identification of these NbN$_x$ phases

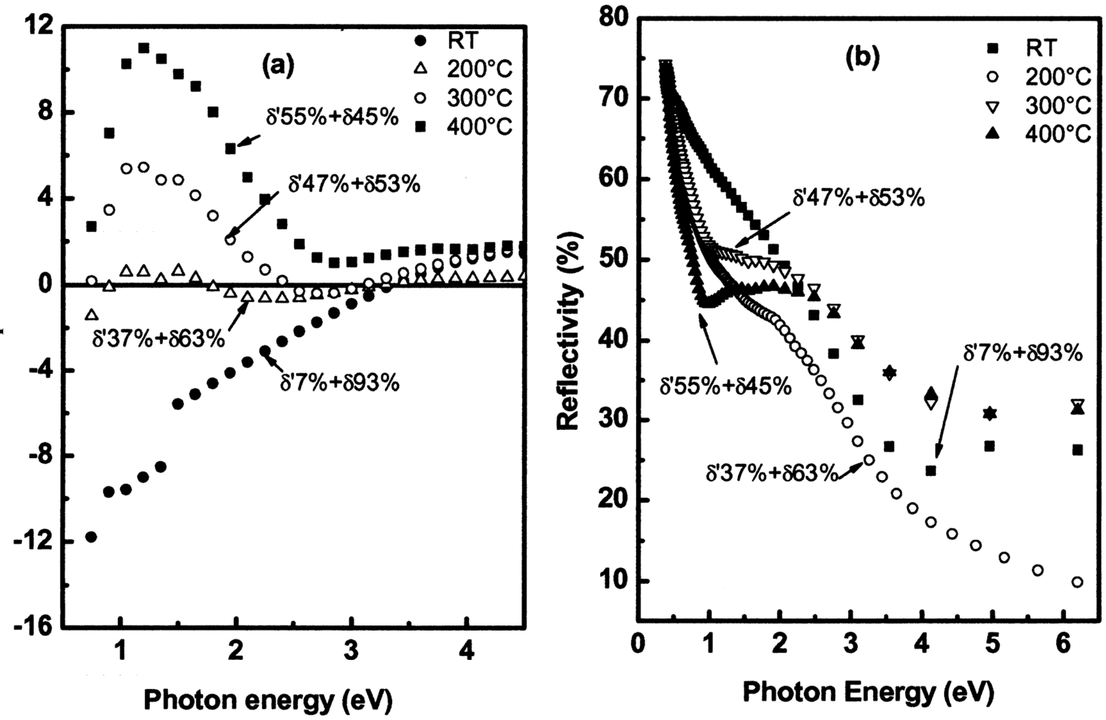

Fig. 3.24. Dielectric function ε_r (a) and reflectivity (b) spectra of NbN$_x$ films, deposited at P_{N2} =15% and various T_s, with different δ′ phase content.

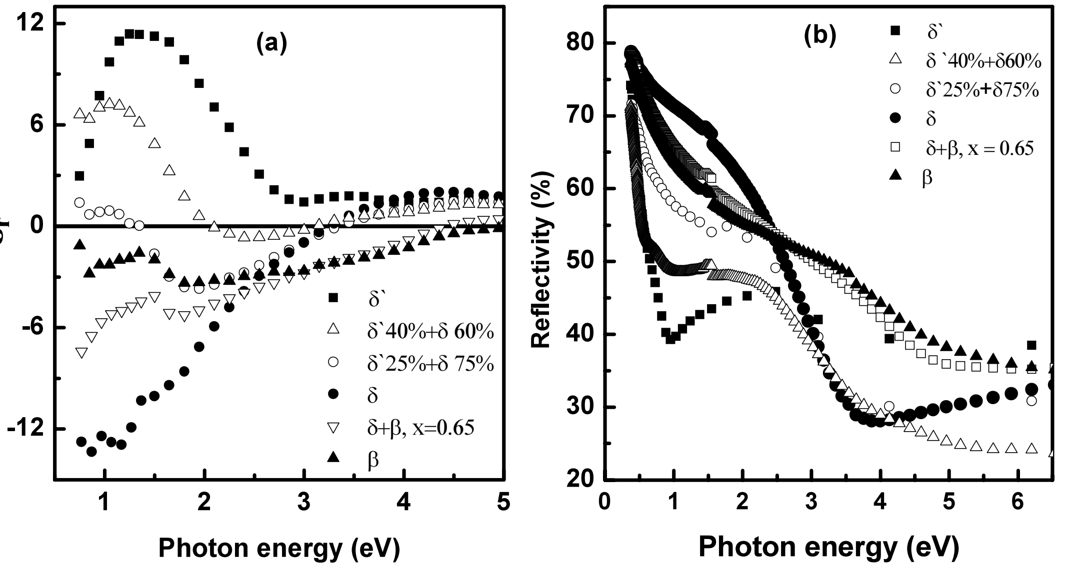

Fig. 3.25. Dielectric function ε_r (a) and reflectivity (b) spectra of NbN$_x$ films, deposited at T_s =400°C and various P_{N2}, containing different phase compositions.

3.4. Mechanical properties and stability

3.4.1. Single NbN_x phases

To investigate the mechanical properties, nanoindentation and stress measurements were done for as deposited single phase films and after their heat treatments. Treatment 1 consists in heating at 700°C in vacuum at the residual pressure $P_{res} = 1\times 10^{-3}$ Pa. Treatment 2 consists in a heating at 800°C in high vacuum at $P_{res} = 5 \times 10^{-6}$ Pa. Treatment 3 consists in heating at 1000°C in high vacuum at $P_{res} = 1\times 10^{-5}$. The oxygen concentration has been measured in as deposited film and after treatment 1. The nanohardness (H) and stress (σ) state have been measured after each treatment. Results of the different heat treatments are summarized in Table 3.4

Table 3.4 *Hardness (H), stress (σ) and oxygen concentration (O) for as deposited and after heat treatments (see text for details) NbN_x single phases: β-Nb_2N and δ´-NbN, and cubic δ-NbN; PO: Peel-off.*

Single phase films	*As deposited*			*Treatment 1*			*Treatment 2*		*Treatment 3*	
	***H* (GPa)**	***σ* (GPa)**	***O* (at.%)**	***H* (GPa)**	***σ* (GPa)**	***O* (at.%)**	***H* (GPa)**	***σ* (GPa)**	***H* (GPa)**	***σ* (GPa)**
δ´	40	-3.5	2	23	-3.5	28	37	-4	35	-1.6
β	34	0.8	2	23	-0.5	29	--	--	PO	PO
δ	24	-1	2	23	0	37	24	0.6	23	0.9

The hardness of δ´ and β phases are 40 and 34 GPa, respectively. The hardness of cubic δ-NbN_x is 24 GPa. For as deposited films, single hexagonal δ´ and β phases are harder than the cubic δ phase. Similar results were found by Sanjinés [18]. They report a high hardness for pure hexagonal V_2N and Cr_2N films compared to cubic VN and CrN films. Singer et al. have found that the β-Nb_2N phase is harder (40%) than the δ-NbN phase [19]. High compressive stress is present in the δ' thin film (-3.5 GPa) compared to the stress in the film of phases β (0.8 GPa) and δ (-1 GPa). The thermal stress for NbN_x film on Si substrate, caused by the mismatch in the thermal expansion coefficient, is about 0.6 GPa. Thus extrinsic thermal stress can originate the stress observed in the β single phase. On the contrary, the residual compressive stress in the δ´ and δ phases must be attributed to intrinsic stress.

After the heat treatment 1, every single phase shows a hardness of 23 GPa. The hexagonal phases lose their high hardness. After treatment 2, the hardness of hexagonal δ′ is still high 37 GPa. The stress in this film is practically unchanged (-4 GPa). After heat treatment 3, the hardness of the δ′ phase is still high 35 GPa whereas the stress reduces down to -1.6 GPa. For the δ phase the hardness is unchanged after Treatment 1, Treatment 2 and Treatment 3 even if its stress decreases and even becomes tensile. The hardness induced by the stress is expected to disappear after heat treatment at 400°C. Thus, the hardness of the hexagonal δ' phase is not caused by the stress. In fact, a small contribution to the hardness (~5 GPa) can be expected to be due to the compressive stress observed in this phase. The high hardness found in this δ′ phase can be attributed to the high degree of covalence observed in this phase (see 3.3.1.4). The dense microstructure also contributes to the high hardness of this phase (see 3.2) and especially to its higher oxidation resistance compared to that of the cubic δ phase. The observed difference in hardness between the two hexagonal phase β and δ′ is probably due to their different microstructures (see 3.2.1).

The applied heat treatments reveal different stability regimes of the investigated phases. The real part of the dielectric function (ε_r) of the hexagonal δ′ phase after heat treatment 3 is similar to that observed for single hexagonal δ′ without heating. In contrast, that of single δ phase after heat treatment 3 changes is similar to that of mixed δ′+δ phases. Thus the hexagonal δ′ phase after heat treatment is stable in contrast with the cubic δ which changes to mixed δ′+δ phases (figure 3.26).

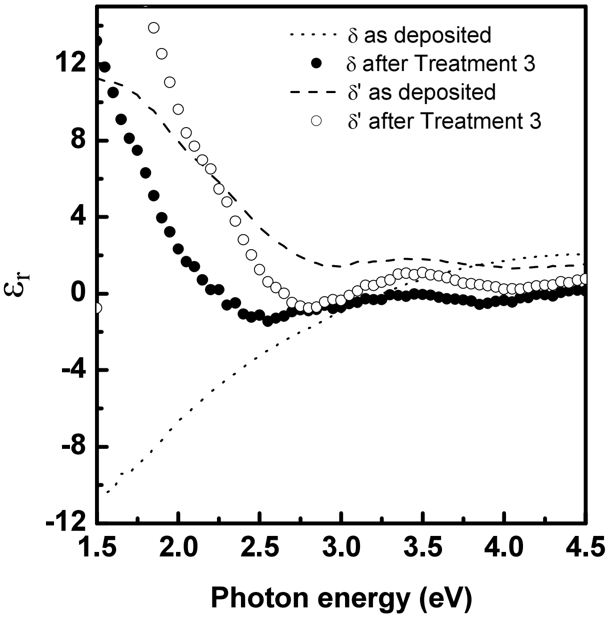

Fig. 3.26. Reel part of the dielectric function spectra of δ-NbN and δ′-NbN after heat treatment 3, compared with that of as deposited δ- NbN and δ′-NbN phases.

3.4.2. Mixed NbN$_x$ phases

The hardness of mixed phases is related to the intrinsic hardness of each constituent phase and to the morphology of the film. The intrinsic hardness of each phase is related to the cohesion, length and the covalence of bonds. The morphology of the films is controlled by the deposition parameters, e.g. nitrogen partial pressure and substrate temperature [20].

The evolution of the hardness and Young's modulus of NbN$_x$ films, deposited at *RT* and various P_{N2}, appears to be related with the type of component phases and their concentration (figure 3.27). The film with x =0.57 which crystallizes in the mixed (β+δ) phases shows high hardness ~32 GPa. In contrast, single cubic δ phase films, 0.6< x <0.97 have low hardness ~24 GPa. For mixed (δ+δ′) phase films, x >0.97, the hardness increases up to 29 GPa with increasing x. This increase is expected to be due to the increase in the hexagonal second phase content. Even if the XRD does not allow following the evolution of the hexagonal content, the behavior of the dielectric function appears to confirm that increase of the hexagonal content with increasing x.

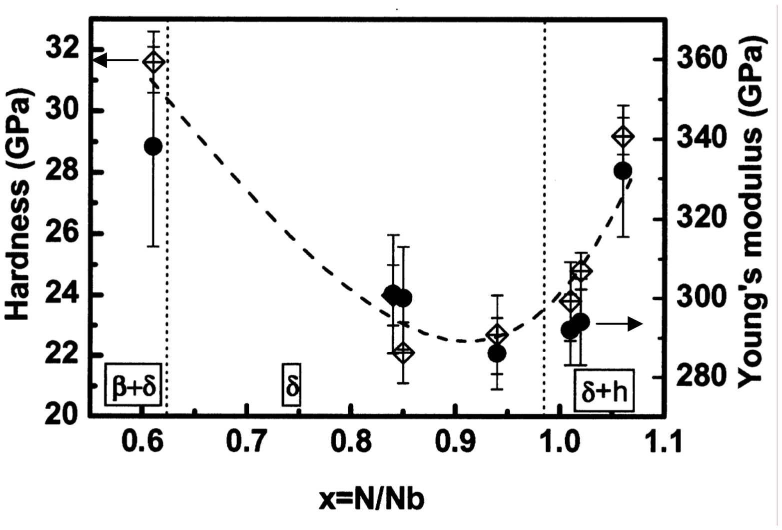

Fig. 3.27. Hardness and Young's modulus of NbN$_x$ films, deposited at RT and various P_{N2}, as a function of the ratio x=N/Nb; β: hexagonal Nb$_2$N, δ: cubic NbN and h: hexagonal δ′-NbN or ε-NbN. *The dotted line follows the values of hardness and Young's modulus as a guide for the eye*

Both, the hardness and the Young's modulus increase with increasing T_s, for film deposited at P_{N2} =15% (figure 3.28). The measured hardness differs from that calculated following the mixture law using the measured hardness for each single NbN$_x$ phase. In fact, the increase in hardness, with increasing T_s, is attributed to both, the increase of the hard δ′ phase content in the film and the film density.

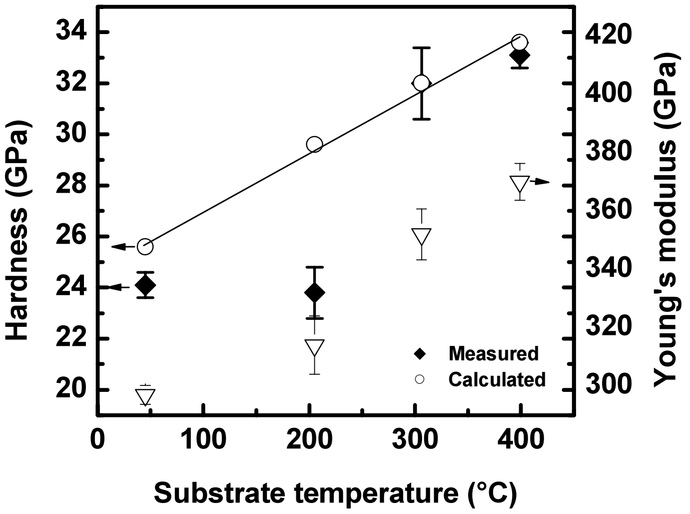

Fig. 3.28. Hardness and Young's modulus of NbN_x films, deposited at P_{N2} = 15% and various T_s. The continue line follows the values of calculated hardness, according to mixture law, as a guide for the eye.

The hardness and Young's modulus as a function of N/Nb ratio for NbN films, deposited at T_s= 400°C and various P_{N2}, are represented as a function of the δ′ phase content (δ′[%]) in the figure 3.29. No correlation between the grain size, preferential orientation, and the hardness and Young's modulus can be found. The β and β+δ (~35 GPa) films are harder than the single δ-NbN films (~25 GPa). The hardness of mixed (δ+δ′) film is low (~ 25 GPa) with δ′[%] < 50% whereas δ+δ′ films with δ′[%]>50% are very hard (~ 40 GPa). This implies that the hardness and Young's modulus values are governed by the type and the quantity of the NbN_x phases present in the films. Films with high concentration of the hard δ′-NbN phase exhibit high hardness and Young's modulus. This is due to the high intrinsic hardness of the δ′ phase and to the high density of the microstructure of the films containing high δ′ phase content.

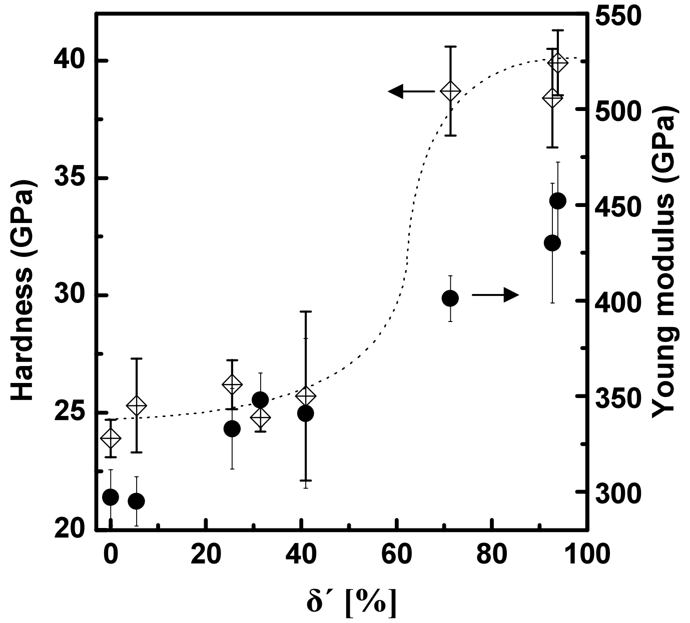

Fig. 3.29. Hardness and Young's modulus of NbN$_x$ films, deposited at T_s =400°C and various P_{N2}, as a function of the δ′ phase content. The dotted line follows the values of hardness as a guide for the eye.

3.5. Summary

Three single and mixed phases of NbN: δ, δ′ and β films were successfully deposited by varying the nitrogen partial pressure P_{N2} and the substrate temperature T_S. The properties of these films were systematically investigated. For x=N/Nb approaching the 0.5 the β phase is the more stable. With x approaching unity the δ′ is stable whereas for the others values of x the stable phase are δ. Only mixed phases of δ+ β and δ+ δ′ were deposited. The three single phases show a columnar morphology. The columnar structure in the hexagonal phases is more distinct than in the cubic. In contrast to the δ and δ′ phases, the microstructure of the β phase shows twins. The optical properties of the single phases are significantly different. Thus, spectroscopic ellipsometry measurements can be used for the determination of the phase composition in the NbN system. Reflectivity spectra of the δ′ phase exhibit a sharp edge at 1 eV which is not common in the fcc MeN phases. The covalence character is more pronounced in the hexagonal phases than in the cubic one. The high hardness of 35 and 40 GPa measured for the β and δ′ phases compared to that of the cubic, 25 GPa, can be related the high covalent character of the hexagonal phases compared to that in the cubic. The high hardness of the δ′ phase is intrinsic. This phase keeps a high hardness of 35 GPa, after heating at vacuum at 1000°C.

References of chapter 3

[1] H. Hollek, Binäre und ternäre Carbid- und Nitridsysteme der Uebergangsmetalle, Gebrüder Borntraeger, Berlin–Stuttgart, 1984.
[2] Yu.V. Levinskiy. Russ. Metall. (1974) 34.
[3] W. Lengauer, M. Bohn, B. Wollein and K. Lisak. Acta Mater. 48 (2000) 2633.
[4] G. Brauer and R. Esselborn, Z. Anorg. Allg. Chem. 309 (1961) 151.
[5] G. Reiss, J. Vancea, H. Hoffman, Phys. Rev. Lett. 56 (1986) 2100.
[6] H. Jones, O. Fischer, G. Bongi, Solid State Commun. 14 (1074) 1061.
[7] D.D. Bacon, A. T. English, S. Nakahara, F.G. Peters, H. Schreiber, W.R. Sinclair, R.B.van Dover, J.Appl.Phys. 54 (1983) 6509.
[8] A. Nigro, G. Nobile, M.G. Rubino, R. Vaglio, Phys. Rev. B 37 (1988) 3970.
[9] G-I. Oya and Y. Ouodera, J. Appl. Phys. 45 (3) (1974) 1389.
[10] Tanabe, H. Assano, Y. Katch and O. Michikami, J. Appl. Phys. 63 (5) (1988) 1733.
[11] M. W. Konevecki, K. L. Westra, B. T. Sullivan, K. E. Kornelson and M. J. Brett, Thin Solid Films 232 (1993) 228.
[12] P.E. Schmid, M.S. Sunaga, F. Lévy, J. Vac. Sci. Technol. A 16 (1998) 2870.
[13] Personn, Phy. Rev. B31 (1985) 1856.
[14] C. Stampfl, W. Mannstadt, R. Asahi, A. J. Freeman, Phys. Rev. B 63 (2001) 155106.
[15] R. Sanjinés, D. Music, M. Benkahoul, M. Papagno and F. Lévy, J. Appl. Phys. (Submitted).
[16] S. P. Denker, J. Less-Common Metals, 14 (1968) 1.
[17] L. I. Johansson, Surface Science Reports 21 (1995) 177.
[18] R. Sanjinés, P. Hones and F. Lévy, Thin Solid Films 332 (1998) 225.
[19] I.L. Singer, R.N. Bolster, S.A. Wolf and E.F. Skelton R.A. Jeffries, Thin Solid Films 107 (1983) 207.
[20] J.E. Sundgren and H.T.G. Hentzell, J. Vac. Sci. Technol. A4 (5) Sep/Oct (1986) 2259.

Chapter 4

Ternary silicon niobium nitride Nb-Si-N thin films

In this chapter, the Chemical composition, crystal structure, morphology, electronic properties and mechanical properties of Nb-Si-N thin films are reported as a function of the Si content. Three distinct composition domains are specified. A model of the microstructure evolution is proposed, as a function of Si content. This model permits to explain the evolution of the properties of the Nb-Si-N films due to Si addition.

4.1. Chemical composition

Nb-Si-N thin films have been deposited by reactive magnetron sputtering from two confocal Nb and Si targets.

In order to obtain various Si contents in the films, the current applied on the Si target (I_{Si}) was varied. The Nb content decreases with increasing I_{Si}, while that of Si increases (figure 4.1). The concentration of oxygen and carbon in the films was measured by electron probe microanalysis (EPMA) and found less than 2 and 3 at.%, respectively. It can be noticed, that for film without Si the concentration of Nb (at.%) is larger than that of N (at.%) whereas for Nb-Si-N film N (at.%)>Nb (at.%).

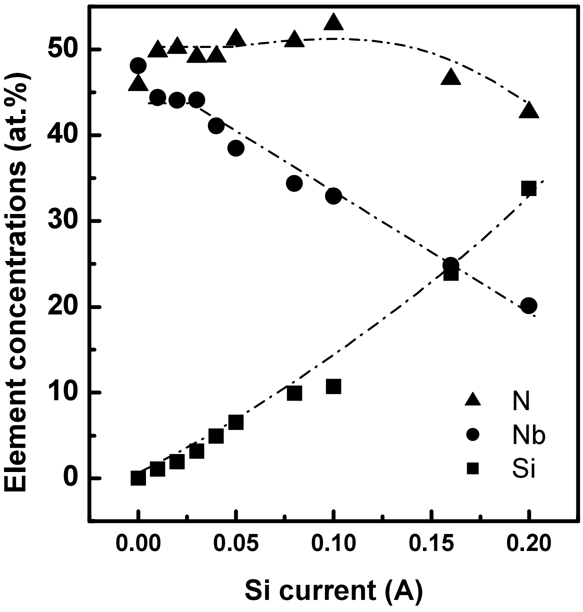

Fig. 4.1. Chemical composition of Nb-Si-N films as a function of the applied current on the Si target.

4.1. Crystalline structure and morphology

XRD patterns, measured at grazing incidence (γ= 4°), of Nb-Si-N films are illustrated in figure 4.2. The crystal structure of the film deposited without Si is mixed of δ+δ' phases. The addition of Si, even in small quantity (~1at.%), leads to the deposition of the single cubic δ phase, only. Neither silicide phases nor crystalline Si_3N_4 peaks are detected in the X-ray diffraction diagrams. For C_{Si} below ~11 at.%, the Nb-Si-N films are well crystallized. At higher C_{Si}, the films become amorphous.

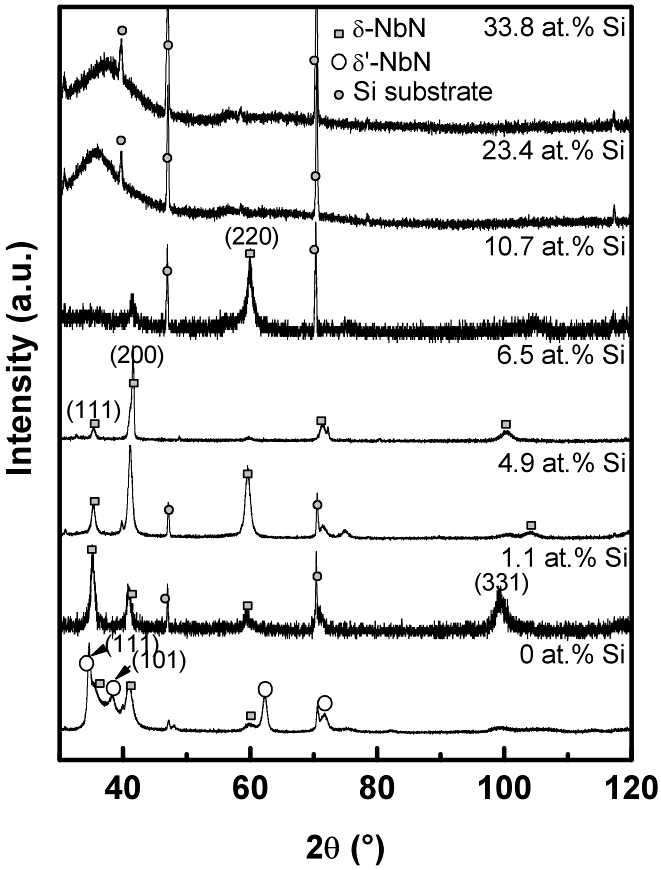

Fig. 4.2. X-ray diffraction patterns at grazing incidence (γ=4°) of Nb-Si-N films with different Si contents (Cu K_α).

The texture parameter (I_{111}/I_{200}) and the crystallite size (perpendicular to plane of the film) are calculated from the XRD patterns, recorded in the Bragg-Brentano configuration (figure 4.3). They are represented in figure 4.4.a and b, respectively. All the films are strongly textured in the [200] direction, except the films with C_{Si} = 3.2 at.% which are [111] textured and with C_{Si} = 4.9 at.% that are not textured. The pure NbN film shows a grain size of about 5 nm. Adding a small quantity of Si (~1 at.%) leads to the increase in the grain size up to 12 nm. This increase can be attributed to the change in the crystal structure from mixed δ+δ' to single δ phase. The grain size does not significantly changes for 1≤ C_{Si} ≤4.9. At C_{Si} = 6.5 at.% the grain size is larger, about 18 nm. Above 6.5 at.% Si, the crystallite size decreases as the Si content increases.

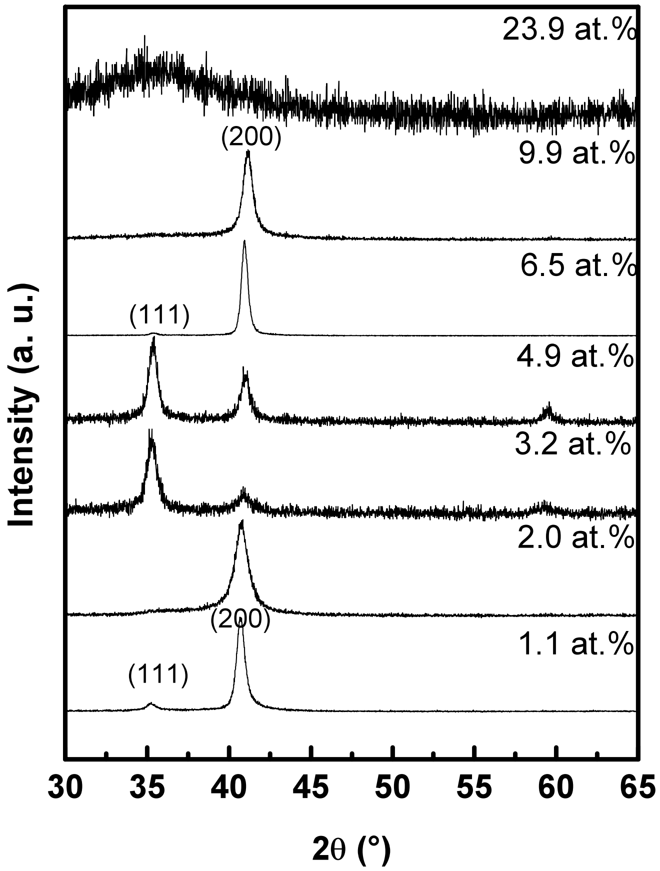

Fig. 4.3. X-ray diffraction patterns at Bragg-Brentano of Nb-Si-N films with different Si contents (Cu $K_α$).

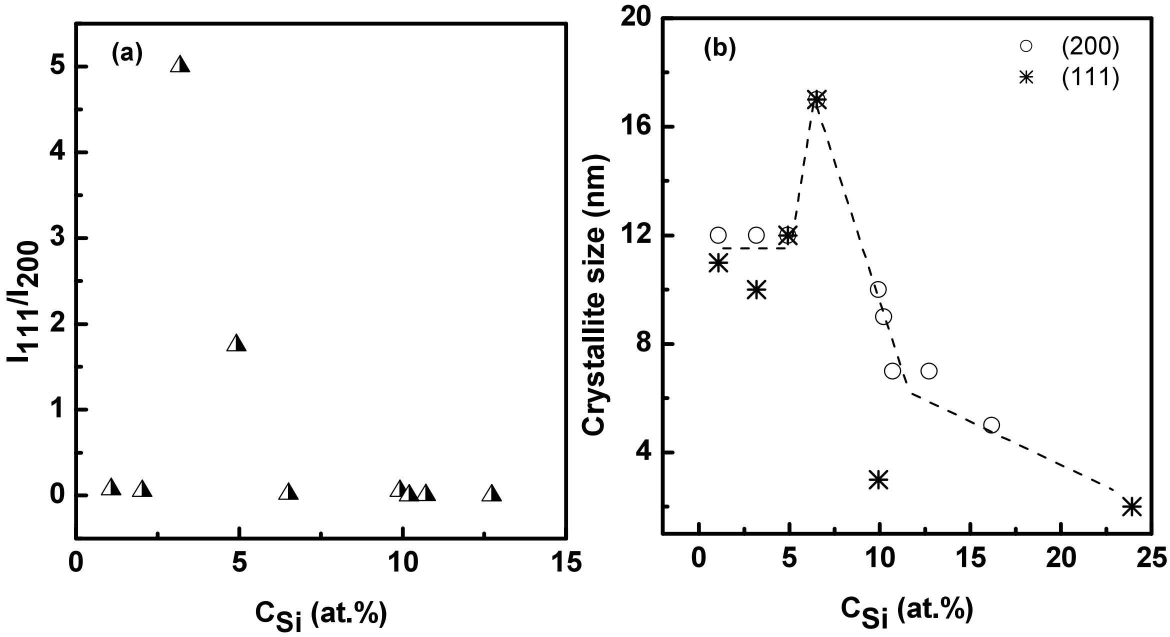

Fig. 4.4. Preferential orientation I_{111}/I_{200} (a) and grain size (b) of Nb-Si-N films vs. Si content. Dashed line follows the values of grain size as a guide for the eye.

TEM and *HRTEM* images of the cross sectional view of the Nb-Si-N films, with various Si content, are illustrated in figures 4.5 and 4.6, respectively.

The film with low Si content, C_{Si} =4.9 at.%, has a columnar structure (figure 4.5a). Each column is formed by crystallites agglomerates. For higher Si content, C_{Si} ≥12 at.%, the global texture is still present in the film, but inside the same column the crystallites have different orientations. Consequently, the diffraction contrast increases inside the column and practically disappears between the columns (figure 4.5b). The columnar morphology disappears for Si content higher than 24 at. % and the films are quasi-amorphous (figure 4.5d).

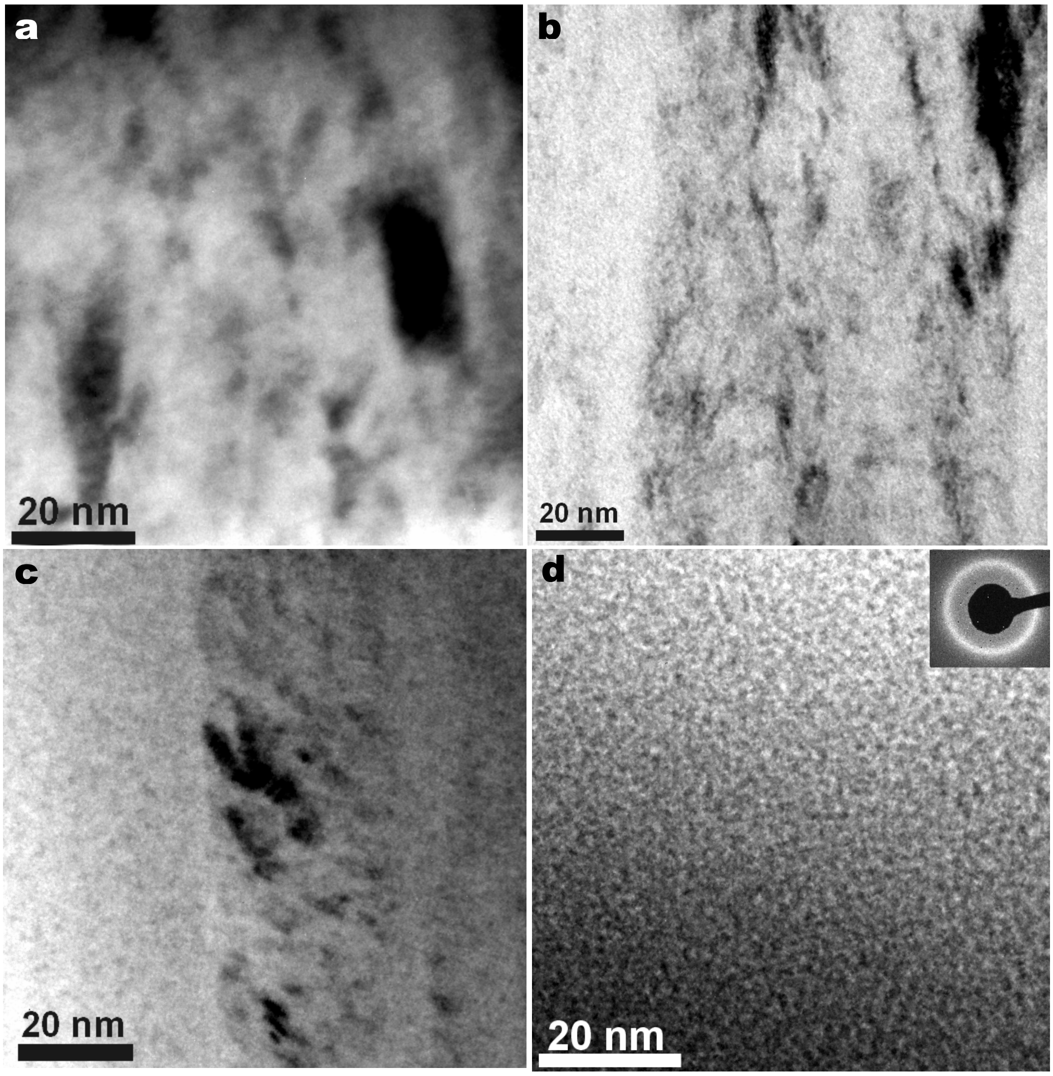

Fig. 4.5. TEM images of Nb-Si-N films with various Si content: a) 4.9 at.% b) 12.7 at.%, c) 20 at.%, d) 24 at.%.

The film at 20 at.% Si (figure 4.5c) shows a mixture of well crystallized columns dispersed in a quasi-amorphous matrix. Inside the columns, the mean value of the crystallite size is 6 nm. In contrast, the grain size is 2-3 nm in the quasi-amorphous matrix (figure 4.6a,b). X-ray energy dispersive spectrometry (XEDS) investigations reveal 23 at. % Si inside the crystalline columns and 18 at.% Si in the quasi-amorphous matrix (figure 4.7). These films present an intermediate morphology between homogeneously well crystallized films and quasi-amorphous films.

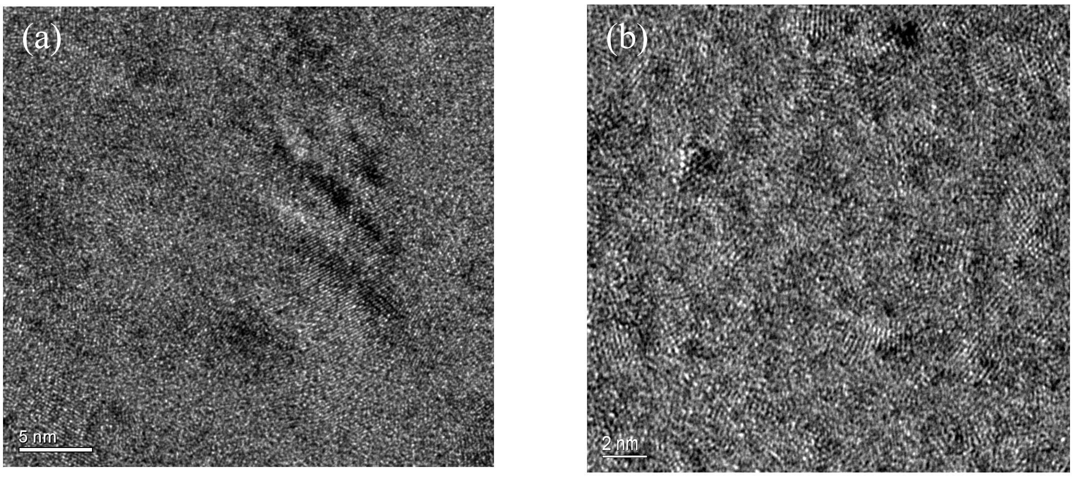

Fig. 4.6. HRTEM images of Nb-Si-N films: (a) 20 at.% inside and (b) 20 at.% outside the column.

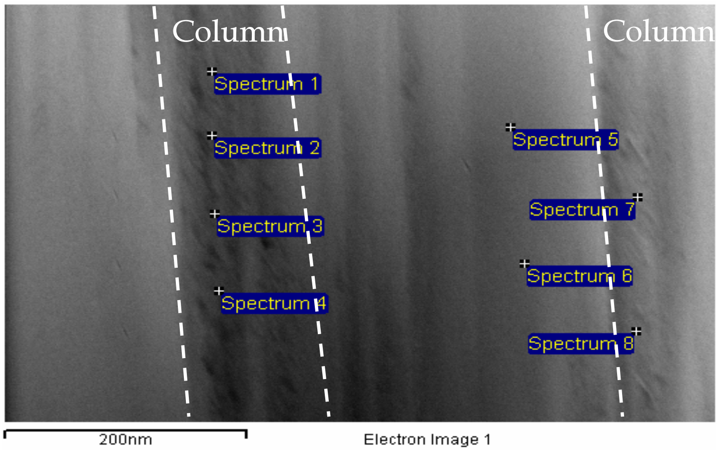

Spectrum	Si/Nb
Spectrum 1	0.37
Spectrum 2	0.38
Spectrum 3	0.39
Spectrum 4	0.41
Spectrum 5	0.54
Spectrum 6	0.54
Spectrum 7	0.41
Spectrum 8	0.41
Mean value	
Inside column	0.40
Outside column	0.54

Fig. 4.7. STEM image with marked points for the chemical composition, measured by XEDS, of Nb-Si-N films with Si content 20 at.%. The dashed line delimits the columns.

4.3. Electronic properties

4.3.1. FTIR and XPS

In order to understand how the silicon atoms are incorporated in the Nb-Si-N films, FTIR absorption spectra were measured (figure 4.8). The film with C_{Si} $\approx$1 at.%, does not present an absorption band, in the range 700–1100 cm^{-1}, whereas that with ~5 at.% shows a broad weak peak. Further increase of Si content leads to the increase in the intensity of this absorption peak. Many investigations report Si–N vibrational modes located at 800, 840, and 970 cm^{-1}. The main mode at 840 cm^{-1} was attributed to asymmetric stretching vibrations of NSi_3 groups, the mode at 800 cm^{-1} was attributed to the Si-N bond vibration in the SiN_x configuration and the high frequency mode at 970 cm^{-1} was correlated with the NSi_3 groups as planar configurations [1,2].

XPS measurements of the Si 2p peak, done by Tabet [3], provide further information on the Si bonding in the films (figure 4.9). The film with C_{Si} $\approx$1 at.% presents a peak at a binding energy (BE) of ~99.4 eV. A peak at BE~101.2 eV appears with increasing C_{Si}. This peak is particularly well observed for C_{Si} $\geq$6.5 at.%. The low energy peak at 99.4 eV can be assigned to Si in either free Si or Nb silicide. The second peak appearing at high BE with increasing C_{Si}, reflects that the silicon becomes more nitrided with probably Si_3N_4 formula. The high energy peak (101.2 eV) corresponds to the Si valence state associated with the replacement of the four possible Si–Si bonds by Si–N bonds [4]. A similar behavior was observed in sputtered Ti-Si-N films [5].

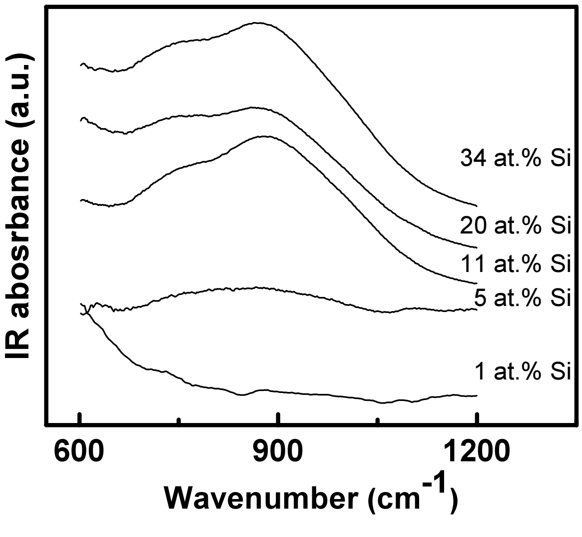

Fig . 4.8. FTIR spectra of Nb-Si-N films with various Si contents.

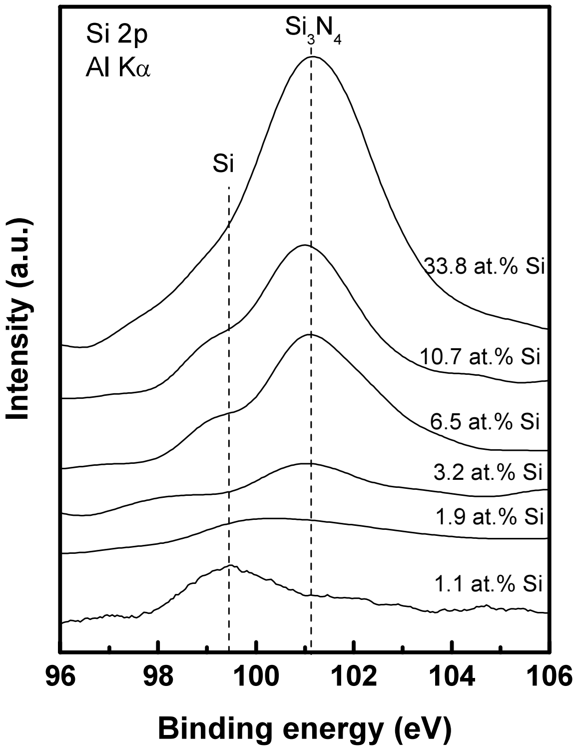

Fig. 4.9. XPS spectra of Si 2p in Nb-Si-N films with various Si contents [3].

4.3.2. Electrical resistivity

The variation of the electrical resistivity ρ_{RT} at room temperature, as a function of the Si content, is illustrated in figure 4.10a. For C_{Si} ≤3.2 at.%, the resistivity ρ_{RT} remains constant (135 μΩcm) with increasing C_{Si}. This ρ_{RT} value is lower than that found for pure cubic NbN phase films, which is ~250 μΩcm (see 3.3.1.1). The decrease of the ρ_{RT} after addition of ~1at.% can be attributed to the induced increase of the grain size (see 4.1). At C_{Si}= 4.9 at.%, the ρ_{RT} becomes 180 μΩcm whereas at C_{Si}= 6.5 at.% it increases to 330 μΩcm. Further increase in Si content leads to a high increase in ρ_{RT} up to 2700 μΩcm. It is clear that for a certain Si content in the range 3.2-5 at.% something changes in the structure of the Nb-Si-N films which induces an increase in the ρ_{RT}. Since the grain size does not change with increasing the Si content from 3.2 to 4.9 at.% the observed increase in ρ_{RT} is expected caused by the change in the nature of the grain boundaries.

The variation of the d.c. electrical resistivity as a function of the temperature is shown in figure 10b. The resistivity $\rho(T)$ curve of every film exhibits a negative temperature coefficient of resistivity TCR $(=\frac{1}{\rho}\frac{\partial \rho}{\partial T})$. A negative TCR is frequently observed in sputtered NbN thin polycrystalline films. It is often explained in terms of grain boundary scattering effects [6]. A second probable mechanism which was reported is the electron localization in weakly disordered metallic materials (weak localization model) [7].

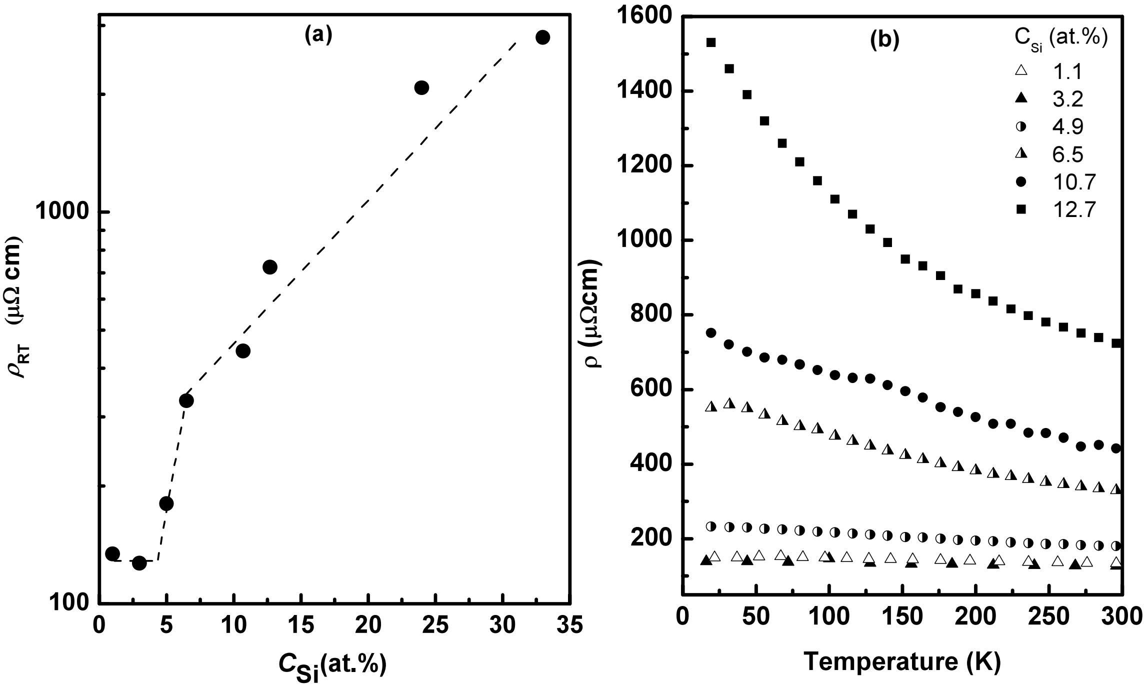

Fig. 4.10. Resistivity at room temperature and as a function of temperature of Nb-Si-N films, vs. Si content, (a) and (b), respectively.

4.3.3. Optical properties

The reflectivity of Nb-Si-N films for C_{Si} ≤10.7 is presented in figure 4.11. At these Si contents the Nb-Si-N films, with thickness higher than 1μm, are opaque and no reflection from the interface film/substrate can occur.

The reflectivity of Nb-Si-N films in the infra-red (IR) and visible range does not significantly change for C_{Si} ≤3.2%), with increasing Si content. Further Si content increase leads to a rapid decrease in the reflectivity in the IR and visible range. The films change their behavior from metallic to dielectric with increasing the Si content.

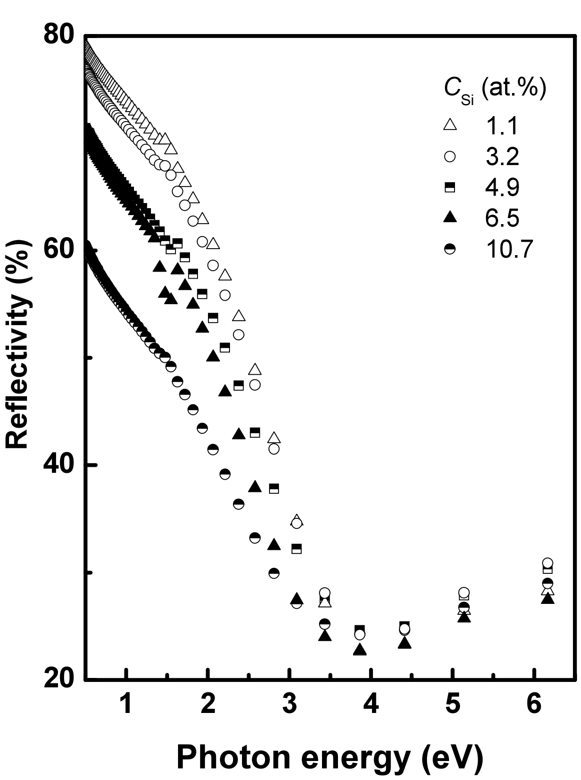

Fig. 4. 11. Reflectivity spectra of Nb-Si-N films with various Si contents.

The real (ε_r) and imaginary (ε_i) parts of the dielectric function of Nb-Si-N films with various Si content are shown in figures 4.12a,b. The refractive index (*n*) and the extinction coefficient (*k*) are reported in figure 4.13a,b. A simple semi-infinite model was used to calculate ε_r, ε_i, *n*, and *k* for Nb-Si-N films with C_{Si} ≤10.7. In this range of Si contents the films are considered as opaque with a thickness higher than 1μm. With increasing the Si content in the films, the behavior of ε_r and ε_i changes from a metallic to a dielectric character. The screened plasma energy ($\hbar\omega_{ps}$) is shown, as a function of the Si content, in figure 4.14. Two different regimes are observed for the variation of the $\hbar\omega_{ps}$ as a function of the Si content. The screened plasma energy $\hbar\omega_{ps}$ for Nb-Si-N films with C_{Si} ≤3.2 at.% slowly decreases with increasing Si content. Further Si content increase induces a rapid decrease of $\hbar\omega_{ps}$.

Values of the refractive index (*n*) and of the extinction coefficient (*k*), at photon energy equal to 2.24 eV corresponding to wavelength of 500 nm are reported in figure 4.14, as a function of Si content. The *n* increases from 1.5 to 2.2 whereas the *k* decreases from 2.9 to 2.1, with increasing C_{Si} from 1.1 at.% to 10.7 at.%.

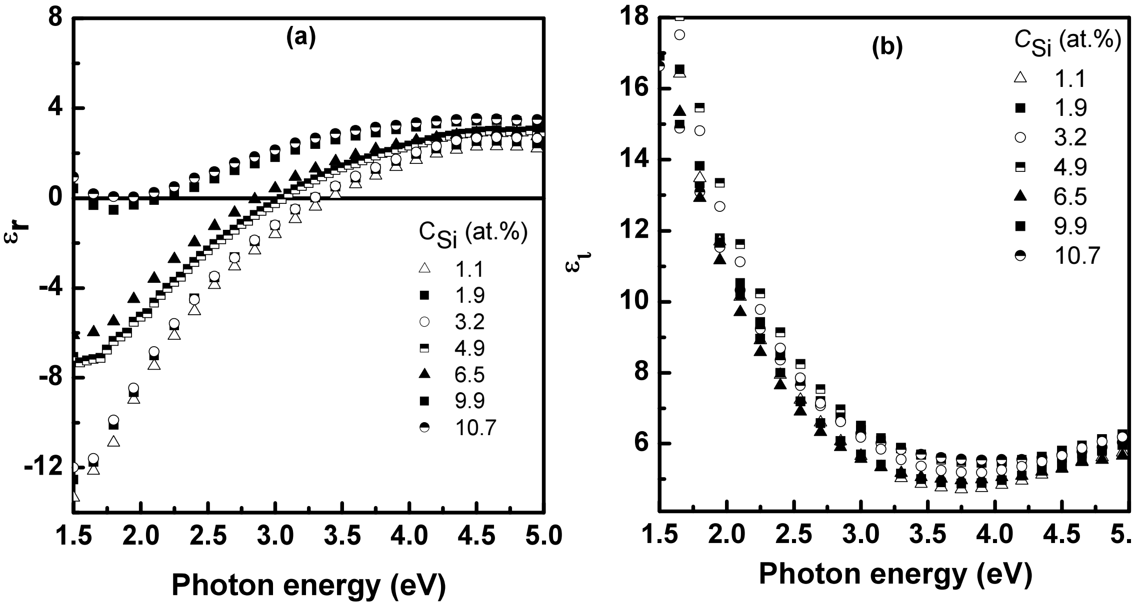

Fig. 4.12. Dielectric function of Nb-Si-N films with various Si contents: (a) reel part (b) imaginary part.

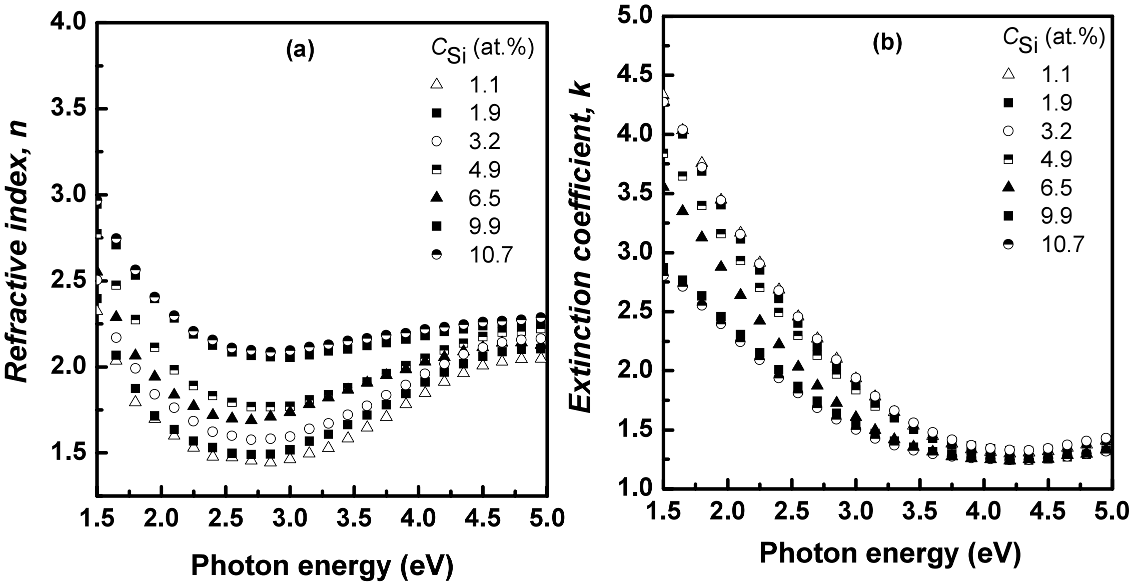

Fig. 4.13. Refractive index (n) and extinction coefficient (k) spectra of Nb-Si-N films with various Si contents.

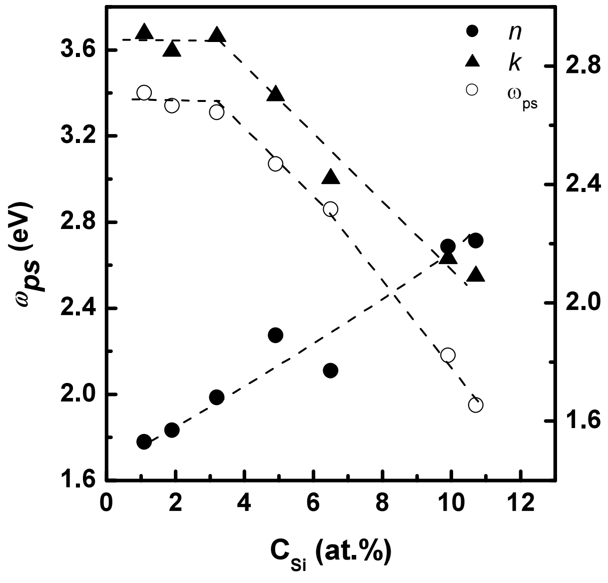

Fig. 4.14. Values of Refractive index (n) and extinction coefficient (k) at wavelength of 500 nm and screened plasma energy (ω_{ps}), vs. Si content in Nb-Si-N films.

4.4. Mechanical properties

Figure 4.15 shows the hardness as a function of the Si content and reports the residual stress values of the Nb-Si-N films. The measured hardness for the film deposited without Si (pure NbN) is 35 GPa. This hardness value is relatively high because of the presence of the hard hexagonal δ′ phase (40 GPa) in the film (see 3.4). Since every Nb-Si-N film, deposited with Si addition, crystallizes in a single cubic δ structure its hardness has to be compared to that of the typical cubic δ phase (25 GPa). The nanohardness increases from 25 GPa to 34 GPa with increasing Si content, from 0 to about 4.9 at.%. The films with C_{Si} in the range 4.9–11 at.% present the highest nanohardness (~34 GPa). For larger C_{Si}, the nanohardness decreases and gradually tends towards the reported value for the amorphous Si_3N_4 phase (22 GPa) A similar trend has been observed in sputter deposited Ti-Si-N thin films [5]. The hardness behavior of sputter deposited Nb-Si-N films is also comparable to that observed in nanocomposite Me-Si-N (Me=Ti, V, W) deposited by plasma CVD [8,9] or PVD [10-12].

All the Nb-Si-N films are in a state of compressive stress. The thermal stress induced by the difference in the thermal expansion between the NbN film and the Si substrate is tensile and is about 0.4 GPa. On the assumption that a low amount of Si addition does not significantly influence the thermal expansion of the film, this thermal stress cannot explain the compressive stress values in the Nb-Si-N films.

For C_{Si} ≤3.2 at.%, no significant change in the stress of films is observed. For 3.2≤ C_{Si} ≤6.5 at.% the stress increases with increasing Si content. Further increase of the Si content leads to a decrease in the residual stress. The change in the stress, at certain Si content indicates probably the presence of microstructural modifications in the film.

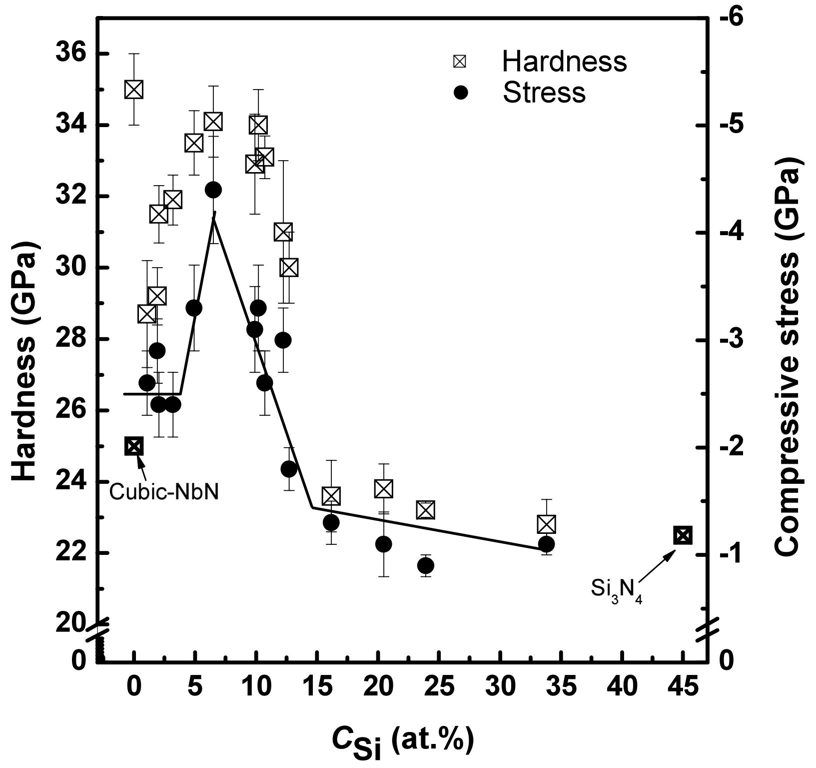

Fig. 4.15. Nb-Si-N films: Nanohardness and compressive stress vs. Si content. Continue line follows the values of stress as a guide for eye. Cubic-NbN: typical hardness of the cubic NbN films measured in this study (see 3.4), Si_3N_4: hardness of Si_3N_4 from [4].

4.5 Model of the morphology evolution as a function of Si content

Regarding the evolution of the properties of Nb-Si-N films, with increasing Si content, it appears that for certain Si concentration between 3.2 and 5 at.% the properties of these films significantly change. A model for the Nb-Si-N film, formation as a function of Si content is proposed. The experimental results which sustain this model are presented below.

In this model, three distinct domains of concentration are specified (figure 4.16). In Domain 1 (1≤ C_{Si} ≤4 at.%) the Si atoms substitute Nb in the NbN lattice and the NbN:Si phase is formed. In Domain 2 (4≤ C_{Si} ≤7 at.%), where the solubility limit is exceeded, a fraction of Si atoms segregate at the grain boundaries. A nanocomposite film containing NbN:Si grains partially covered by SiN_x layer is formed. The value of 4 at.% is chosen as a limit of the solubility at the middle of the Si content range from 3.2 to 4.9 at.%. The upper limit, 7 at.%, for the domain 2 corresponds to the Si content for which the coverage of the NbN:Si grain by SiN_x layer is 100% (see annex 1). For further increase in Si content (Domain 3), the NbN:Si crystallites, surrounded by a monolayer of SiN_x, reduce their size. So, the increasing amount of the SiN_x amorphous phase in the films is obtained by increasing the surface to volume ratio of the NbN:Si crystallites. Figure 4.16 illustrates this model of morphology evolution.

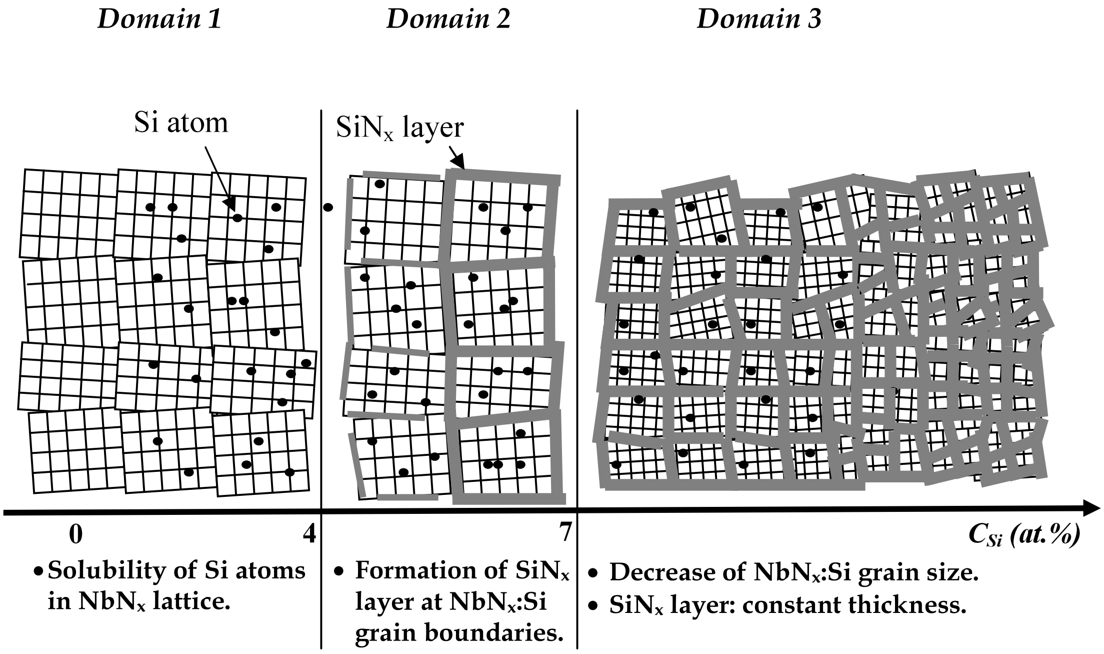

Fig. 4.16. The film formation model for the Nb-Si-N ternary system.

The following results have allowed establishing this model.

In order to study the solubility domain of Si in NbN, the relaxed lattice constant a_0 for various Si content is reported in figure 4.17. The a_0 value is deduced by calculating and subtracting the residual stress contribution to the lattice deformation. The lattice constant (a) was calculated from the position of the (200) peak in the XRD patterns, measured in the Bragg-Brentano configuration. Considering that the films are free of stress perpendicular to the plane of the film ($\sigma_z = 0$), and that the stress of the film parallel to plane is isotropic ($\sigma_x = \sigma_y = \sigma$), then the relaxed lattice constant a_0 can be calculated with help of the relation

$$\frac{a-a_0}{a_0}=-\frac{2\nu\sigma}{E}$$

where σ, ν and E are the compressive residual stress, the Poisson coefficient (0.3) and Young's modulus measured on Nb-Si-N films by nanoindentation, respectively.

Even in small quantities (1 at.%), the Si addition induces a significant increase of the lattice parameter a_0 by about 0.7 %. This lattice variation is attributed to the important increase of the nitrogen content in the film (figure 4.18). The increase of the N content in the Nb-Si-N films, compared to NbN, can be attributed to the influence of the second plasma (from the Si target) on the kinetic of the film growth, by increasing the ionization of the N atoms. The introduction of N into interstitial positions and the diminution of possible Nb and N vacancies in the NbN lattice are responsible for the observed lattice expansion. In the fcc NbN, the intrinsic vacancy concentration can reach 13% [13]. Further increase of the Si content in the films (Domain 1 and 2 in figure 4.17) leads to a decrease of the lattice parameter. In Domain 1 ($1\leq C_{Si}\leq 4$ at.%) the decrease of a_0 can be explained by a lower global nitridation (i.e. having less nitrogen in interstitial sites) and by a replacement of Nb by Si in the fcc NbN lattice. Similar results of the lattice parameter contractions were already observed for Cr-Si-N films [14].

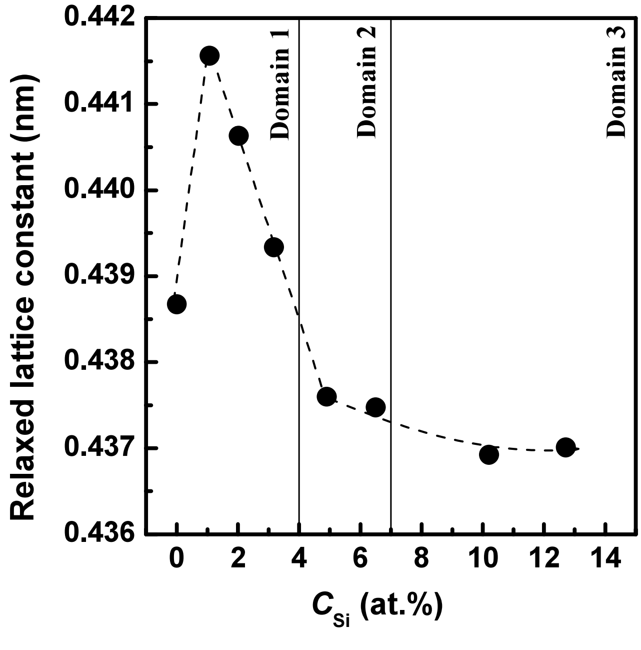

Fig. 4.17. Relaxed lattice parameter of Nb-Si-N films vs. Si content.

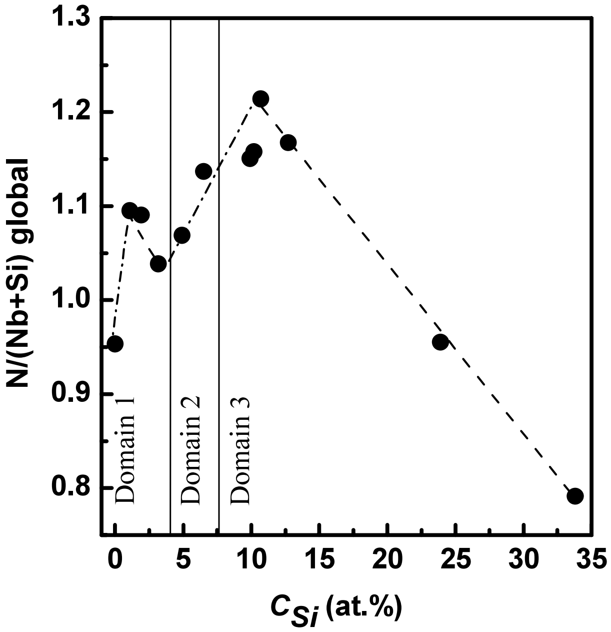

Fig. 4.18. N/(Nb+Si) ratio of Nb-Si-N films vs. Si content.

In Domain 2, the lattice parameter decreases with increasing Si content, but at a lower rate. This can be explained by the diminution of the nitrogen content inside the crystallites. The formation of the SiN_x ($x \geq 1.5$) phase surrounding the NbN:Si crystallites (with ~4 at.% Si inside) can explain the increase of the global N/(Nb+Si) ratio (figure 4.18). The results of the XPS measurements point at this sense (see 4.3.1). Further increase of Si content ($C_{Si} \geq 7$ at.%) does not significantly change the lattice parameter value (Domain 3). The decrease of N content for higher Si content (Domain 3 figure 4.18) is a consequence of the increasing Nb + Si atomic fluxes whilst maintaining the same N_2 partial pressure.

According to XEDS, certain regions which probably consist of SiN_x appear in Nb-Si-N films rich in Si. The use of XRD, FTIR, XPS, TEM and HRTEM do not allow distinguishing whether this SiN_x form a separate phase or coat the NbN crystallites. No direct method can answer this question; the study of the variation of the grain size (D) *vs.* Si content provides hints. The reduction rate of crystallite size with Si addition ($-\Delta D/\Delta C_{Si}$) is negative or 0 at low Si content (Domain 1 and 2). The decrease of the mean crystallite size in the films due to Si incorporation is observed only in Domain 3 ($C_{Si} \geq 7$ at.%). In this domain, the size of the crystallites in the Nb-Si-N films decreases according to the relationship C_{Si} α $(1/D)$, as shown in figure 4.19. A similar behaviour was found for Ti-Si-N [11] and Ti-Ge-N films [15]. During the film growth, the Si atoms segregate at the grain surface, and hinder the growth of the NbN:Si crystallites. The dependence C_{Si} α $(1/D)$ confirms the increase of the amount of the SiN_x phase in the films on the NbN:Si nanocrystallite surfaces by increasing their surface/volume ratio and maintaining a constant thickness of the SiN_x layer.

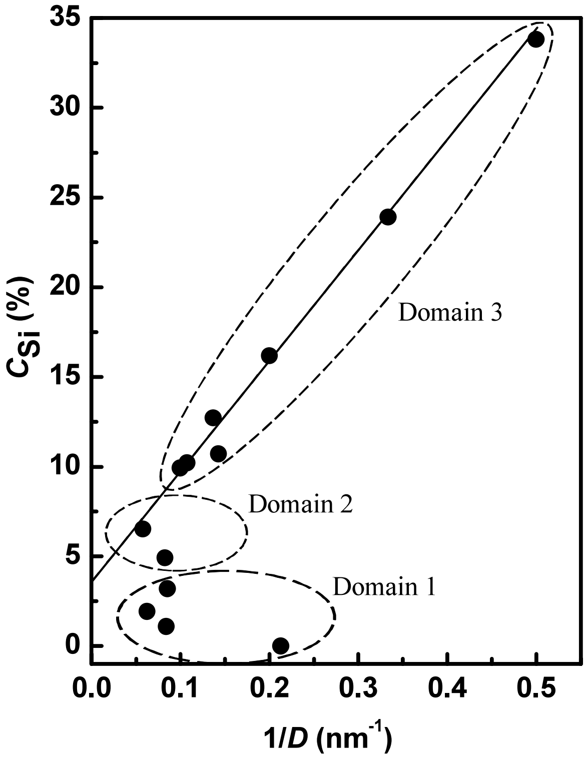

Fig. 4.19. Si content of Nb-Si-N films vs. the inverse of grain size (1/D).

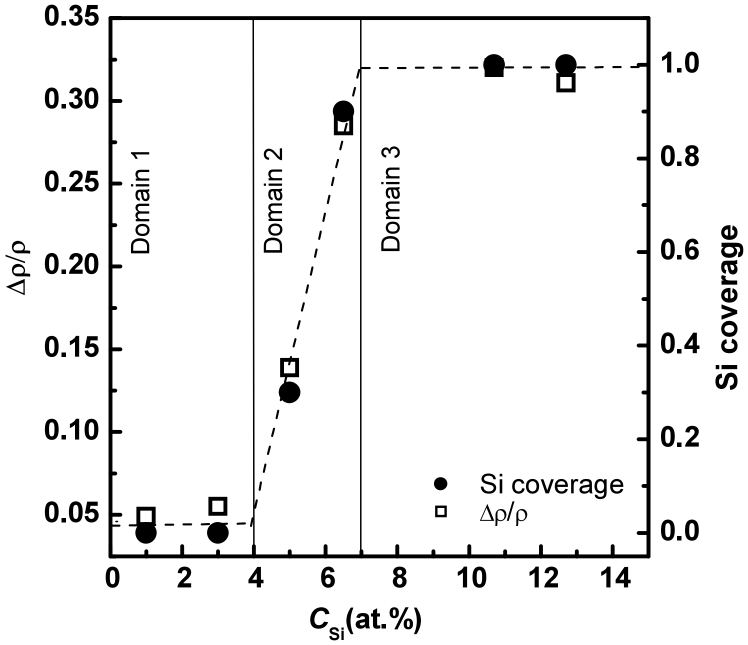

Fig. 4.20. The relative variation of resistivity ($\Delta\rho/\rho$) and the Si coverage ratio vs. Si content of Nb-Si-N films.

Complementary studies of the electrical resistivity of Nb-Si-N films as a function of the temperature bring into evidence the presence of the SiN_x layer at the grain boundaries.

From the evolution of the resistivity as a function of the temperature (figure 4.10b), in the range (150K-RT), the relative variation of the resistivity with temperature $\Delta\rho/\rho$ $((\rho_{150K} - \rho_{RT}) / \rho_{RT})$ is reported *vs.* Si content in figure 4.20. In the chosen range of temperature (150 K-RT) the resistivity varies linearly with the temperature.

In the Si content dependence of $\Delta\rho/\rho$, three distinct domains are observed, which correspond to the 3 domains pointed out through the observation of the structural and morphological film evolution. A good correlation between the Si coverage and the $\Delta\rho/\rho$ can be noted. Calculation details of the Si coverage are reported in annex 1.

In Domain 1 (Si atoms soluble in the NbN lattice) $\Delta\rho/\rho$ ~0.05 and is constant. A drastic increase of $\Delta\rho/\rho$ to ~ 0.3 is observed in Domain 2. This corresponds to the formation of the SiN_x layer at the grain boundaries. In Domain 3, $\Delta\rho/\rho$ is constant at 0.3 and corresponds to a constant thickness of the SiN_x layer. In fact, the $\Delta\rho/\rho$ parameter is related to the temperature coefficient of resistivity (TCR) which reflects the evolution of a supposed grain boundary barrier.

Quantitatively, the behaviors of the variation of the resistivity relative and the Si coverage ratio, as a function of Si content, are similar. The TCR behavior is dominated by the formation of SiN_x insulating layer at the grain boundaries. TCR measurements can provide a good method for the detection of the solubility limit of Si in NbN.

4.6. Understanding of the hardening and stress state in Nb-Si-N films with help of the proposed model

In Domain 1 (C_{Si} ≤4 at.%), the hardening observed with increasing C_{Si} is due to the fact that Si atoms are soluble in the NbN lattice in this domain. Thus, a solid solution hardening mechanism can explain the hardness increase. Even though changes in the film morphology were not seen, they cannot be excluded and they can also influence the film hardening in this concentration range. The stress state is related to the morphology of the film. Since Si atoms are soluble in NbN crystallites, the film morphology does not change and the stress remains constant with increasing C_{Si}.

In Domain 2 (4≤ C_{Si} ≤7 at.%), the NbN:Si grains cannot accept the whole quantity of added Si atoms. This induces a diffusion of a certain amount of Si to the grain boundaries. Thus a layer of SiN_x surrounding the NbN:Si crystallite is formed. If the hardness remains constant the stress increases in this Si concentration range. The formation of the SiN_x layer surrounding the NbN:Si grains during the film growth alters the stress state.

Further increase of the Si content (Domain 3, C_{Si} ≥7 at.%) leads to a reduction of the crystallite size without changing the thickness of the SiN_x layer at the crystallite surface. This induces a gradual nanohardness decrease towards the reported value for the amorphous Si_3N_4 phase (22 GPa). In fact, above C_{Si} ~13 at.% the volume fraction of the SiN_x phase becomes significant and, with increasing Si content, thus the films become softer [15]. As a consequence of the crystallite size reduction, the compressive stress decreases in Domain 3.

As a conclusion, the stress is not responsible on the hardening in the Nb-Si-N films. The stress evolution as a function of the Si content, gives reliable information on the microstructure evolution.

4.7. Summary

A model for the film formation of Nb-Si-N thin films deposited by DC magnetron sputtering is proposed. Observing the evolution of the structural, morphological and mechanical properties with increasing Si content, 3 distinct concentration domains are pointed out. In Domain 1 (1≤ C_{Si} ≤ 4 at.%) the Si atoms substitute Nb in the NbN lattice and polycrystalline film of NbN:Si grains is deposited. In Domain 2 (4≤ C_{Si} ≤7 at.%) a fraction of Si atoms segregates at the grain boundaries. A SiN_x layer is formed on the NbN:Si crystallite surfaces. The covering ratios increase with Si content up to 100% (formation of a monolayer). Further increase in Si content (Domain 3), the NbN:Si crystallites, surrounded by a monolayer of SiN_x, reduce their size. So, the increasing amount of the SiN_x phase in the films is realized by increasing the surface to volume ratio of the NbN:Si nanocrystallites.

The formation of the SiN_x layer can explain the change observer in the electrical and optical properties of Nb-Si-N films with increasing the Si content.

The resistivity measured as a function of temperature is proposed to provide an experimental mean for determining the limit of Si solubility in Nb-Si-N system and for following the thickness evolution of the SiN_x coverage layer in the composite films.

The hardness behavior is explained through the structural and morphological mechanisms involved at the nanoscale level: solid solution hardening explains the hardening observed in the Nb-Si-N films.

References of chapter 4

[1] Y.C. Liu, K. Furukawa, D.W. Gao, H. Nakashima, K. Uchino and K. Muraoka, Appl. Surf. Sci. 121–122 (1997) 233.

[2] E. Martinez, R. Sanjinés, A. Karimi, J. Esteve and F. Lévy, Surf. Coat. Technol. 180–181 (2004) 570.

[3] M. Benkahoul, C.S. Sandu, N. Tabet, M. Parlinska-Wojtan, A. Karimi and F. Lévy, Surf. Coat. Technol. 188-189 (2004) 435.

[4] R. Kärcher, L. Ley and R.L. Johnson, Phys. Rev. B 30 (1984) (4) 1896.

[5] M. Diserens, J. Patscheider and F. Lévy, Surf. Coat. Technol. 108–109 (1998) 241.

[6] A. Nigro , G. Nobile, M.G. Rubino, R. Vaglio, Phys. Rev. B 37 (1988) 3970.

[7] M. Kaveh and N.F. Mott, J. Phys. C: Solid State Phys. 15 (1982) 707.

[8] S. Veprek, J. Vac. Sci. Technol. A 17 (1999) (5) 2401.

[9] E.-A. Lee and K.H. Kim, Thin Solid Films 420–421 (2002) 371.

[10] M. Diserens, J. Patscheider and F. Lévy, Surf. Coat. Technol. 120–121 (1999) 158.

[11] J. Patscheider, T. Zehnder and M. Dieserens, Surf. Coat. Technol. 146–147 (2001) 201.

[12] R. Hauert, J. Patscheider, L. Knoblauch and M. Diserens, Adv. Mater. 11 (1999) 175.

[13] S.P. Denker, J. of the Less-Common Metals 14 (1968) 1.

[14] Jong Hyun Park, Won Sub Chung, Young-Rae Cho and Kwang Ho Kim, Surf. Coat. Technol. 188-189 (2004) 425.

[15] C.S. Sandu, R. Sanjinés, M. Benkahoul, M. Parlinska-Wojtan, A. Karimi, F. Lévy, Thin Solid Films (accepted).

Chapter 5

Ternary aluminum niobium nitride Nb-Al-N thin films

In this chapter, properties of $Nb_zAl_yN_x$ thin film such as chemical composition, crystalline structure, electronic and mechanical properties are reported as a function of the Al content. Two series of samples are deposited: with low Al content $Nb_zAl_yN_x$, $y \leq 0.17$, obtained by monitoring the Al target current and with high Al content deposited by lowering the current on the Nb target.

5.1. Chemical composition

In order to cover a large range of Al content, two series of $Nb_zAl_yN_x$ films were deposited. The first was deposited at I_{Nb} = 0.3 A with varying the current applied on the Al target (I_{Al}) (figure 5.1a). In this series the Al content progressively increases in $Nb_zAl_yN_x$ up to y =0.17 whereas the Nb content decreases and N remains fixed at x ≈0.5, with increasing I_{Al}. It was found that for I_{Al} >0.15 A the oxygen concentration increases rapidly and reaches a high value, more than 10%. In order to deposit Nb-Al-N films with high Al content and low oxygen content a second series was deposited by keeping the I_{Al} at 0.15 A and varying the current applied on Nb target I_{Nb} from 0.03 to 0.07 A (figure 5.1b). In this case, the Al content increases from y=0.18 up to y=0.33 when the I_{Nb} content decreases from 0.07 to 0.03.

The N content is relatively higher than in the first series, around 0.55 at.% (figure 5.1b). High N content observed for this series is probably related to the high Al content and its high affinity to N compared to that of Nb. The oxygen content is less than 3 at.% for all Nb-Al-N films.

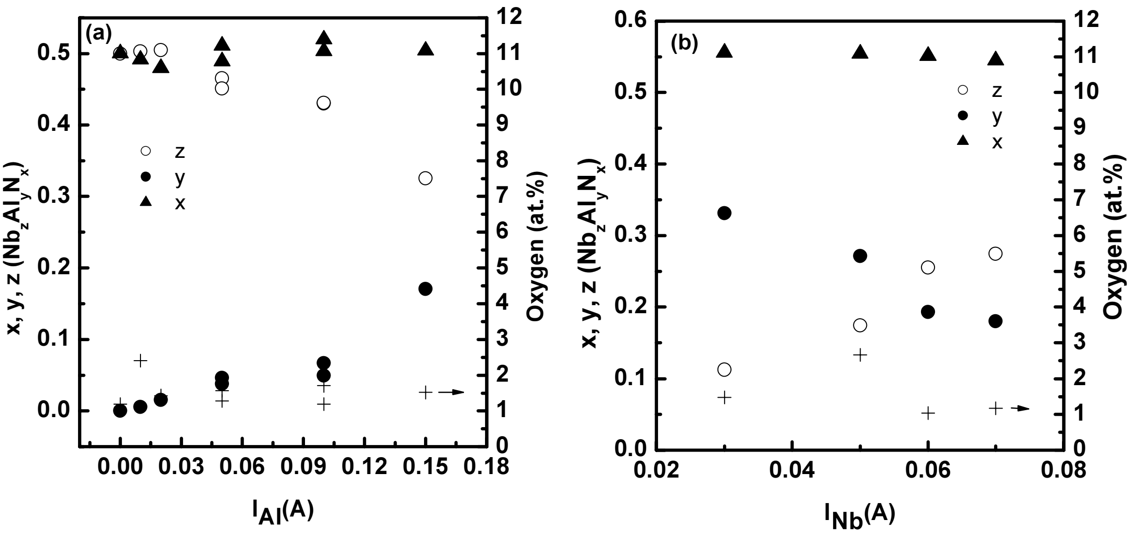

Fig. 5.1. x, y, z and oxygen content in $Nb_zAl_yN_x$ films deposited vs. (a) I_{Al} (I_{Nb} =0.3 A) and (b) I_{Nb} (I_{Al}=0.15 A).

5.2. Crystalline structure

Nb-Al-N films deposited without Al (pure NbN_x) crystallize in mixed δ′+δ phases (figure 5.2a). The addition of Al in small quantity, y≤ 0.02, leads to the deposition of mixed δ′+δ phases, with a relatively low δ′ content in the films. Further increase of y leads to the deposition of single phase cubic δ films, for y ≤0.19 (figure 5.2a and b). For y ≥0.27, the films contain mixed phases: cubic δ structure and hexagonal AlN (PCPDF file 25-1133) structure (figure 5.2b). The results indicate that the solubility limit of Al in NbN_x is y/(y+z) =0.5±0.1. A value of 0.53 for the limit solubility of Al in NbN_x was predicted by Makino et al. [1].

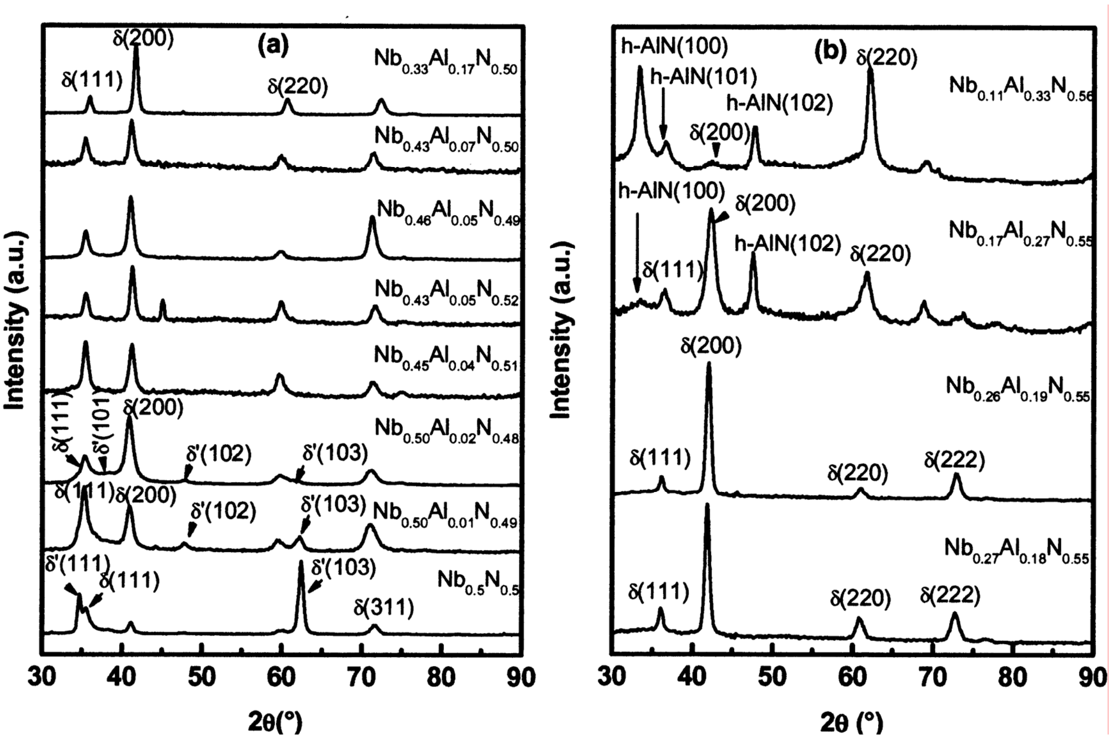

Fig. 5.2. XRD patterns of $Nb_zAl_yN_x$ films deposited vs. (a) I_{Al} and (b) I_{Nb}.

The lattice constants (a) and average grain size (D) calculated from the peaks (111) and (200) of XRD (in grazing incidence configuration, γ= 4°), are represented on figure 5.3 as a function of the Al content in the film. The addition of Al by substitution of Nb leads to the shrinkage of the lattice. The lattice constant decreases following a linear relationship as y increases. Since the atomic radius of aluminum is smaller than that of niobium, the substitution of Nb atoms by Al atoms in the NbN lattice leads to the decrease in the lattice constant. The linear relationship of the lattice constants as a function y indicates the solubility of the Al in the cubic NbN_x structure. Except for two films, y = 0.05 and 0.18, where the average grain size is about 15 nm, all $Nb_zAl_yN_x$ have an average grain size of the order of 10 nm.

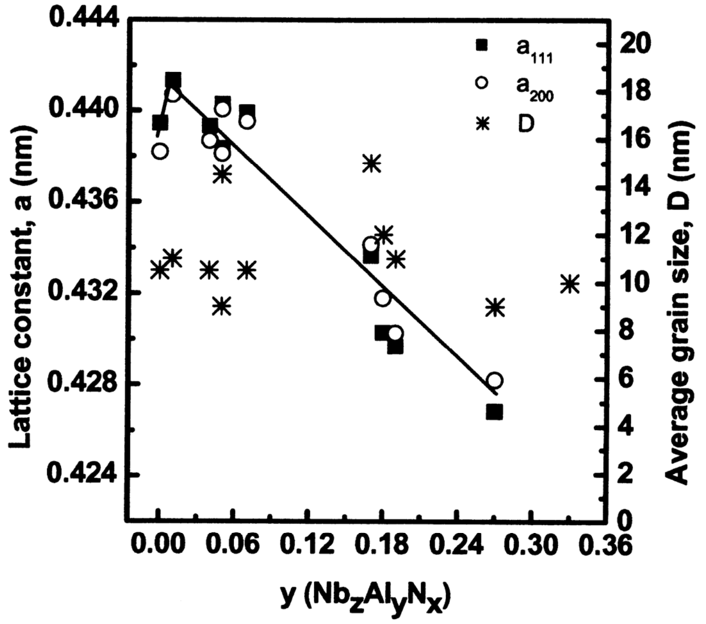

Fig. 5.3. $Nb_zAl_yN_x$ thin films: lattice constants (a) and average size (D) of cubic grains, vs. Al content y. The continuous line follows the lattice constants values as a guide for eye.

5.3. Electrical and optical properties

Room temperature resistivity (ρ_{RT}) of $Nb_zAl_yN_x$ films is represented in figure 5.4. For $y \leq 0.07$ the resisivity ρ_{RT} varies in the range 100-200 μΩcm, without significant trend. For $0.07 \leq y \leq 0.19$, ρ_{RT} increases with increasing y. In this composition range, Al atoms are soluble in the NbN lattice. Since each Al atom gives to the conduction band 2 electrons less than the Nb atom, the density of the free electrons reduces with increasing y. Thus, the resistivity (ρ_{RT}) increases with increasing the Al content, y. The very high resistivity measured for the $Nb_{0.17}Al_{0.27}N_{0.55}$ film is probably due to the presence of the insulating AlN phase.

Reflectivity spectra of $Nb_zAl_yN_x$ films are represented in figure 5.5. In good agreement with XRD data, the reflectivity of the film deposited without Al (pure NbN), is similar to that observed in the case of mixed $\delta'+\delta$ phases (see 3.3.2). For $y \leq 0.02$ the films exhibit a reflectivity similar to that of mixed $\delta'+\delta$ phases. Nevertheless, the reflectivity progressively changes to that of single δ phase, due to the decrease of the δ′ content, with increasing y. For $0.02 < y < 0.19$, the films crystallize in single δ phase. In this concentration range of y, the reflectivity in the IR and visible range decreases with

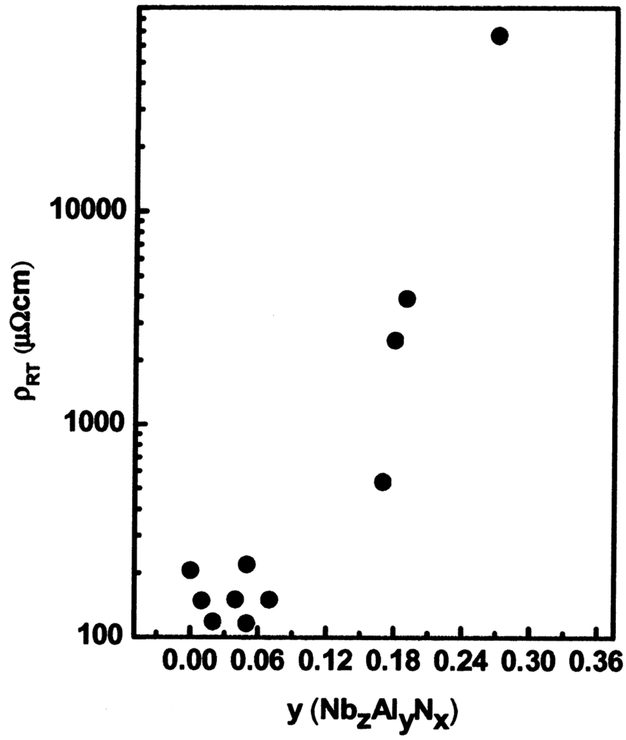

Fig. 5.4. $Nb_zAl_yN_x$ thin films: room temperature resistivity (ρ_{RT}) *vs. Al content y.*

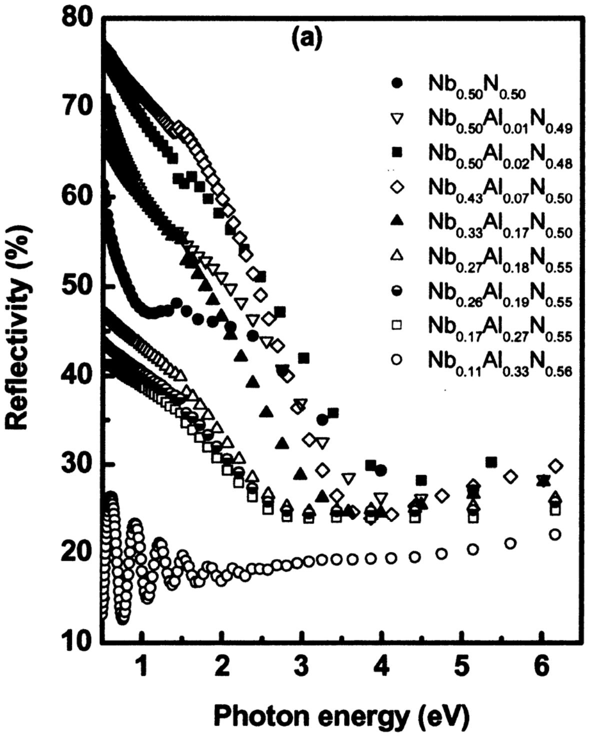

Fig. 5.5. Reflectivity spectra of $Nb_zAl_yN_x$ films.

increasing y. This is caused by the reduction of the density of free electrons in the films resulting from the substitution of Nb atoms by Al atoms in the lattice. For y values higher than 0.27, the reflectivity represented in figure 5.5 is influenced by the reflection at the interface film/substrate since the film becomes less opaque, because of the formation of the insulating hexagonal AlN phase. The interference fringes on the reflectivity of $Nb_{0.11}Al_{0.33}N_{0.56}$ film are due to its transparency.

A semi-infinite model was used for calculating the real part (ε_r) and imaginary part (ε_i) of the dielectric function, refractive index (n) and extinction coefficient (k), for $y<0.19$. Within this range of Al content y, the films are considered as opaque, in the studied range of energy (1.5-5eV). Real and imaginary part of the dielectric function, ε_r and ε_i are represented in figure 5.6a and b, respectively.

It is worth of noting that in good agreement with XRD data, the ε_r and ε_i of the film deposited without Al (pure NbN), are similar to those measured in the case of mixed δ'+δ phases (see 3.3.2).

The position of the screened plasma energy $\hbar\omega_{ps}$ (i.e. where ε_r =0) depends on the Al and N contents. The $\hbar\omega_{ps}$ of the sample $Nb_{0.43}Al_{0.05}N_{0.52}$ and $Nb_{0.46}Al_{0.05}N_{0.49}$, which have similar ratio $y/(y+z) \approx 0.1$, are 2.8 and 3.25 eV, respectively. Thus, the increase of x leads to the shift of the screened plasma energy $\hbar\omega_{ps}$ to the lower energy, indicating a loss in the free electrons concentration. The screened plasma energy $\hbar\omega_{ps}$ of the sample $Nb_{0.43}Al_{0.07}N_{0.50}$ and $Nb_{0.33}Al_{0.17}N_{0.50}$ which have a similar stoichiometric ratio, x =0.50, are 2.5 and 3.25 eV, respectively. Thus, the increase of the ratio $y/(y+z)$ leads to the shift of the $\hbar\omega_{ps}$ toward lower energy, indicating a loss in the free electrons. These trends are consistent with the interpretation that when Al substitutes the Nb atom, it results in two free electrons less per Al atom in the conduction band.

For high values of y, 0.18-0.19, the real part of the dielectric function ε_r remains positive over the measured range 1.5-5 eV.

The film deposited without Al addition (pure NbN) have a refractive index (n) and an extinction coefficient k similar to that observed in the mixed δ'+δ phase. For $y \approx 0.02$, n and k change toward that of single cubic δ NbN with increasing y, due to the decrease in the δ' content (figure 5.7). Further increase in $y \geq 0.02$ leads to the change in the behavior of n and k. The refractive index n becomes high (up to 3.5) over the energy range 1.5-5 eV.

The n and k values at 2.24 eV (wavelength of 500 nm) for the $Nb_zAl_yN_x$ films as a function of y are represented in figure 5.8. For $y \leq 0.02$, the films crystallize in mixed δ′+δ phase. With increasing y from 0 to 0.04, the refractive index n decreases from 2.8 to 1.2. This decrease is due to the decrease in the δ′ phase content. For $0.04 \leq y \leq 0.07$ the films crystallize in cubic δ structure and n remains about 1.2. Further increase in $y > 0.14$ leads to the increase of n up to 2.8.

With increasing y from 0 to 0.01, the extinction coefficient k increases from 2.8 to 3.4. Further, increase of $y > 0.02$ leads to a progressive decrease of k down to 2.2 for $y = 0.19$.

Due to the high solubility of the Al in the NbN in the range $y \leq 0.19$, it appears that the electrical and optical properties of $Nb_zAl_yN_x$ films change with increasing y. A similar behavior has been investigated in Cr-Al-N films where the Al content alters significantly the electronic properties [2].

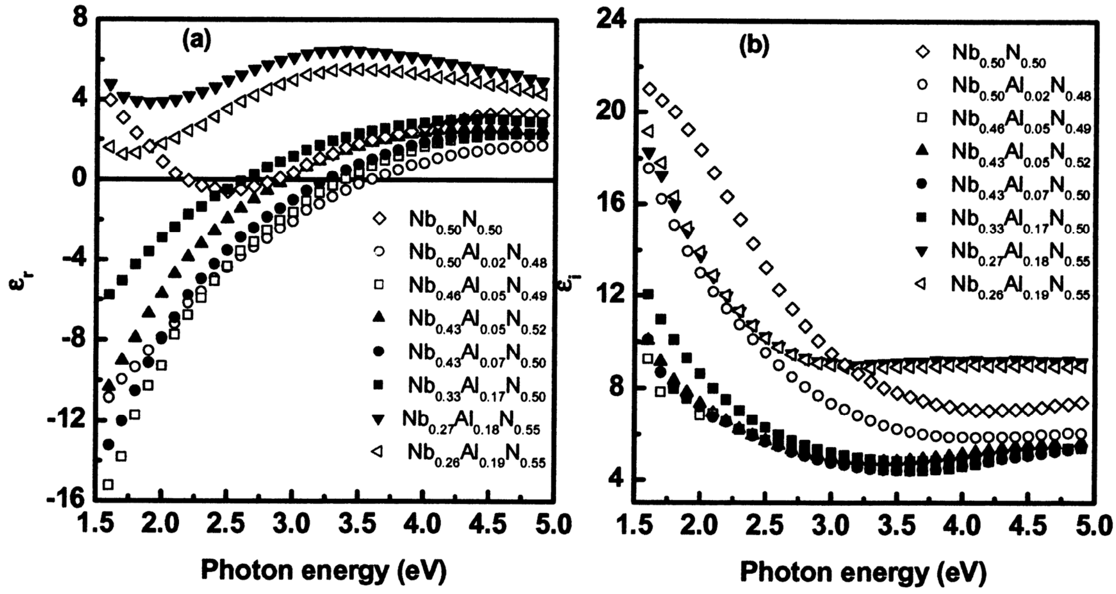

Fig. 5.6. Real part (ε_r) (a) and imaginary part (ε_i) (b) of the dielectric function of $Nb_zAl_yN_x$ films for various Al/Nb composition ratio and stoichiometric ratio N/(Al+Nb).

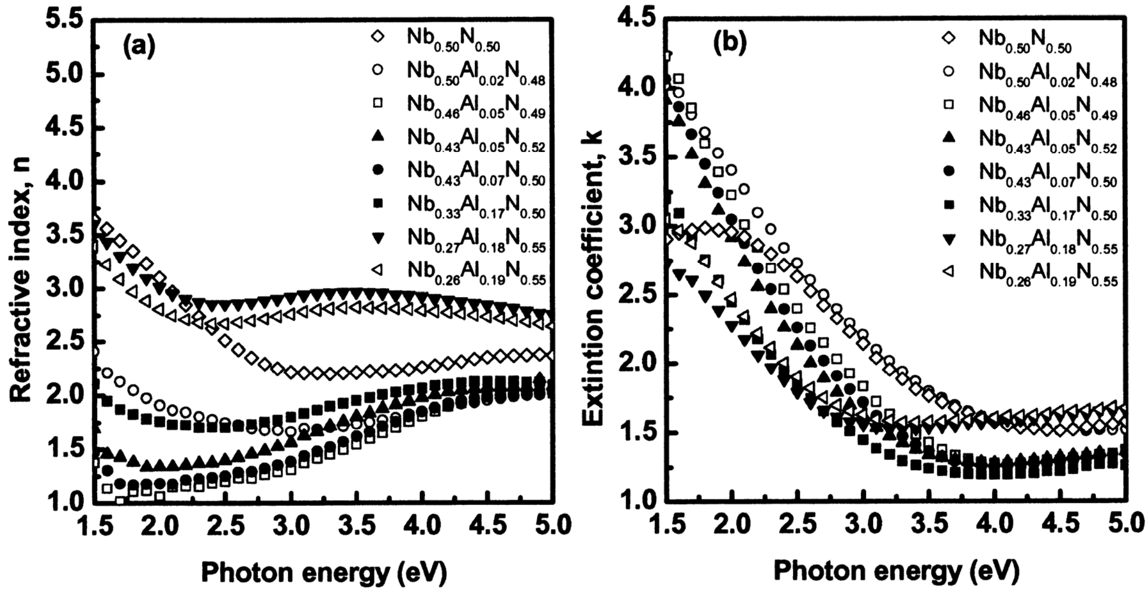

Fig. 5.7. Refractive index (n) (a) and extinction coefficient (k) (b) of the dielectric function of $Nb_zAl_yN_x$ films for various Al/Nb composition ratio and stoichiometric ratio N/(Al+Nb).

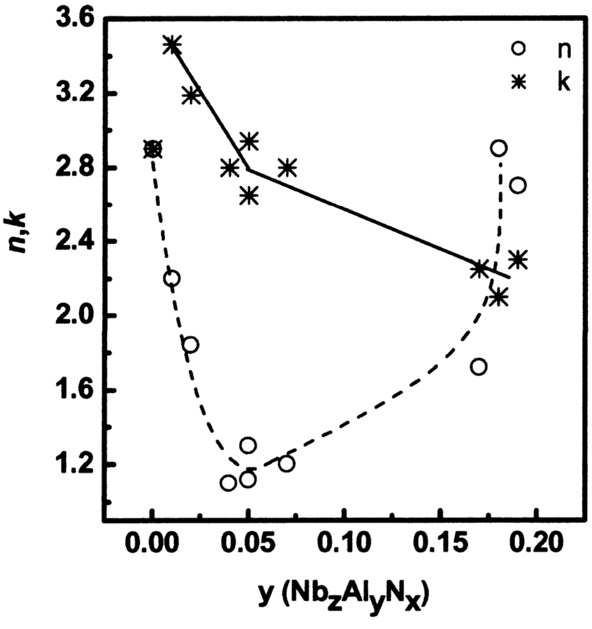

Fig. 5.8. Refractive index (n) and extinction coefficient (k) calculated at 2.24 eV (500nm) vs. y of $Nb_zAl_yN_x$ films.

5.4. Mechanical properties

Hardness and stress as a function of y of the $Nb_zAl_yN_x$ films are represented in the figure 5.9. The measured hardness of the film deposited without Al (pure NbN_x) is about 32 GPa. This relatively high hardness is attributed to relatively high δ′ content in the mixed phases δ′+δ (see 3.4.2). Film with low Al, y ~0.01, shows a low hardness of 24 GPa. This value is typical for single δ-NbN phase. Even if these films have a mixed δ′+δ phases, the low δ′ content in the film is responsible for the lower hardness. With increasing y up to ~0.18 the hardness increases up to 30 GPa. With the appearance of the hexagonal AlN phase, y >0.24 a drastic decrease in the hardness down to 18 GPa, is observed.

In the Nb-Al-N films, $0<y \leq 0.19$, the stress is compressive and varies between -2.2 and -4 GPa. For mixed phases δ- Nb-Al-N and hexagonal AlN films, y >0.24, the stress is close to zero.

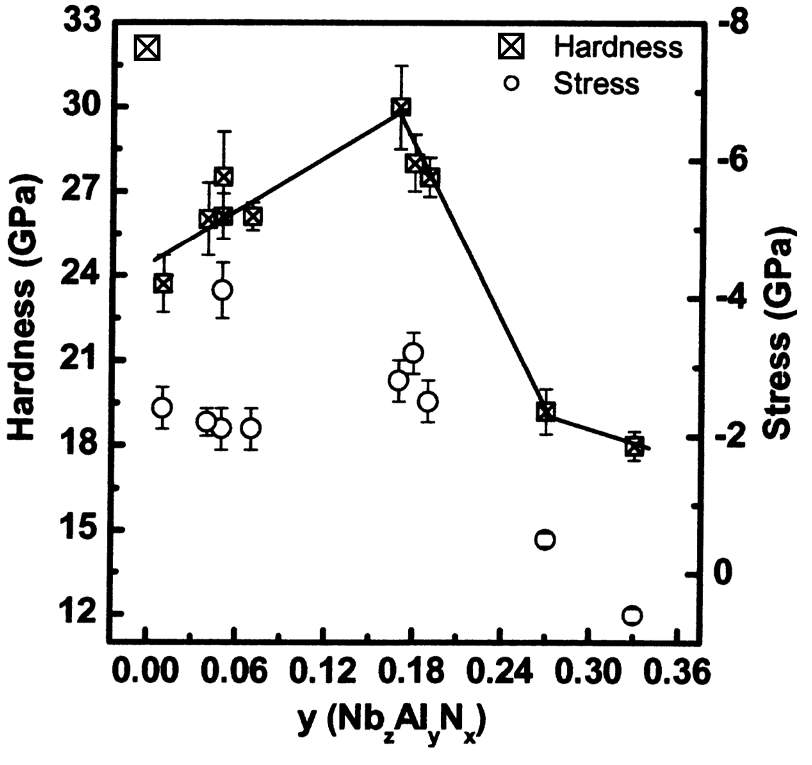

Fig. 5.9. Hardness and stress of $Nb_zAl_yN_x$ films vs. y. the continue line follows the values of hardness as guide for eye.

No study on the mechanical properties of the Nb-Al-N films can be found in the literature. Most of the works report the properties of Ti-Al-N films. Hörling et al. [3] have found that the hardness increases up to 33 GPa with increasing y to 0.3 in $Ti_zAl_yN_x$ arc evaporated films. Liu et al. [4] have found maximum hardness at y =0.12, with increasing y, in $Ti_zAl_yN_x$ films deposited by reactive RF sputtering. They report also a sudden decrease in the hardness for further y increase. This hardness decrease was attributed to the change in crystalline structure from B1 to B4 wurtzite. Similar results were found by Shum et al. [5]. The authors report a maximum hardness and limit solubility of Al in the TiN for the film $Ti_{0.27}Al_{0.18}N_{0.47}O_{0.08}$. They attributed the hardening of the $Ti_zAl_yN_x$ with increasing y up to 0.18 to the densification of the microstructure and the development of refined grain size.

In our case, no decrease of the grain size is observed for harder Nb-Al-N films. The hardening in the Nb-Al-N films is attributed to the solid solution hardening mechanism.

5.5. Summary

The solubility limit of the Al in the NbN lattice is in the range: $y/(y+z) = 0.5\pm0.1$ ($Nb_zAl_yN_x$). Passing this value an insulating hexagonal AlN phase is formed. The electrical and optical properties of the $Nb_zAl_yN_x$ are very altered by the change in the value of y and x. The hardness of the $Nb_zAl_yN_x$ is maximum in the film with y =0.19 (solubility limit). At higher y the formation of the AlN phase reduces the hardness. Hardening observed in the $Nb_zAl_yN_x$ films is attributed to the solid solution hardening mechanism.

References of chapter 5

[1] Y. Makino, M. Mori, S. Miyake, K. Saito, K. Asami, Surf. Coat. Technol. 193 (2005) 219.

[2] R. Sanjinès, O. Banakh, C. Rojas, P. E. Schmid and F. Lévy, Thin Solid Films 420-421 (2002) 312

[3] A. Hörling, L. Hultman, M. Odén, J. Sjölén and L. Karlsson, Surf. Coat. Technol. 191 (2005) 384)0.

[4] G.T. Liu, J.G. Duh, K.H. Chung and J.H. Wang, Surf. Coat. Technol. (in press).

[5] P. W. Shum, K. Y. Li, Z. F. Zhou and Y. G. Shen, Surf. Coat. Technol. 185 (2004) 245.

Chapter 6

Conclusion

This work provides new results on the physical properties of NbN, Nb-Si-N and Nb-Al-N sputter deposited thin films.

Three single and mixed phases of niobium nitride, hexagonal β-Nb_2N and δ′-NbN as well as cubic δ-NbN films were successfully deposited by reactive magnetron sputtering with varying nitrogen partial pressure P_{N2} and substrate temperature T_s. Low nitrogen partial pressure P_{N2} favors the deposition of the hexagonal β-Nb_2N phase whereas at higher P_{N2} the stable phase is cubic δ-NbN. For intermediate P_{N2}, the hexagonal δ′-NbN phase is stable. The increase in the substrate temperature T_s leads to the increase in the hexagonal δ′-NbN phase content. Only mixed phases δ+β and δ+δ′ were deposited. All the NbN films show columnar morphology. The columnar structure in the hexagonal β-Nb_2N and δ′-NbN phases is more pronounced than in the cubic δ-NbN. The film morphology containing the hexagonal δ′-NbN phase appears to be more compact than those with low δ′-NbN content. In contrast to the cubic δ-NbN and hexagonal δ′-NbN phases, the microstructure of the hexagonal β-Nb_2N phase shows feather like columns formed by multitwins sequences.

The spectroscopic ellipsometry measurement provides complementary results for the determination of the phase composition in the NbN system. Reflectivity spectra of the hexagonal δ′-NbN phase exhibit a sharp edge at 1 eV which is not usual for the fcc MeN phases.

Different values are measured for the difference in the core level binding energy ΔBE (ΔBE = N 1s – Nb $3d_{5/2}$), for the three phases, suggesting that the covalent character is more pronounced in hexagonal β-Nb_2N and δ´-NbN phases than in the cubic δ-NbN one.

The hexagonal β-Nb_2N and δ´-NbN thin films exhibit high hardness of 35 and 40 GPa whereas cubic δ-NbN shows relatively low hardness of 25 GPa. While the hexagonal δ´-NbN phase film exhibits high compressive stress of about –3 GPa the hexagonal β-Nb_2N phase film is not stressed whereas cubic δ-NbN phase film show low compressive stress of about -1.5 GPa. The high covalent character of the hexagonal β-Nb_2N and δ´-NbN phases compared to that of the cubic is partially responsible for the different hardness measured for the different phases. The highest hardness and good stability were found in the δ´-NbN phase.

The addition of a third element in transition metal nitrides leads to significant changes in most properties. In particular, silicon stabilizes the cubic δ-NbN phase of NbN. It influences the electrical and optical properties.

A model for the film formation of Nb-Si-N thin films deposited by DC magnetron sputtering is proposed. Three distinct concentration domains are pointed out. In Domain 1 ($1 \leq C_{Si} \leq 4$ at.%) the Si atoms substitute Nb in the NbN lattice and polycrystalline films of NbN:Si are deposited. In Domain 2 ($4 \leq C_{Si} \leq 7$ at.%) a fraction of Si atoms segregates to the grain boundaries. A SiN_x layer is formed on the NbN:Si crystallite surfaces. The covering ratios increase with Si content, up to 100% (formation of a monolayer). For a further increase of the Si content (Domain 3), the NbN:Si crystallites, surrounded by a monolayer of SiN_x, reduce their size from 18 to 2 nm. So the increasing amount of the SiN_x phase in the films is realized by increasing the surface to volume ratio of the NbN:Si nanocrystallites.

The formation of the SiN_x layer on the crystal surface is responsible for the changes observed in the electrical and optical properties of Nb-Si-N films with increasing Si content.

The electrical resistivity measured as a function of temperature is proposed to provide an experimental mean for determining the limit of Si solubility in Nb-Si-N system and for following the thickness evolution of the SiN_x coverage layer in the composite films.

Concerning the $Nb_zAl_yN_x$ films, the solubility limit of Al in the NbN lattice is $y/(y+z) = 0.5 \pm 0.1$. Passing this value, an insulating hexagonal AlN phase is formed. The electrical and optical properties of the $Nb_zAl_yN_x$ deposited films are significantly modified by the change in the values of y and x. The Al atom substitution gives two electrons less, to the conduction band, than the Nb atom.

Therefore, increasing the Al content y leads to the increase of the resistivity and the change in the optical properties to that of a poor conductor.

The hardness of the $Nb_zAl_yN_x$ is maximum in the film with y =0.19 (solubility limit). At higher concentration y, the formation of the AlN_x phase reduces the hardness. The hardening observed in the $Nb_zAl_yN_x$ films is attributed to the solid solution hardening mechanism.

Finally, the most interesting results are provided by the investigation of the physical properties of the hexagonal δ′-NbN phase, in particular the mechanical and optical properties. This phase has a hardness of 40 GPa and keeps this high value of 35 GPa after heating in vacuum at 1000°C. The sharp reflectivity edge at 1 eV measured in hexagonal δ′-NbN thin films can be used in optical applications e.g. filter.

While the system NbN presents many phases, it appears that the addition of the third element, Si and Al, allows the stabilization of the cubic δ phase. In both Nb-Si-N and Nb-Al-N systems Si and Al are soluble up to a certain limit. Passing this limit the third element segregates at the grain boundaries forming SiN_x and hexagonal AlN_x. Nevertheless, the segregation differs from one system to another. In the case of the Nb-Si-N films the formed SiN_x segregates as layer surrounding the NbN:Si grains. For the Nb-Al-N films the hexagonal AlN_x phase segregates as separated phase. The high Al solubility in NbN allows the control of the electrical and optical properties of Nb-Al-N thin film by changing the Al content. In contrast, the formation of the SiN_x insulating layer at the surface of the NbN:Si crystallites limit the conductivity in the Nb-Si-N system.

Annexe A

Si coverage of the NbN:Si grain

The objective is to determine the relation between the concentrations of Si in NbN films and the Si surface "monolayer" at the surface of NbN crystallite of typical size D.

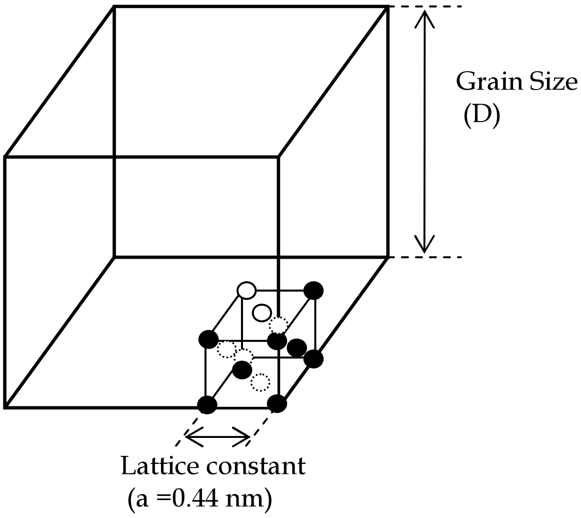

The volume of the grain is $V_{grain} = D^3$ (D: grain size) whereas that of the unit cell is $V_{cell} = a^3$ (a: lattice constant). The surface of the grain is $S_{grain} = 6 \times D^2$, the surface of one face of the unit cell is $S_{cell-face} = a^2$

The number of the cells present in a grain is $N_{cell/grain} = \frac{D^3}{a^3}$ and the number of the face cell present on the grain surface is $N_{S,cell-face} = \frac{S_{grain}}{S_{cell-face}} = 6 \times \frac{D^2}{a^2}$.

For the cubic fcc NbN structure, in each unit cell the number of the Nb atoms is $\frac{1}{2} \times 6 + \frac{1}{8} \times 8 = 4$ (atoms/Volume cell). For each face of the unit cell we have $1 + \frac{1}{4} \times 4 = 2$ (atoms/cell face).

The number of Nb atoms in one grain is

$$N_{V/grain} = 4 \times N_{cell/grain} = 4 \times \frac{D^3}{a^3}$$

The number of the Nb sites on the grain surface is

$$N_{S/grain} = 2 \times N_{S,cell-face} = 2 \times 6 \times \frac{D^2}{a^2} = 12 \times \frac{D^2}{a^2}.$$

The ratio between the number of Nb on the grain surface and the number of atoms inside the grain is $\frac{N_{S/grain}}{N_{V/grain}} = \frac{\left(12 \times \frac{D^2}{a^2}\right)}{\left(4 \times \frac{D^3}{a^3}\right)} = 3 \times \frac{a}{D} \Rightarrow N_{S/grain} = N_{V/grain} \times \left(3 \times \frac{a}{D}\right)$.

Under the assumption that the segregated Si atoms occupy the sites of Nb atoms on the crystallite surface, the Si coverage is calculated by:

$$\text{Si coverage} = \frac{N_{Si/grain-surface}}{N_{S/grain}}$$

where

$N_{Si/grain-surface}$ = number of the Si atoms segregated to the grain boundary of one grain,

$N_{Si/grain-surface}$ = Si atoms in one grain - Si atoms soluble in one NbN grain.

$N_{V/grain}$ sum of the number of the Nb and Si atoms in the grain.

If the numerator and denominator of the relation of the Si coverage are divided by the total number of atoms forming grain:

$$\text{Si coverage} = \frac{C_{Si} - 4}{(C_{Nb} + 4) \times \left(3 \times \frac{a}{D}\right)}$$

where C_{Si} and C_{Nb} are the Si and Nb content, respectively.

Numerical application: For Nb-Si-N film with C_{Si} =6.5 at.% the C_{Nb} is 38.5 at.% and the grain size is D= 18 nm this implies $\text{Si coverage} = \frac{6.5 - 4}{(38.5 + 4) \times \left(3 \times \frac{0.44}{18}\right)} \approx 80\%$.

Acknowledgments

Several senior researchers and colleagues have contributed in some way to the achievement of this work which has been carried out at the Institut de Physique de la Matière Complexe (IPMC) of the Ecole Polytechnique Fédérale de Lausanne (EPFL).

First of all, Prof. Francis Lévy, who proposed the subject to me and supervised my Ph.D work. Also, the financial support of the Swiss National Science Foundation is acknowledged.

I thank especially my colleague and friend Dr. C-S. Sandu who provided a great contribution to this work, by supporting and helping me. I appreciate especially his friendship.

I am grateful to Dr. R. Sanjinés for his advices and assistance, to Dr. P.-E. Schmid for critical discussions, to Dr. O. Banakh for my assistance during the first critical time of my Ph.D work. Dr. S. Springer is acknowledged for sharing his experience on the analysis techniques, for instance XRD and ellipsometry, with me and Dr. M. Parlinska for TEM observations.

My acknowledgements also address Dr. A. Karimi for giving me the opportunity to perform the nanoindentation tests, Dr. N. Tabet, King Fahd University, Saudi Arabia, for XPS measurements and Prof. S. Achour who provided me the opportunity for my initial research on the PVD thin films.

Furthermore, I would like to thank Mr. H. Jotterand, Mr. J. Besuchet, Mr. M. Tschumi and Ms. C. Crot for their excellent technical assistance.

I want to thank all my family, especially my mother for her sacrifices and my wife for her encouragements.

Curriculum vitae

Name: BENKAHOUL Moushab
Email: moushab.benkahoul@epfl.ch
Date and place of birth: October 16, 1973 in Constantine, Algeria
Nationality: Algerian
Marital status: married

Higher education:

1991	Baccalauréat en Mathématiques, Lycée frères Biskri, Constantine, Algeria.
1991-1995	High diploma in solid state physics, Department of physics, University of Constantine, Algeria.
1996-1999	Magister en physique du solide, Department of physics, University of Constantine, Algeria, thesis entitled "DEPOSITION AND CHARACTERISATION OF TiN THIN FILMS".
2001-2005	Ph.D student at the Swiss federal institute of Technology Lausanne (EPFL), thesis entitled "NIOBIUM NITRIDE BASED THIN FILMS DEPOSITED BY DC REACTIVE MAGNETRON SPUTTERING: NbN, NbSiN and NbAlN".

Professional experience

1998-1999	Institute of Biology, University of Constantine, Algeria: Teaching assistant of biophysics.
2000-2001	Institute of Exacts sciences, University of Constantine, Algeria: Teaching assistant of electricity.
2001-2005	Swiss federal institute of Technology Lausanne (EPFL): Reaserch and teaching in the field of thin film technology, PVD, Hard coating and characterization.

Languages

Arabic (native), French, English.

Publications

1. O. Bourbia S. Achour, S. Zerkout, M. Benkahoul and A. Harabi "Effect of tantalum addition on optical transmittance and electrical resistivity of TiN thin films prepared by d.c. magnetron sputtering", KEY ENG. MAT. 206-2: 523-526 2002.
2. M. Benkahoul, E. Martinez, A. Karimi, R. Sanjinés and F. Lévy, "Deposition and characterisation of cubic and hexagonal NbN thin films", Surf. Coat. Technol. 180-181, (2004) 178.
3. M. Benkahoul, C.S. Sandu, N. Tabet, M. Parlinska-Wojtan, A. Karimi and F. Lévy, "Effect of Si incorporation on the properties of niobium nitride films deposited by DC reactive magnetron sputtering", Surf. Coat. Technol. 188-189 (2004) 435.
4. S. Zerkout, M. Benkahoul, H. Sahraoui, S. Achour and A Mosser, "Effect of heat treatment on TiN, film structure", Materials Science Forum 480-481 (2005) 187.
5. R. Sanjinés, M. Benkahoul, D. Music and F. Lévy, "Electronic state and physical properties of hexagonal Nb_2N and NbN", Thin Solid Films. (in press).
6. C.S. Sandu, R. Sanjinés, M. Benkahoul, M. Parlinska-Wojtan, A. Karimi and F. Lévy, "Structural and chemical properties of sputter deposited Ti-Ge-N thin films", Surf. Coat. Technol. (accepted).
7. C.S. Sandu, R. Sanjinés, M. Benkahoul, M. Parlinska-Wojtan, A. Karimi, F. Lévy, "Influence of Ge addition on the morphology and properties of TiN thin films deposited by magnetron sputtering", Thin solid films (accepted).
8. C.S. Sandu, M. Benkahoul, M. Parlinska-Wojtan, R. Sanjinés and F. Lévy, "Morphological, structural and mechanical properties of NbN thin films deposited by reactive magnetron sputtering", Surf. Coat. Technol. (accepted).

Submitted papers

1. R. Sanjinés, D. Music, M. Benkahoul, M. Papagno and F. Lévy, "Electronic structure of Nb_2N and NbN thin films", J. Appl. Phys.
2. C.S. Sandu, M. Benkahoul, R. Sanjinés and F. Lévy, "Relationship between structure, morphology and electrical properties of sputtered Nb-Si-N thin films: from solid solution to nanocomposite", J. Appl. Phys.
3. R. Sanjinés, M. Benkahoul, C.S. Sandu and F. Lévy, "Optical and electrical properties Nb-Si-N thin films deposited by DC reactive magnetron sputtering", J. Appl. Phys.
4. C.S. Sandu, R. Sanjinés, M. Benkahoul, F. Medjani and F. Lévy “Formation of composite ternary nitride thin films by magnetron sputtering co-deposition”, Thin solid films.

Presentations at conferences and seminaries

1. Seventh conference and exhibition of the European ceramic society, Brugge 2001, Belgium, "Effect of tantalum addition on optical transmittance and electrical resistivity of TiN thin films prepared by d.c. magnetron sputtering", O. Bourbia S. Achour, S. Zerkout, M. Benkahoul and A. Harabi.
2. Annual meeting of thé Swiss Physical Society, Bâle, 2003, "Deposition and characterisation of cubic and hexagonal NbN thin films", M. Benkahoul, E. Martinez, S. Springer, R. Sanjinés, P.E. Schmid, F. Lévy.
3. Spring meeting of The European Material Research Society, Strasbourg, France, June 2003, "Structural and Mechanical Properties of sputtered cubic and hexagonal NbN_x thin films", M. Benkahoul, E. Martinez, R. Sanjinés, A. Karimi and F. Lévy.
4. First International Meeting on Applied Physics APHYS, Badajoz, Spain, 2003, "Effect of heat treatment on TiN, film structure", S. Zerkout. M. Benkahoul, H. Sahraoui, S. Achour and A. Mosser.
5. Annual meeting of the Swiss Physical Society, Neuchâtel, 2004, "Improving nanohardness of NbN thin films by addition of Si", M. Benkahoul, C.S. Sandu, A. Karimi and F. Lévy.
6. International Conference on Metallurgical Coatings and Thin Films, San Diego, California, 2004, "Effect of Si incorporation on the properties of niobium nitride films", M. Benkahoul, C.S. Sandu, A. Karimi and F. Lévy
7. ASEVA Summer School for vacuum Science and Apllications, Avila, Spain, July 2004, "Deposition and characterization of $NbSi_yN_x$ sputtered thin Films", M. Benkahoul, C.S. Sandu, N. Tabet, M. Parlinska-Wojtan, A. Karimi, R. Sanjinés and F. Lévy.
8. ASEVA Summer School for vacuum Science and Apllications, Avila, Spain, July 2004, "Reactively Sputtered Ternary Films of Ti-Ge-N and their Properties", C.S. Sandu, R. Sanjinés, M. Benkahoul, M. Parlinska-Wojtan, A. Karimi and F. Lévy.
9. International Conference on Metallurgical Coatings and Thin Films, San Diego, California, 2005, "Electronic structure and physical properties of hexagonal Nb_2N and NbN", R. Sanjinés, M. Benkahoul, D. Music and F. Lévy.
10. International Conférence on Metallurgical Coatings and Thin Films, San Diego, California, 2005, "Structural and Chemical Properties of Sputtering Deposited Ti-Ge-N Thin Films", C.S. Sandu, R. Sanjinés, M. Benkahoul, M. Parlinska-Wojtan, A. Karimi and F. Lévy.
11. Spring meeting of The European Material Research Society, Strasbourg, France, June 2005, "Properties of $NbSi_yN_x$ thin films deposited by DC reactive magnetron sputtering", M. Benkahoul, C.S. Sandu, R. Sanjinés, A. Karimi and F. Lévy.
12. Spring meeting of The European Material Research Society, Strasbourg, France, June 2005, "Morphological, structural and nechanical properties of NbN thin films deposited by reactive magnetron sputtering", C.S. Sandu, M. Benkahoul, R. Sanjinés, A. Karimi and F. Lévy.

13. International Conference on Surfaces, Coatings and Nanostructured Materials, Aveiro, PORTUGAL, September 2005, "Formation of composite Ternary nitride thin films by magnetron sputtering co-deposition", C.S. Sandu, R. Sanjinés, M. Benkahoul and F. Lévy.